A High Pressure
Xenon Time Projection Chamber for Double Beta Decay

Thesis by

Bridget Mary Geraldine O'Callaghan-Hay

In Partial Fulfillment of the Requirements

for the Degree of

Doctor of Philosophy

California Institute of Technology

Pasadena, California

1989

(submitted Jan 9, 1989)

to

Jon and Edgar

Acknowledgements

I wish to express special thanks to Professor Felix Boehm for his encouragement and support throughout my studies at Caltech. I also wish to thank the collaborators on this experiment, especially my fellow graduate student, Henry T-k Wong, Herb Henrikson and Zafar Iqbal. A special thanks goes to Elsa Garcia for her assistance and friendship. Thanks also go to all the members of Ph 34.

I wish to acknowledge the financial assistance provided by the California Institute of Technology and the U.S. Department of Energy.

I am ever grateful to my parents for their constant support and encouragement throughout my many years of study.

This thesis is affectionately dedicated to Jon, my husband, without whose constant encouragement, understanding and endless patience I would not have completed this project. Buíochas óm chroí go hiomlán.

Abstract

This thesis describes the design, construction and performance of a high-pressure, xenon, gas time projection chamber (TPC) for the study of double beta decay in ^{136}Xe. The TPC when operating at 5 atm can accommodate 28 moles of 60 % enriched ^{136}Xe. The TPC has operated as a detector at Caltech since 1986. It is capable of reconstructing a charged particle trajectory and can easily distinguish between different kinds of charged particles. A gas purification and xenon gas recovery system were developed. The electronics for the 338 channels of readout was developed along with a data acquistion system. Currently, the detector is being prepared at the University of Neuchatel for installation in the low background laboratory situated in the St. Gotthard tunnel, Switzerland. In one year of runtime the detector should be sensitive to a 0ν lifetime of the order of 10^{24} y, which corresponds to a neutrino mass in the range 0.3 to 3.3 eV.

Contents

CHAPTER ONE

Theoretical Background

1.1 Introduction

Double beta decay is a semileptonic weak process in which a nucleus (N,Z), undergoes a transition to the nucleus (N-2, Z+2), the transition to the intermediate nucleus (N-1, Z+1) being energetically forbidden or strongly hindered. There are two possible modes for this process, resulting in a final state with two electrons along with either two or zero neutrinos. The two-neutrino mode (2ν) can occur as a second-order perturbation of the weak interaction within the Minimum Standard Model, in which neutrinos are massless Dirac particles. For the zero-neutrino (0ν) mode to occur, the violation of the law of lepton number conservation along with the existence of massive Majorana neutrinos is required.

A description of the 0ν mode requires a mixture of elementary particle physics and nuclear physics. The issues in particle physics that can be resolved through a study of double beta decay include the questions: Is the neutrino a Majorana particle and if so, what is its mass? Do weak interactions contain leptonic currents with a small right-handed component? The principal issues in nuclear physics deal with the identification and evaluation of the nuclear matrix elements responsible for the decay.

This thesis describes the design, construction and performance of a high-pressure xenon gas, time projection chamber (TPC) for the study of double beta decay in ^{136}Xe. The present Chapter 1 describes neutrinos and their properties and their implications on double beta decay. Chapter 2 describes the operating principles of the TPC. Chapter 3 describes the results of the study of

a prototype TPC. In Chapter 4, a description of the Monte Carlo code for simulating tracks in the TPC is presented. Chapter 5 describes the design and construction of the 200 liter TPC, with particular emphasis on the design of the anode system. A description of the readout electronics and data acquistion is presented in Chapter 6. Chapter 7 discusses the performance of the TPC and the future plans for the experiment.

1.2 The Neutrino

In 1930, Pauli [1] first postulated the existence of the neutrino, in order to explain the observed continuous electron spectrum that accompanies nuclear beta decay. However, the first experimental, direct detection of the neutrino was not made until 1956, when Cowan et al. [2] observed inverse beta decay

$$\overline{\nu_e} + p \rightarrow e^+ + n \,,$$

i.e., the absorption of an antineutrino with a proton to produce a neutron and a positron. In addition to the electron neutrino ν_e, emitted in beta decay, two other neutrinos were discovered, the muon-neutrino ν_μ [3] and the tau-neutrino ν_τ [4]. The concept that these neutrinos could mix was first proposed by Maki et al. [5] and Pontecorvo [6].

In 1956, Lee and Yang [7] worked out the fundamental interactions responsible for the production of neutrinos, which came to be known as the V-A (vector minus axial vector) law. Since 1961, after many experimental and theoretical developments, the minimum standard model of electroweak interaction emerged ([8], [9], [10]). This model is capable of describing all the known physics of weak and electromagnetic interactions and to date has survived a vast number of rigorous tests without showing any signs of failure. However, in the present form, the model is not capable of predicting the masses of the fermions, nor can it explain the existence of the several fermion

families and the related quark families. Although much progress has been made in understanding neutrino properties and interactions, some issues still remain to be settled, including:

- Why are there different neutrino families and how many such families exist?

- Is the conservation of lepton number exact?

- Are neutrinos Dirac or Majorana particles?

- Do neutrinos have a nonvanishing rest mass?

- Are neutrinos stable against decay?

Let us recall that a Dirac particle is one that is distinct from its antiparticle, whereas a Majorana particle is identical to its antiparticle. To clarify the distinction, consider the following arguments of Kayser [11]. In a given reference frame (e.g.,the lab frame) as a result of the V-A law, neutrinos emitted in ordinary beta decay will have a polarization - $|v|/c$ along their direction of motion. This neutrino is a left-handed neutrino, ν_l. By virtue of CPT invariance, which is assumed to be valid, the existence of ν_l implies the existence of $\overline{\nu_r}$, the CPT mirror image. If this neutrino is massive, it travels more slowly than light, and so there exists a frame of reference that moves faster than ν_l. In this frame, the same neutrino will appear polarized in the positive direction of travel and so will be a right-handed neutrino ν_r, and this neutrino may not be the same particle as the CPT mirror image $\overline{\nu_r}$ of ν_l. If it is not the same, then altogether there are four states with the same mass. This quadruplet of states is called a Dirac neutrino ν^D. If the particle ν_r obtained by the Lorentz transformation to the moving frame of reference is the same particle as $\overline{\nu_r}$, then only two states with a common mass exist. This pair of states represents a Majorana neutrino ν^M. If the neutrino rest mass is zero, then it travels with the speed of light, and so the helicity of the neutrino can no longer be reversed by going to a faster-moving frame. Since the dipole moment of a neutrino with

left-handed interactions is proportional to the mass, it vanishes for the massless neutrino. Thus, an external **E** or **B** field also cannot reverse the helicity of the massless neutrino. Since the two states ν_l^D and $\overline{\nu_r}^D$ and the states ν_r^D and $\overline{\nu_l}^D$ are completely disconnected, the Dirac-Majorana distinction has vanished.

Leptons comprise the electron e^-, the muon μ^-, and the tau lepton τ^- and their associated neutrinos ν_e, ν_μ, and ν_τ. The leptons are divided into distinct flavors or families. Each lepton family has associated with it an additive quantum number called the lepton number (L_e, L_μ, L_τ), which is +1 for each lepton in that family, -1 for each antilepton of that family, and 0 for all other particles. The Standard Model assumes that each lepton number (L_e, L_μ, L_τ) is conserved in all processes. Some models now question whether or not lepton number is conserved absolutely and allow the possibility of a small but observable deviation. A study of double beta decay can test this conservation law to great accuracy because in order for the 0ν mode to occur, the total lepton number must change by two units.

Historically, the question associated with double beta decay is whether the electron neutrino should be described by a Dirac or a Majorana field. Prior to 1955, when Davis [12] showed that ν_e and $\overline{\nu_e}$ are not identical, physicists believed that the electron neutrino could be described by both the Dirac and the Majorana fields. The null result of Davis's tests was interpreted by many as the proof that the neutrino was not a Majorana particle.

No theoretical prediction for the neutrino mass exists. Prior to 1980, only upper bounds for the mass had been reported. In 1980 Lubimov et al. [13] measured the ^{3}H beta spectrum with a magnetic spectrometer and claimed the mass as 14 eV $\leq m_{\overline{\nu_e}} \leq$ 46 eV at the 99% confidence level. In a more recent experiment, Lubimov [14] reported mass values in the range 17-40 eV. It was this and other reports indicating a nonvanishing neutrino mass which have stimulated the recent growth in interest in neutrino physics. A massive neutrino has many important implications in various branches of physics. According to

the standard electroweak theory of Glashow [8], Salam and Ward [9], and Weinberg [10], neutrinos should be massless. The development of grand unified theories (GUTS) of the electroweak and strong interactions suggested that rather than result from an exact global symmetry, the conservation of lepton number may only appear to be valid at low energies because of the the large grand unified mass scale M that governs the symmetry breaking. Current GUTS suggest that the neutrino has a small Majorana mass of a size $\approx$(light mass)^2/M, where the "light mass" is typically that of a quark or a charged lepton. Thus, massive neutrinos provide one of the crucial tests for different theoretical models.

Massive neutrinos are important in the fields of cosmology and astrophysics. According to modern cosmology, the universe can be in either of the following states: open, closed, or flat. The open universe expands forever, whereas the closed universe eventually stops expanding, collapses back in on itself, heats up, and goes through another "big bang". Between these two cases is the flat universe, which is expanding now but ultimately, after an infinite time, will come to rest. If neutrinos are sufficiently massive (a few eV) and if their lifetimes are comparable to or longer than the lifetime of the universe, they could account for enough energy density to close the universe [15]. Between 1970 and 1984 Davis et al [17], have conducted a series of measurements on the solar neutrino flux. The measured neutrino flux is about three times lower than predicted. This discrepancy has become known as the solar neutrino puzzle. One suggested way to resolve the discrepancy is to relate the reduction of the neutrino flux to neutrino oscillations either in the interior of the sun or during the trip to Earth [15].

From the above discussion it can be seen how a study of double beta decay can help in the determination of the interactions and properties of the neutrino.

1.3 Double Beta Decay

Double beta decay, as mentioned in the introduction, is the process in which two neutrons in a nucleus decay into two protons, two electrons, and either two or no antineutrinos. The decay in which two antineutrinos are emitted is labeled two-neutrino double beta decay ($2\nu\beta\beta$ decay). This mode can occur regardless of whether the neutrinos are Dirac or Majorana, and massive or massless. It is a second-order, weak process in the standard model. The decay in which no neutrinos are emitted is called neutrinoless double beta decay ($0\nu\beta\beta$ decay). For $0\nu\beta\beta$ decay to occur, the neutrino must be a massive Majorana particle. Figure (1.1) is a schematic of the modes of $\beta\beta$ decay.

1.3.1 $2\nu\beta\beta$ decay

For the $2\nu\beta\beta$ decay

$$(Z, A) \rightarrow (Z+2, A) + 2e^- + 2\overline{\nu}_e$$

to occur, the following two conditions must be satisfied:

$$M(Z, A) > M(Z+2, A)$$

and

$$M(Z, A) < M(Z+1, A).$$

Here, M(Z, A) is the atomic mass of the isotope (Z, A). The second condition is the requirement that the mass of the intermediate nucleus must be greater than the mass of the parent nucleus. This completely suppresses the process in which two ordinary beta decays in sequence can transform the nucleus (Z, A) to (Z+2, A).

1.3.2 $0\nu\beta\beta$ decay

To determine the conditions necessary for the $0\nu\beta\beta$ decay to occur consider the following sequence and also Figure (1.2):

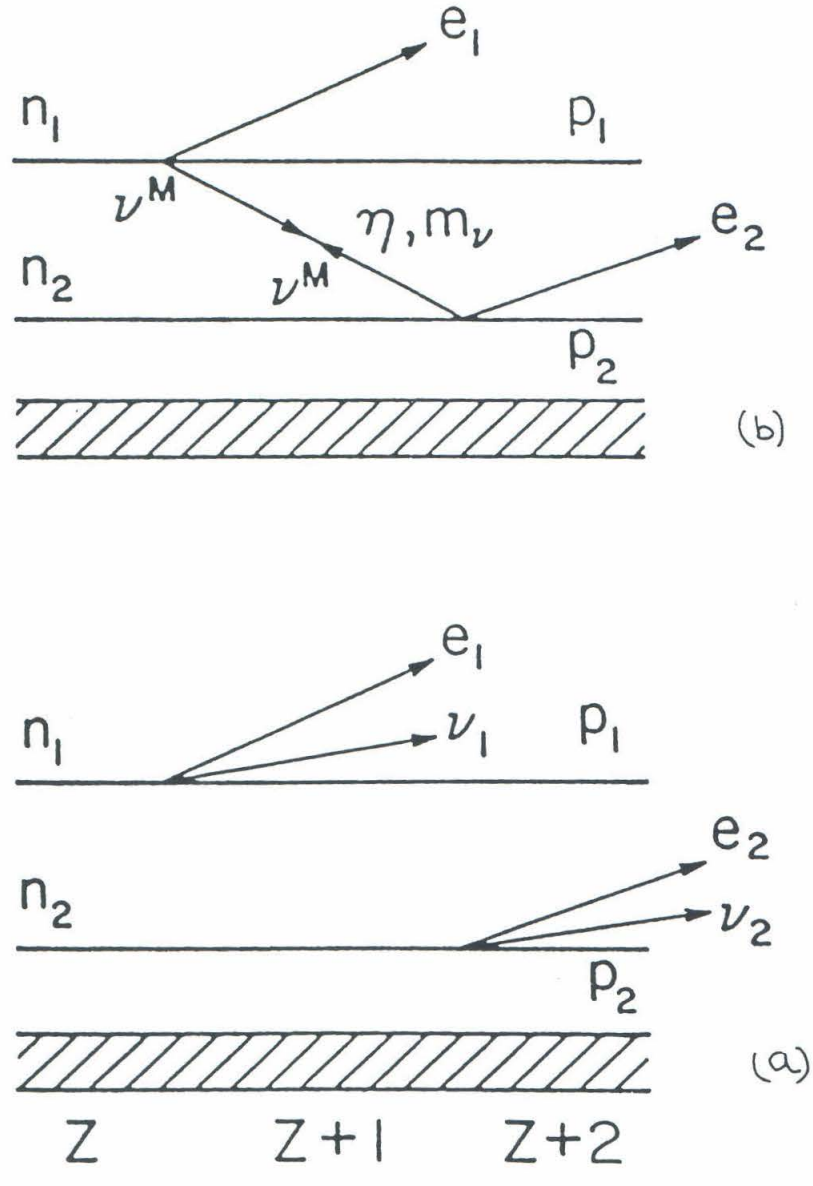

Figure (1.1) Schematic diagram for double beta decay in the two-nucleon mechanism. Part (a) is for the 2ν mode and part (b) is for the 0ν mode [15].

$$n_1 \rightarrow p_1 + e_1 + ''\nu''$$

$$''\nu'' + n_2 \rightarrow p_2 + e_2 .$$

The above is the so-called decay-absorption Racah Sequence. This sequence may proceed, provided that:

1) The neutrino emitted in the first decay is the antiparticle for the neutrino absorbed in the second decay.

2) The particle emitted by n_1 is a combination of two helicity states; in the minimum standard model, only purely right-handed antineutrinos are emitted and only purely left-handed neutrinos are absorbed.

These conditions require the neutrino to be a Majorana particle, since by definition it is its own antiparticle and since it is massive, it is not in a state of definite handedness.

The helicity matching requirement can be satisified if the neutrinos are massive and/or if the right-handed (V+A) current coexists with the V-A current in the weak interaction Hamiltonian. For a massive neutrino the right-handed helicity amplitude is proportional to m_ν/E_ν, where m_ν and E_ν are the neutrino mass and energy, respectively. The decay rate is expected to be proportional to the square of the neutrino mass and/or the square of the coupling strength of the right-handed current. As discussed in Boehm and Vogel [15] for neutrinoless double beta decay, a finite neutrino mass is always required even if right-handed interactions exist. Of course, in order for the $2\nu\beta\beta$ decay and $0\nu\beta\beta$ decay to become noticeable, single beta decay to the intermediate nucleus must be energetically forbidden or strongly hindered.

The dependence of the atomic mass M of the isotope (Z, A) on the nuclear charge Z determines whether or not the nucleus is energetically stable or undergoes a weak decay. Near its minimum this mass charge dependence can be approximated by a parabola [16]

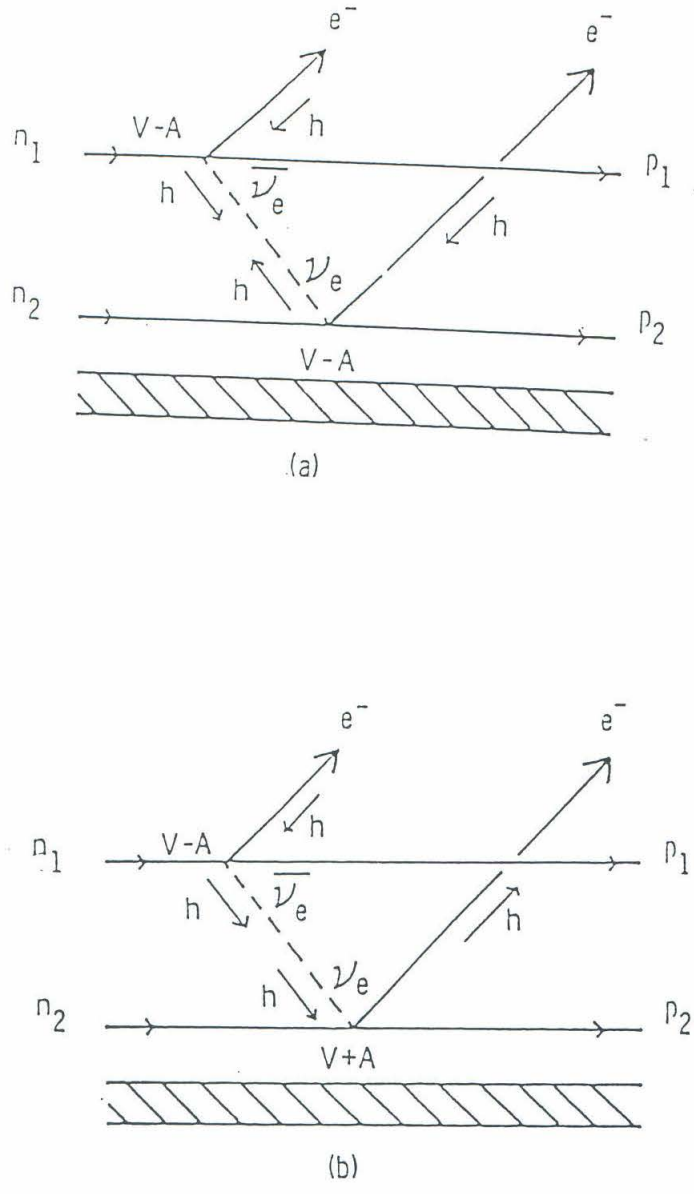

Figure (1.2) Schematic diagram of the 0ν mode of double beta decay in the two-nucleon mechanism. Arrows represent the main neutrino helicity in each vertex. Part (a) is for the left-handed lepton current in both vertices; part (b) is for the left-right current interference [15].

$$M(Z, A) = const. + 2b_{symm}\frac{(A/2-Z)^2}{A^2} + b_{coul}\frac{Z^2}{A^{1/3}} + m_e Z + \delta .$$

In the above expression, $b_{symm} \sim 50$ MeV is the symmetry energy coefficient and $b_{coul} \sim 0.7$ MeV is the Coulomb energy coefficient. The last term, δ, describes nuclear pairing. In a crude approximation it is given by

$$\delta \sim \pm 12A^{1/2} ,$$

for odd N, odd Z, or even N, even Z, respectively, while for odd A, $\delta = 0$. Thus, for odd A nuclei, typically only one isotope is stable whereas, because of the pairing term, for even A nuclei two parabolae exist, one for even-even nuclei and another, at a higher mass, for odd-odd nuclei. Hence, for a given even A, there exist two even-even nuclei, which are stable against both the electron and positron (or electron capture) decays. As these two nuclei usually do not have the same mass, the heavier one may decay into the lighter one through the second-order process of double beta decay.

Double beta decay candidates then have even N and Z; therefore, they have 0^+ ground states (zero angular momentum and even parity). If the two electrons emitted are in a zero angular momemtum state, then the final nucleus must be left in a 0^+ ground state or a 2^+ excited state. The decay to the 2^+ state is possible only if the mass of the 2^+ state in the final nucleus is less than the mass of the parent nucleus and, in the 0ν mode, if there is some form of right-handed coupling. If the V-A coupling is effective at both vertices, then the neutrino helicity must be the same at both. Thus, the virtual neutrino cannot carry angular momentum between the vertices. On the other hand, if some component of the V+A coupling is present, then the neutrino can carry one unit of angular momentum, thus making the 2^+ an accessible final state. Figure (1.3) shows the mass scheme for the decays.

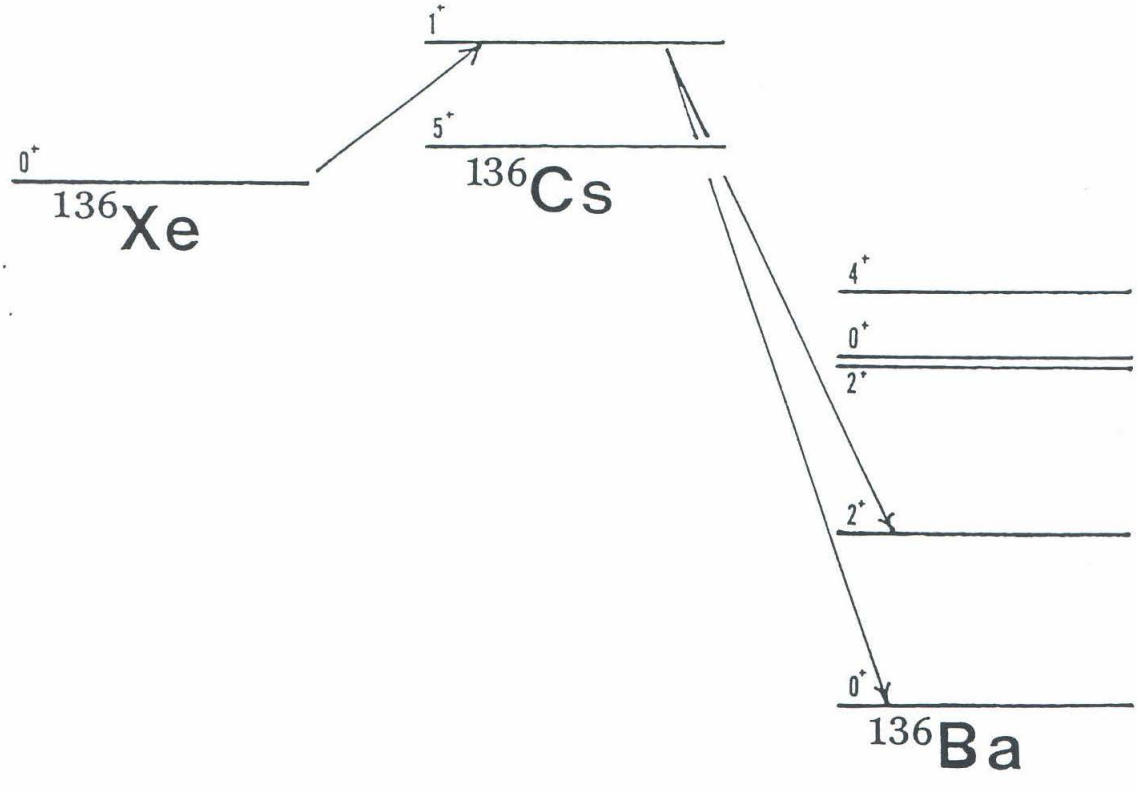

Figure (1.3) States participating in the double beta decay of ^{136}Xe. Principal decay branches are indicated.

1.4 Double Beta Decay Rates

1.4.1 The $2\nu\beta\beta$ decay rate

In this section an outline of the calculation of the decay rates for the 2ν and 0ν modes will be presented. The relationship between the 0ν decay rate and the neutrino mass and right-handed currents will also be given.

Fermi's Golden Rule and the second-order perturbation theory give:

$$d\lambda = 2\pi\delta(E_i - \sum_f E_f) \left| \sum_{m,\beta} \frac{<f \mid H_\beta \mid m><m \mid H_\beta \mid i>}{E_i - E_m - p_\nu - E_e} \right|^2 . \qquad (1.1)$$

Here $d\lambda$ is the partial decay rate; H_β is the Fermi Hamiltonian for the weak interaction; E_i, E_f and E_m are the energies of the initial, final and intermediate states, respectively; and p_ν and E_e are the momentum and energy of the neutrino and electron emitted in the first decay, respectively.

Typically, nucleons bound in nuclei have a binding energy of the order of 8 MeV and thus are essentially nonrelativistic. Also, the de Broglie wavelength of the outgoing leptons is much longer than the nuclear radius. Since the lepton current J_α, as it enters the transition amplitude $<f \mid H_\beta \mid i>$, needs to be known only within the spatial limits of the nuclear states and is practically constant within these limits, the value of J_α at the nuclear center can be used. The effect of these approximations is that the beta transition amplitude can be written as

$$<f \mid H_\beta \mid i> \sim \sqrt{2}g\left[C_V J_4 \int 1 - iC_A \vec{J}.\int \vec{\sigma}\right] ,$$

where

g = Fermi coupling constant

C_V = Vector coupling constant

C_A = Axial vector coupling constant

$$\int 1 \equiv \langle f \mid \sum_a \tau_+^a \mid i \rangle$$

$$\int \vec{\sigma} \equiv \langle f \mid \sum_a \tau_+^a \ \vec{\sigma}^a \mid i \rangle \ ,$$

the summation being over the nucleons in the decaying nucleus. J is the lepton current evaluated at the nuclear center. This is the so-called "*allowed approximation.* " The following terms are defined:

$$M^k_{m,i} = C_A \langle m \mid \sum_a \tau_+^a \sigma_k^a \mid i \rangle \text{ for } k = 1, 2, 3$$

$$M^4_{m,i} = C_V \langle m \mid \sum_a \tau_+^a \mid i \rangle .$$

$$J_\alpha(n_e n_\nu) = i u_e^+ \sigma_\alpha u_\nu \ ; \ \sigma_4 = -i \ .$$

For transitions in which the nuclear states have the same parity and differ at most by one unit of angular momentum, the nuclear and leptonic degrees of freedom can be separated. Thus, in the allowed approximation the transition matrices can be written:

$$\langle m \mid H_\beta(n_e, n_\nu) \mid i \rangle = -\sqrt{2} i g \sum_\alpha M_{m,i}{}^\alpha J_\alpha(n_e, n_\nu) \ ,$$

and the partial decay rate can be written as

$$d\lambda = 8\pi G_F^4 \cos^4\theta_c \, \delta(E_i - \sum_f E_f)$$

$$\times \left| \sum_{m\alpha\beta} M_{f,m}{}^\alpha M_{m,i}{}^\beta \sum_{n_e, n_\nu} (-1)^{n_e + n_\nu} \frac{J_\alpha^{n_e' n_\nu'} J_\beta^{n_e n_\nu}}{E_i - E_m - p_{n_\nu} - E_{n_e}} \right|^2 . \quad (1.2)$$

In this expression n_e = 1,2 for the first and second electron, respectively; similarly for the label n_ν, the index n' denotes the complement of n (if n=1 then n'=2). The intermediate states are labeled by m. Note that the matrix

elements are summed over all possible final states, and a minus sign has been introduced between all amplitudes that differ by the exchange of indistinguishable leptons in the final states. If the distinctions among the lepton energies contributing to the energy denominators in Equation (1.2) are neglected, then the term $E_{n_e} + p_{n_\nu}$ can be averaged to $(E_i - E_f)/2 = (M_i - M_f)/2$. In the allowed approximation, plane-wave modes (with corrections for the nuclear charge effects) can be used for the leptons, so the phase space factor is the numbers of the modes in the various momentum ranges. Since, as discussed by Haxton and Stephenson [18] and Doi et al. [19], the antisymmetry in the electron and antineutrino energies results in a strong suppression of the $0^+ \rightarrow 2^+$ transition, only the $0^+ \rightarrow 0^+$ transition will be considered. The intermediate odd-odd nucleus must be in the 1^+ state. When Equation (1.2) is multiplied by the phase space factor, summed over the lepton polarizations (taking into account the indistinguishability of the final lepton pairs), and integrated over the unobserved variables (terms linear in p_e and p_ν, which disappear after the integration over angles, are neglected), the following expression for the decay rate is obtained:

$$\omega_{2\nu} = \frac{G_F^4 Cos^4\theta_c}{8\pi^7} \int_{m_e}^{E_0 - m_e} F(Z,E_{e_1})\, p_{e_1}\, E_{e_1}\, dE_{e_1}$$

$$\times \int_{m_e}^{E_0 - E_{e_1}} F(Z,E_{e_2})\, p_{e_2}\, E_{e_2}\, dE_{e_2}$$

$$\times \int_{0}^{E_0 - E_{e_1} - E_{\nu 2}} \left| M \right|^2 p_{\nu_1}{}^2\, (E_0 - E_{e_1} - E_{e_2} - p_{\nu_1})^2\, dp_{\nu_1} \,. \qquad (1.3)$$

Here, M is the nuclear matrix element, which is given by:

$$M = \left| M_{GT}^{2\nu} - \frac{g_V^2}{g_A^2} M_F^{2\nu} \right| \,, \text{ where}$$

$$M^{2\nu}_{GT} = \sum_m \frac{<0^+_f \mid \sum_l \vec{\sigma}_l \tau^+_l \mid 1^+_m><1^+_m \mid \sum_k \vec{\sigma}_k \tau^+_k \mid 0^+_i>}{E_m - (M_i + M_f)/2}, \text{ and}$$

$$M^{2\nu}_{F} = \sum_m \frac{<0^+_f \mid \sum_l \tau^+_l \mid 1^+_m><1^+_m \mid \sum_k \tau^+_k \mid 0^+_i>}{E_m - (M_i + M_f)/2}. \qquad (1.4)$$

F(Z, E) is the Coulomb correction for the outgoing electrons. A nonrelativistic approximation (Primakoff and Rosen [20]) can be written as

$$F(Z,E) = \frac{E}{p} \frac{2\pi Z\alpha}{1 - e^{-2\pi Z\alpha}}.$$

This nonrelativistic approximation for F(Z,E) describes the shape of the total electron and single electron energy spectra quite well. However, the approximation cannot be used to calculate the total decay rate. Haxton and Stephenson [18], give a corrected value for the total decay rate based on a numerical evaluation of the Coulomb correction.

Using the nonrelativistic approximation for F(Z,E), the required integration can be done analytically. Thus, the expression for the summed electron kinetic energy spectrum, the decay rate, and the half-life of the decay can be obtained. Of primary interest from the experimental point of view is the sum electron spectrum:

$$\frac{dN}{dK} \sim K(T_0 - K)^5 \left[1 + 2K + \frac{4K^2}{3} + \frac{K^3}{3} + \frac{K^4}{30}\right],$$

where K is the sum of the kinetic energies of both electrons, and $T_0 = E_0 - 2$ is the maximum kinetic energy (K and T_0 are in units of electron rest mass). An example of a summed electron energy spectrum is shown in Figure (1.4). The half-life of the decay is given by :

$$\left[T^{2\nu}_{1/2}(0^+ \rightarrow 0^+)\right]^{-1} = G^{2\nu}(E_0, Z) \mid M \mid^2.$$

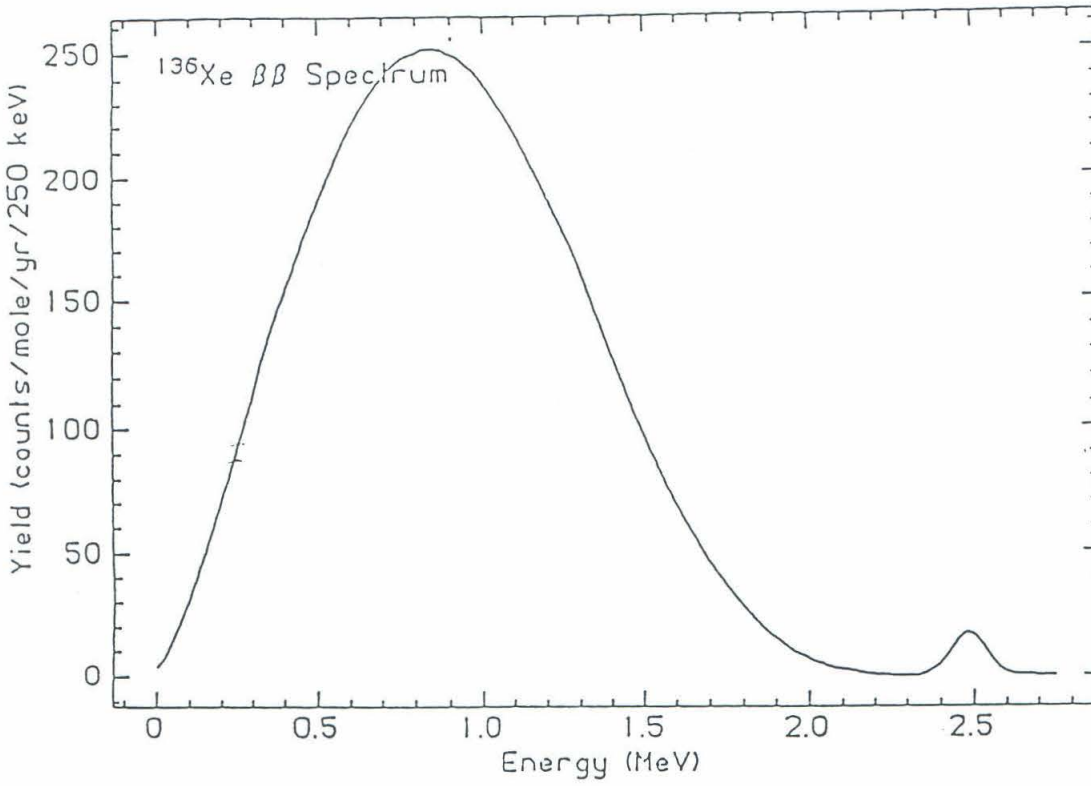

Figure (1.4) The energy spectra of electrons from the 2ν and 0ν decay of ^{136}Xe. The 2ν lifetime (3.8×10^{20}y) of Engel et al. [21] and the 0ν lifetime ($3\times10^{23} y/m_\nu{}^2$) of Klapdor and Grotz [22] was used in calculating these spectra. It was assumed that the neutrino has a mass of 2.5 eV and the detector resolution was 5 %.

The function $G^{2\nu}(E_0,Z)$ is the result of the lepton phase space integration and contains all the relevant constants. In fact, in the nonrelativistic Primakoff-Rosen approximation

$$G^{2\nu} \propto T_0^7\left[1 + \frac{T_0}{2} + \frac{T_0^2}{9} + \frac{T_0^3}{90} + \frac{T_0^4}{1980}\right].$$

1.4.2 The $0\nu\beta\beta$ decay rate

Figure (1.2) shows how neutrinoless double beta decay may proceed in the two-nucleon mechanism. As discussed earlier, in order for $0\nu\beta\beta$ decay, neutrinos are required to be massive Majorana particles. Right-handed currents make the rate go faster, but their existence is not sufficient for the 0ν decay because generally the emitted and absorbed neutrinos are different. The electron spectra and decay rates associated with the nonvanishing value of m_ν will be derived in this section. Details of the contribution of the right-handed currents can be found in [15].

The partial decay rate can be written

$$\omega_{0\nu} = 2\pi \sum_{spins} \left|R_{0\nu}\right|^2 \delta\,(E_{e_1} + E_{e_2} + E_f - M_i)\, d^3p_{e_1}\, d^3p_{e_2}\ ,$$

where $R_{0\nu}$ is the transition amplitude and includes both the lepton and the nuclear parts, and E_F is the energy of the final nucleus. Although $R_{0\nu}$ has a form similar to the amplitude in the 2ν case, it contains a neutrino propagator term in the lepton amplitude, which can be written as

$$-i\int \frac{d^4q}{(2\pi)^4} \frac{e^{-iq(x-y)}}{q^2-m_\nu^2}\, \overline{e}(x)\gamma_\rho \times \frac{1}{2}(1-\gamma_5)$$

$$\times(q^\mu\gamma_\mu + m_\nu)\times\frac{1}{2}(1-\gamma_5)\gamma_\sigma e^C(y)\ .$$

Here q is the four momentum carried by the virtual neutrino. Integration over

the virtual neutrino energy and over the space part $d\overline{q}$ lead to an expression representing the effect of the neutrino propagation between the two nucleons. The resulting expression, which has the form of a " *neutrino potential*, " H(r), appears in the nuclear matrix elements and makes the transition operator dependent on the coordinates of the nucleons as well as on the excitation energy $E_m - E_i$ of the virtual state. If it is assumed that the energy difference between initial and intermediate nuclear states is much smaller than the energy carried by the virtual neutrino, then the " *neutrino potential* " has the form:

$$H(r) = R/r\, e^{-r\, m_\nu},$$

where the nuclear radius, R, = $1.2\, A^{1/3}$. Also, in this approximation the sum over intermediate states can be performed by closure to give the following:

$$M^{0\nu}_{GT} \sim <0^+_f \mid R\sum_{lk} \vec{\sigma}_l \cdot \vec{\sigma}_k\, \tau_l^+\, \tau_k^+ \,/\, r_{lk} \mid 0^+_i > \qquad (1.5),$$

and

$$M^{0\nu}_{F} \sim <0^+_f \mid R\sum_{lk} \tau_l^+\, \tau_k^+ \,/\, r_{lk} \mid 0^+_i > \,. \qquad (1.6)$$

In Equations (1.5) and (1.6), the summation is over all the nucleons of the nucleus, and r_{lk} is the distance between the nucleons l and k.

The total rate is then

$$\left[T^{0\nu}_{1/2}(0^+ \rightarrow 0^+)\right]^{-1} = G^{0\nu}(E_0, Z) \left| M^{0\nu}_{GT} - \frac{g_V^2}{g_A^2} M^{0\nu}_F \right|^2 <m_\nu>^2 . \quad (1.7)$$

$G^{0\nu}$ is the phase-space coefficient and is proportional to:

$$G^{0\nu} \sim \int F(Z,E_{e_1}) F(Z,E_{e_2})\, p_{e_1}\, p_{e_2}\, E_{e_1}\, E_{e_2}$$

$$\times \delta(E_0 - E_{e_1} - E_{e_2}) dE_{e_1}\, dE_{e_2}$$

$$\sim \left(\frac{E_0^5}{30} - \frac{2E_0^2}{3} + E_0 - \frac{2}{5}\right),$$

where the Primakoff-Rosen approximation has again been used for F(Z,E).

The sum electron spectrum is a δ - function peaked at the endpoint energy E_0, a feature that makes the distinction between the 0ν and 2ν decay experimentally feasible.

If the additional terms for right-handed currents are included to the lowest order, the decay rate can be written [19] as a sum of six terms,

$$\left[T^{0\nu}_{1/2}(0^+ \to 0^+)\right]^{-1} = C_1 \langle m_\nu \rangle^2 + C_2 \langle \lambda \rangle \langle m_\nu \rangle + C_3 \langle \eta \rangle \langle m_\nu \rangle$$

$$+ C_4 \langle \lambda \rangle^2 + C_5 \langle \eta \rangle^2 + C_6 \langle \lambda \rangle \langle \eta \rangle \ . \qquad (1.8)$$

The quantities $\langle \lambda \rangle$ and $\langle \eta \rangle$ describe the coupling between the right-handed lepton current and the right-handed quark current, and the coupling between the right-handed lepton current and the left-handed quark current, respectively, and they also include the effects of neutrino mixing.

As well as the two-nucleon, double beta decay, other mechanisms are possible. These include decays mediated by the Δ isobar; Δ isobars are excited three-quark systems having all quarks in the s-state, coupled to spin S = 3/2 and isospin T= 3/2. They differ from a nucleon by a spin and an isospin flip of one of the quarks. Other possible mechanisms are transitions involving virtual Higgs scalars and a transition in which a light boson, the Majoron, is emitted with the two electrons. The Majoron is the massless Goldstone boson generated by the spontaneous breakdown of B-L (baryon number minus lepton number) symmetry [23]. The Majoron transition mode would, because of the three body phase space, give rise to a continuous spectrum peaked at approximately three quarters of the decay energy T_0. A discussion of the Δ isobar role is given in Boehm and Vogel [15], while Doi et al. [19] provide a discussion of the Majoron emission case.

1.5 Nuclear Structure and Double Beta Decay

In order to establish a connection between $\beta\beta$ experiments and the underlying weak interaction theory, the nuclear matrix elements have to be calculated. The nuclear matrix elements that have been defined in Equations (1.4) are all similar in structure. They consist of the wave function of the initial even-even nucleus in the 0^+ ground state, the wave function of the final even-even nucleus (usually in the 0^+ state but which can sometimes be in the 2^+ first excited state), and an operator connecting the two states. The procedure for evaluating the matrix elements would consist ideally of solving the nuclear, many-body problem with a realistic nucleon-nucleon interaction and of using a minimum number of approximations to find the required wave functions. Then, diagonalizing the resulting matrix would result in a straightforward evaluation of the matrix elements. However, except in the case of the lightest double beta decay candidates, such a procedure is technically not feasible. The first systematic work on the evaluation of matrix elements was an application of the shell model by Haxton et al. [24]. These shell model calculations consistently overestimate the rate for the 2ν mode especially in the case of ^{130}Te, where the experimental value for the matrix element is 9×10^{-3} [25] and the calculated value is 0.11 [23]. Theorists have searched for ways to resolve the discrepancy. Recently, an approach which involves a quasiparticle random phase approximation (QRPA) has been applied to the matrix element calculation [21].

A detailed discussion of the nuclear structure issues is presented in Boehm and Vogel [15], and Haxton and Stephenson [18]. The conclusion is that the precise calculation of the nuclear matrix elements for both modes of double beta decay is a difficult and as yet unsolved problem.

1.6 Experimental Studies of Double-Beta Decay

To date experimental searches for $\beta\beta$ decay can be divided into three categories:

1. Geochemical Experiments: Ores (or meteorites) that are of the order of 10^9 years old and rich in the isotope expected to undergo $\beta\beta$ decay have been examined. By extracting and measuring the quantity of the daughter nuclei present, an estimate of the decay rate of the parent can be made. Since the half-lives for double beta decay are so long (typically 10^{21} years), the technique has been successful only in those cases with noble gas daughter nuclei, whose natural abundances in ores are so low that any isotopic anomalies produced by $\beta\beta$ decay are measurable. Difficulties associated with this method include: uncertainties in the age of the ore, incomplete knowledge of the geological history of the ore and limitations on the sample size. This method also cannot distinguish between the various decay modes. The technique has been applied to the decays of $^{82}Se \rightarrow ^{82}Kr$, $^{128}Te \rightarrow ^{128}Xe$, and $^{130}Te \rightarrow ^{130}Xe$. A summary of the results is presented in Table 1.1 [15]. Prior to the work performed by Elliot et al. [26], the only positive results on $\beta\beta$ decay were from geochemical experiments.

2. Radiochemical Experiments: These experiments differ from geochemical ones in that the accumulation occurs over a known time interval in a carefully controlled environment. Because the accumulation time is now much shorter, it is essential that the sample be purged of naturally occurring daughter atoms. Thus, in these experiments decays with short-lived daughter isotopes are used. Prior to 1986 only one such milking experiment had been performed. The isotope under investigation was ^{238}U; while it can decay by alpha decay as well as by spontaneous fission, it cannot beta decay to ^{238}Np. Double beta decay would transform it into ^{238}Pu which has a 5.51 MeV alpha decay with a half-life of 87.4 years. In 1950 Levine et al. [27], extracted plutonium from a six-year old UO_3 sample and searched for the alpha decay of

the ^{238}Pu. No alpha particles were seen, and a lifetime limit of $T_{1/2} > 6\times10^{18}$y was established. At present a reexamination of this decay is planned [28]. This plan will use a 1000 kg sample of uranium and separate the plutonium every 4 months. The expected lifetime sensitivity is of the order of 2×10^{22}y. Another such laboratory experiment under development involves ^{136}Xe [29]. In this experiment, it is hoped that the decay can be observed by separating the ^{136}Ba daughter nuclei and counting them, using multiphoton ionization techniques.

3. Direct Detection Experiments: In these experiments the energy of the electrons emitted in the $\beta\beta$ decay is measured. Thus, it is feasible to distinguish the 0ν from the 2ν mode, since the characteristic signature of the former would be a monochromatic peak in the energy spectrum, whereas the spectrum of the latter would be a continuum with a broad maximum peaked at half of the decay energy. Examples of the sum electron spectra for the two modes are shown in Figure (1.4). To date many direct detection experiments have been performed, but it is only recently that their sensitivities have matched that of the geological methods. Included in this class of studies are the high-resolution spectroscopy experiments in ^{76}Ge ([30], [31], [32], [33], [34], [35]); high pressure ^{136}Xe experiments ([36], [37]); and track recognition experiments in ^{48}Ca [38], ^{82}Se [26] and ^{136}Xe ([39], [40]). The experiment described in this thesis belongs to the last class of experiments. Also included are the coincidence experiments in ^{100}Mo and ^{150}Nd. Apart from the unpublished reports on the evidence of the Majoron mode in ^{76}Ge [41] and the 2ν mode in ^{82}Se [26], all the published results are negative. The half-life limits are summarized in Table 1.1

1.7 Neutrinoless $\beta\beta$ decay data and current neutrino mass limits

To date ^{76}Ge is probably the best explored neutrinoless double beta decay. Using the calculated values of the coefficients C_i [19], Equation (1.8) and $T_{1/2} \geq 1\times10^{23}$y [42], the following upper bounds for the parameters $<m_\nu>$, $|<\eta>|$, and $|<\lambda>|$ are obtained:

$$<m_\nu> \leq 2\text{-}16eV\,,\ |<\eta>| \leq 0.0025\,,\ \text{and}\ |<\lambda>| \leq 0.004\ .$$

	Spectroscopic experiments					
	^{48}Ca	^{76}Ge	^{82}Se	^{100}Mo	^{150}Nd	^{136}Xe
$T_{1/2}(0\nu) >$	2×10^{21}	4×10^{23}	7×10^{21}	2.1×10^{21}	7×10^{19}	1.2×10^{21}
$T_{1/2}(2\nu) >$	3.6×10^{19}	8×10^{20}	1×10^{20}		1.3×10^{19}	1.8×10^{19}

	Geochemical experiments		
	^{82}Se	^{128}Te	^{130}Te
$T_{1/2}(0\nu,2\nu)$	$(1.3\pm0.05)\times10^{20}$	$> 8\times10^{24}$	$(2.6\pm0.3)\times10^{21}$

Table (1.1) Experimental half-lives (y) for double beta decay [15].

CHAPTER TWO

The ^{136}Xe Double Beta Decay Experiment

2.1 Criteria for a feasible double beta decay experiment

An examination of the data in Table 1.1 of Chapter 1 reveals the extremely long half-lives, of double beta decays. Because of such long half-lives the count rate is low; for example, a one-mole sample of an isotope having a half-life of 10^{23}y would generate only 4 disintegrations per year. To be sensitive to such a count rate, a direct detection experiment must include a source with a large number of candidate decay nuclei and a detector that measures the kinetic energy of the two electrons emitted in the decay. The detector must be capable of discriminating between the electrons produced by double beta decay and the background of electrons produced by other events. The main contributions to this "sea" of background electrons come from cosmic ray muon interactions, the decay of radioisotopes in the detector system and its shielding, the decay of radioisotopes produced by cosmic ray neutrons and neutrons generated by the spontaneous fission, or (α, n) reactions in ^{238}U (which is present in most environments), and the interactions between atomic electrons and gamma ray photons emitted in the decay of the foregoing radioisotopes. A detailed discussion of the background problem is presented in Chapter 5. From the preceding discussion, it is evident that a viable double beta decay experiment must meet the following requirements:

1. The source must contain a large number of candidate decay nuclei. The decay candidate should be available in a reasonable, natural isotopic abundance. The transition energy (Q) of the decay preferably should be higher than 2 MeV. Most of the gamma lines from the natural decay chains have

an energy below 2 MeV, so for a candidate with a decay energy above this point there will be much fewer gamma lines that can generate background electrons near the expected 0ν line. Also, as shown in Chapter 1, the transition rate depends on the phase-space factor, which in turn depends on Q_O^{11} for the 2ν mode and depends on Q_O^5 for the 0ν mode.

2. The source and the materials used in the construction of the detector should contain the minimum amount of possible radioactive contaminants.
3. In order to reduce the background generated by cosmic ray muon interactions, it should be possible to install the experiment in a deep mine or a tunnel with a large overhead burden, and a low environmental radioactivity level. Further, the size of the source-detector system should be such that it is possible to surround it with shielding and so reduce the effect of environmental radioactivity.
4. The total kinetic energy of the two electrons emitted in the 0ν mode is always equal to the decay energy Q_0. Hence, the detector should have sufficient energy resolution to distinguish the $0\nu\beta\beta$ electrons from the $2\nu\beta\beta$ continuous electron spectrum.

2.2 ^{136}Xe as a $\beta\beta$ Candidate

^{136}Xe is a very promising candidate for a double beta decay experiment for the following reasons:

(1) The Q value for the single beta decay (^{136}Xe→^{136}Cs) is -69 keV; i.e., energetically, this decay is forbidden.

(2) The Q value for the double beta decay, (^{136}Xe→^{136}Ba), is 2.48 MeV. This is slightly higher than the 2.04 MeV of ^{76}Ge (the experiment with the current highest limit for the 0ν decay half-life). The result is an increase in the rate because of the phase space factor.

(3) The natural abundance of ^{136}Xe is 8.87%, and it is possible to have a

system with a very large number of atoms without isotopic enrichment. ^{136}Xe can also be obtained as an enriched isotope.

(4) Xenon can be used in a time projection chamber, (TPC). Thus, as in the germanium experiment, the detector will act as the source. In other experiments, the double beta decay source has been in the form of plates, foils or wires. Because the source has to be thin in order to meet the required energy resolution criterion, the amount of beta active material cannot be very large. By having the source as detector, the source thickness is not limited, and also a 4π solid angle for the decay is achieved.

2.3 The Time Projection Chamber

It was in the 1970's, in the midst of discussions on the proposed new generation of detectors for the "positron-electron project" or PEP collider, that D. Nygren [43] invented the TPC. The TPC can reconstruct the tracks of charged particles in three dimensions and can also identify particles by measuring the ionization energy that they deposit along their tracks. Along with being able to make these measurements over a large solid angle, the TPC can also do the same in those cases where a large number of tracks are simultaneously created.

A schematic of a TPC is shown in figure (2.1). Basically, the TPC consists of a large closed chamber filled with a gas with a high electron mobility factor and a small electron attenuation coefficient. As charged particles pass through the TPC, they ionize the gas, producing tracks of electron-ion pairs. The amount of energy they deposit depends on both their charge and their velocity. A uniform electric field (uniformity is ensured by the field shaping rings) is applied in the axial direction. Under the influence of this electric field, the secondary electrons formed in the ionization process drift toward the readout plane located at one end of the TPC. Their arrival time at the readout plane together with the known drift velocity allows the determination of the spatial

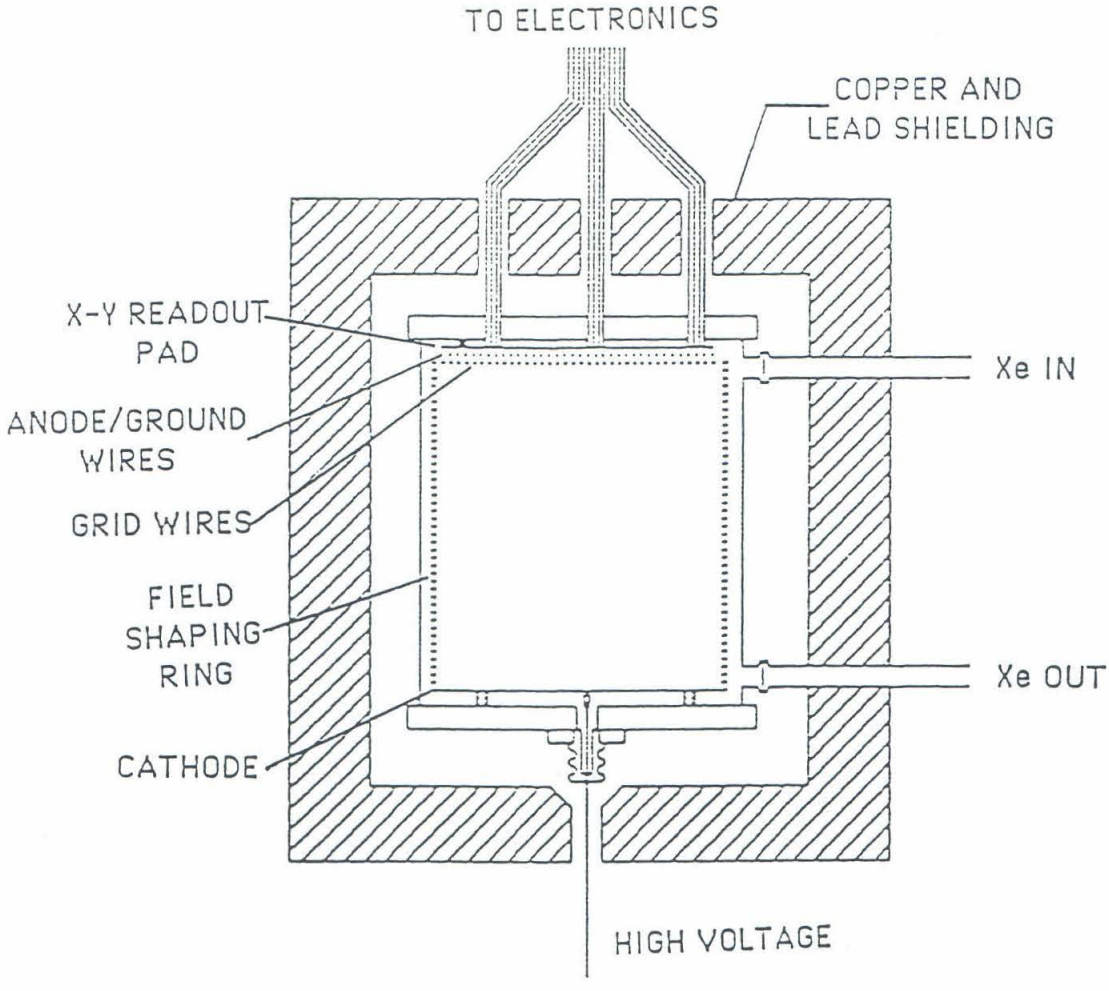

Figure (2.1) Schematic representation of the TPC.

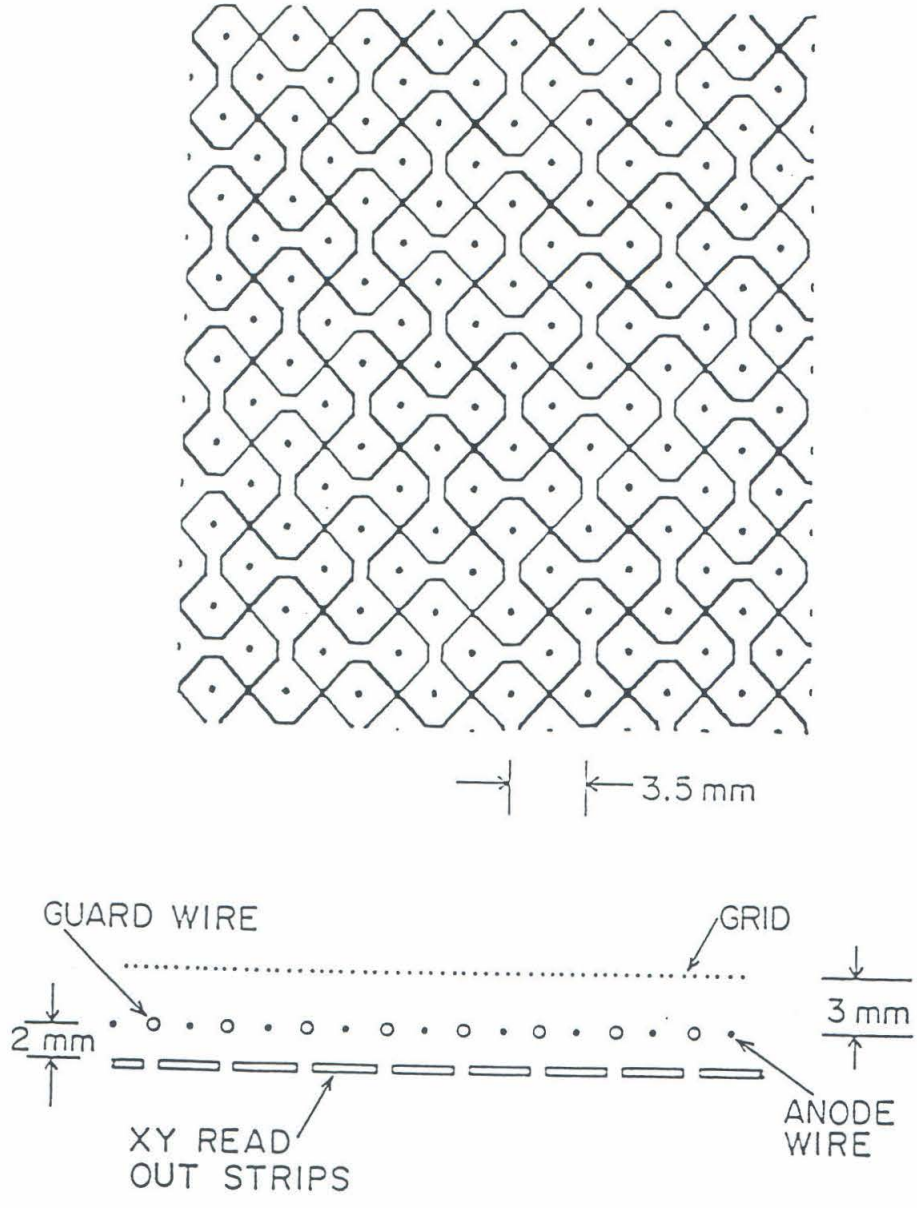

Figure (2.2) The upper section of the diagram shows the pattern of the X-Y readout system. The black lines represent regions where the copper has been etched off the circuit board. The dots represent the plated through holes. The x channels are horizontal and the y channels are vertical. The lower section of the diagram shows the relative position of the grid, guard wires, and anode wires and the X-Y readout pads.

coordinate of the track in the drift direction (hence, the name *time projection* chamber). A schematic of the readout system is shown in Figure (2.2). At the readout plane the secondary electrons undergo charge multiplication near a set of anode wires that are held at a positive high voltage. The signals from these wires are used to look at the energy deposition along the track. The charge multiplication at the anode wires induces signals on an orthogonal set of readout pads, located a few mm away. The point at which the signal is induced gives the x-y coordinates (or the appropriate coordinates in any other frame).

Excellent background rejection can be achieved using both the track recognition and the ionization measurement ability of the TPC. A typical electron track generated in the TPC is shown in Figure (2.3a). The following features are to be noted:

(1) The beginning of the track is relatively straight and the ionization density is constant.

(2) As the electron slows down near the end of the track, large angle scatterings are numerous, and as a result the ionization density increases giving rise to high ionization "blobs."

The characteristic signature for a $\beta\beta$ decay event is a continuous track with high ionization (or charge) blobs and large angle scatterings at both ends. In contrast, tracks formed by cosmic ray muons are straight and have a constant ionization deposition throughout the track. An example is shown in Figure (2.3b). Alpha particles generate short tracks with highly localized charge depositions.

2.4 Experimental Objectives

Using the calculations of the nuclear matrix elements associated with the $0\nu\beta\beta$ decay [21], a lifetime of 10^{24} y gives an upper limit of 2 eV for the neutrino mass. Hence, to be sensitive to such a value for the neutrino mass, the

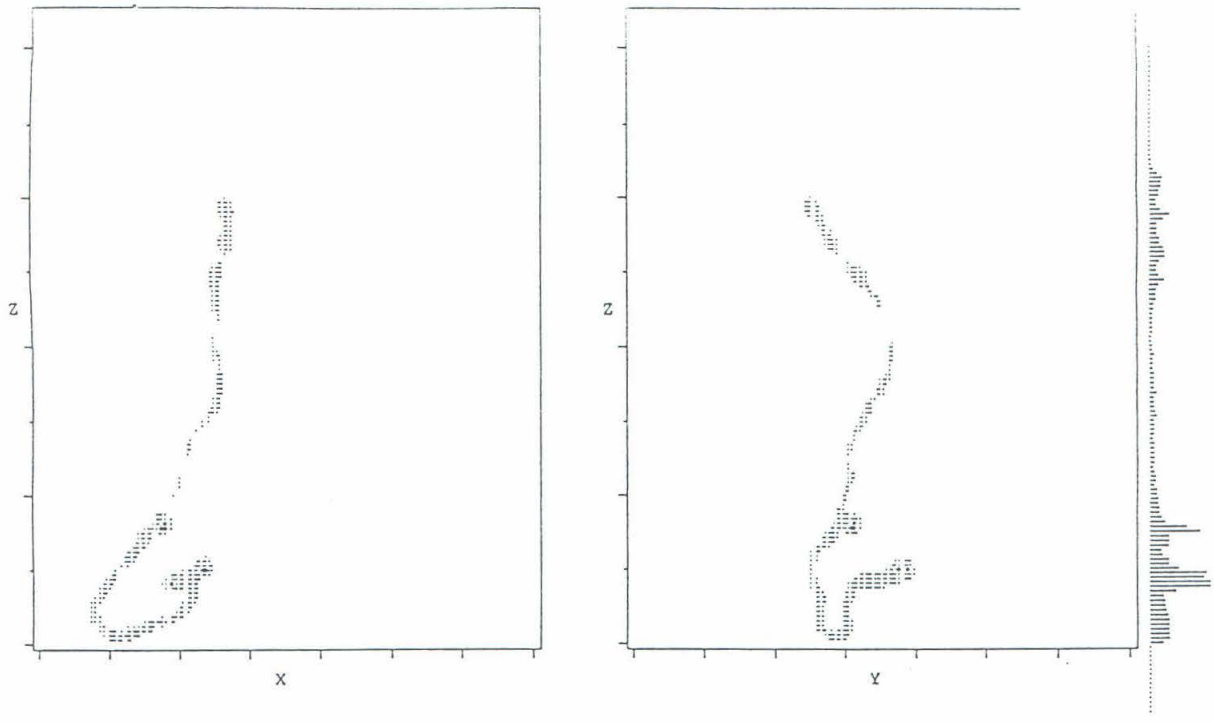

Figure (2.3a) The xz and yz projection of an electron track. The energy deposited by the electron as a function of the drift time is shown on the right-hand side.

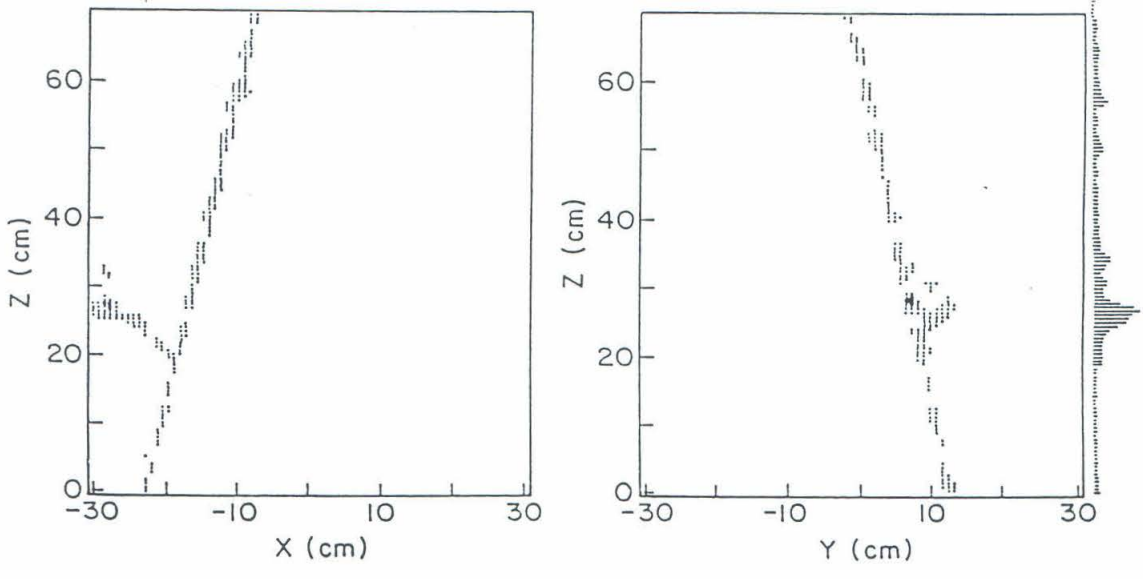

Figure (2.3b) The xz and yz projection of the track formed by a cosmic ray muon as it ejects a delta electron. The energy deposited by the muon as a function of the drift time is shown on the right-hand side.

experiment must be capable of detecting and identifying a few counts per year. Since the TPC can provide a very effective background rejection through its combination of track reconstruction, energy loss (dE/dx), and total energy measurements, it is particularly suited for a sensitive search for double beta decay. In theory, there is no limit to the amount of xenon that can be put into a high pressure gas TPC. In practice, because of physical limitations (a detailed discussion of these limitations is presented in Chapter 5), the pressure is limited to about 10 atm, and so the amount of xenon is limited accordingly. Still, the number of available candidate nuclei for decay is quite high relative to other $\beta\beta$ experiments. With an active volume of 208 litres and an operating pressure of 5 atm, the TPC can accommodate 28 moles of 60% enriched ^{136}Xe. This is to be compared with the 7 moles of ^{76}Ge contained in the largest Ge detectors built to date [15]. The following are the goals of the TPC:

a) *Track Reconstruction:* Track reconstruction provides an excellent means of background suppression. In the TPC used in this experiment, the anode wires are connected together through a low-noise, high-gain, current sensitive preamplifier. The x-y coordinates are obtained from the charges collected on an orthogonal set of readout strips located in a single plane. A detailed Monte Carlo study (to be discussed in Chapter 4) showed that electrons going through xenon gas at high pressure undergo a large amount of multiple scattering. As a consequence, good spatial resolution cannot be obtained from a center of gravity fit to the track; thus, the spatial resolution is determined by the configuration of the x-y readout strips. Because of the diffusion of the secondary electrons over the drift distance, the resolution is ultimately limited to about 2 mm.

b) *Energy Resolution:* The total energy of the two electrons emitted in the $0\nu\beta\beta$ decay of ^{136}Xe is 2.48 MeV. In order to distinguish this signal both from the 2ν mode (which consists of a broad spectrum peaked at 0.8 MeV and a tail extending to 2.48 MeV) and from background events, good energy resolution is

critical. The energy of an event is measured by integrating the signals from the anode wires during the drift time. A resolution of 5% at 2 MeV seems to be a realistic goal.

c) *dE/dx Measurement:* Since the large number of multiple scatterings experienced by an electron complicates the recognition of the vertex of the track generated in a $\beta\beta$ event, it is difficult to distinguish between single-electron and two-electron tracks on the basis of track reconstruction alone. However, by measuring the dE/dx along the track, it is possible to detect the larger charge deposition (charge "blobs") at the end of the tracks and thus locate the end of a track. The Monte Carlo study indicated that with a resolution of 3.5 mm in all directions, the charge deposited in the last centimeter of a track is at least four times larger than the charge deposited along the rest of the track. This Monte Carlo result suggested that a readout system consisting of two threshold levels instead of full digitization should be sufficient to recognize the charge blobs with an adequate efficiency. A two-level system and a spatial resolution of 3.5 mm in both the x and y direction have been adopted.

2.5 Previous Experimental Studies of Double Beta Decay in ^{136}Xe

In the Baksan Neutrino Laboratory in the USSR at a depth of 850 meter water equivalent (mwe), Barabash et al. [44] have explored the double beta decay of ^{136}Xe, using a 3.14 liter ionization chamber pressurized to 25 atm with xenon, enriched to 93% with ^{136}Xe, and an admixture of 0.8% H_2 (to improve the drifting of electrons). Thus, the number of moles of ^{136}Xe amounted to about 3.3 moles. No excess counts were seen at the decay energy and the limits obtained were $T^{0\nu}_{1/2} > 1.2\times10^{21}$y and $T^{2\nu}_{1/2} > 1.8\times10^{19}$y. The runtime for the 0ν result was 243 hours and the runtime for the 2ν result was 120 hours. Meanwhile, an Italian group [39] is working with a multielement, xenon proportional chamber in the Gran Sasso Underground Laboratory in Italy. Their

chamber has an active volume of 80 liters, operates at 9.5 atm, and has an energy resolution of 4% at 1.5 MeV. After a run time of 846 hours, the limit obtained for the 0ν decay mode was $T^{0\nu}_{1/2} > 1.8\times10^{21}$y. Preliminary studies are also under way to measure the double beta decay lifetime of ^{136}Xe by counting the ^{136}Ba daughter atoms using multiphoton ionization techniques [29]. The expected sensitivity to the 2ν lifetime, using a sample of 10 moles of xenon gas, is 10^{20} years.

After a runtime of one year it is expected that the experiment described in this thesis is capable of reaching a half-life sensitivity of 1.2×10^{24} years. From existing calculations of the nuclear matrix elements associated with the decay [21], an upper limit of 2.3 eV for the neutrino mass $<m_\nu>$ should be achieved.

CHAPTER THREE

Study of a Prototype Xe TPC

3.1 Introduction

This chapter describes the studies performed with a prototype TPC. This prototype was built and used to assist in optimizing the various parameters of the full-scale TPC. It had a volume of about 1 liter, operated at 1 atm, and had 16 readout channels. For comparison, the final system has a volume of 208 liters, operates at 5 atm, and has 336 readout channels. Among the very important issues studied with this prototype were the gas handling system, the readout electronics, and the choice of a "magic gas" which, when added to pure Xe, would increase the electron drift speed and suppress the diffusion. Also investigated was the possibility of using the scintillation properties of Xe as a time-zero signal. However, the prototype TPC was too small and the spatial resolution too coarse to see the charge blob produced by the increased dE/dx, which is deposited by the low-energy electrons at the end of a track. To obtain some realistic tracks to further study these charge blobs, a Monte Carlo code was developed to generate tracks in the TPC. This work is described in Chapter 4.

3.2 Description of the Prototype System

A schematic of the prototype TPC is shown in Figure (3.1). Basically, it consisted of a drift region and a readout system. The drift region was composed of a 10 cm copper cathode plane separated from an anode wire plane by two field shaping rings and a Frisch grid. To generate a uniform electric field inside the TPC, the field shaping rings were connected to a voltage divider. The Frisch grid was kept at ground potential and thus isolated the readout system from the drift region. This drift region was mounted on a Delrin slab, which held the 16-channel readout system. The readout system consisted of 8 anode wires (having a diameter of 20 μm) spaced 1 cm apart. In an effort to reduce the cross talk between anode wires, guard wires (having a diameter of 50 μm) were installed between adjacent anode wires. A set of eight 1 cm copper pads were mounted above (and perpendicular to) the anode wire plane on the Delrin slab, using a high-vacuum epoxy. In this configuration the anode wires and the copper pads formed a 2-D readout system. The readout system along with the drift region was mounted on a conflat flange, and the whole assembly was placed inside a stainless steel vessel with a volume of about 1 liter. To study the scintillation light, an ultraviolet photomultiplier tube viewed the system through a sapphire window.

3.3 The Gas Handling System

A schematic of the gas-handling system is shown in Figure (3.2). It consisted of a purifier, a circulating pump, a high-vacuum pumping station, a manifold, and reservoirs that were used for gas storage. Before filling the chamber with a gas, the chamber was first pumped down to a high-vacuum state. To

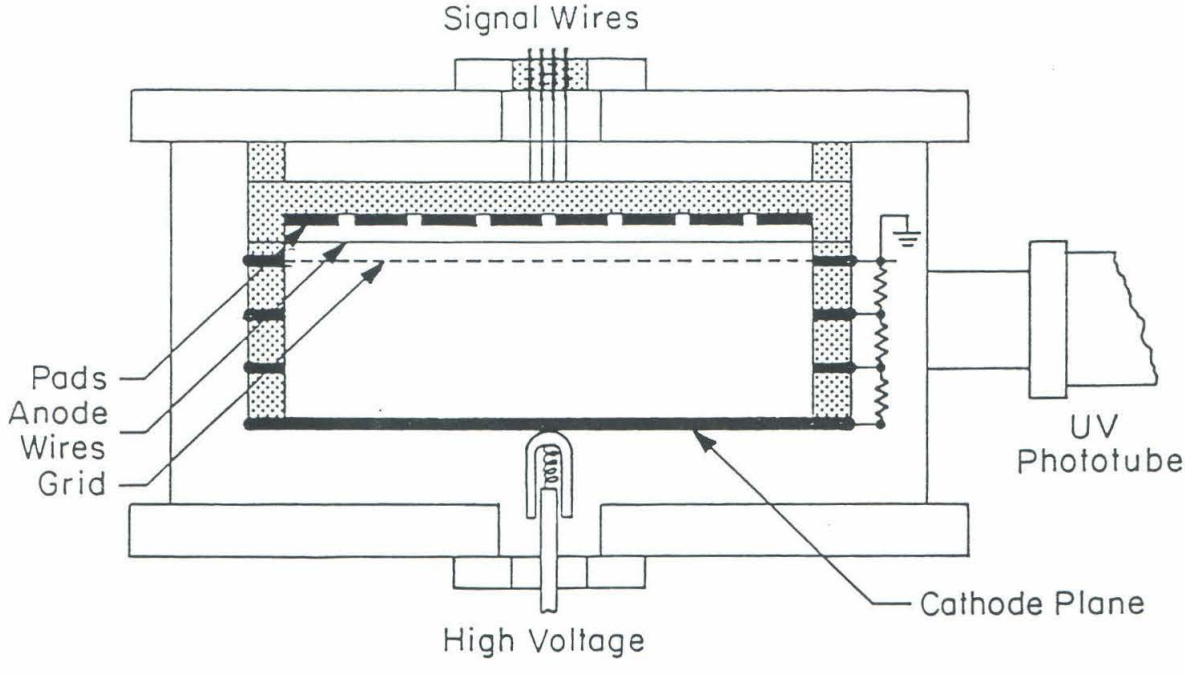

Figure (3.1) Schematic diagram of the prototype xenon TPC.

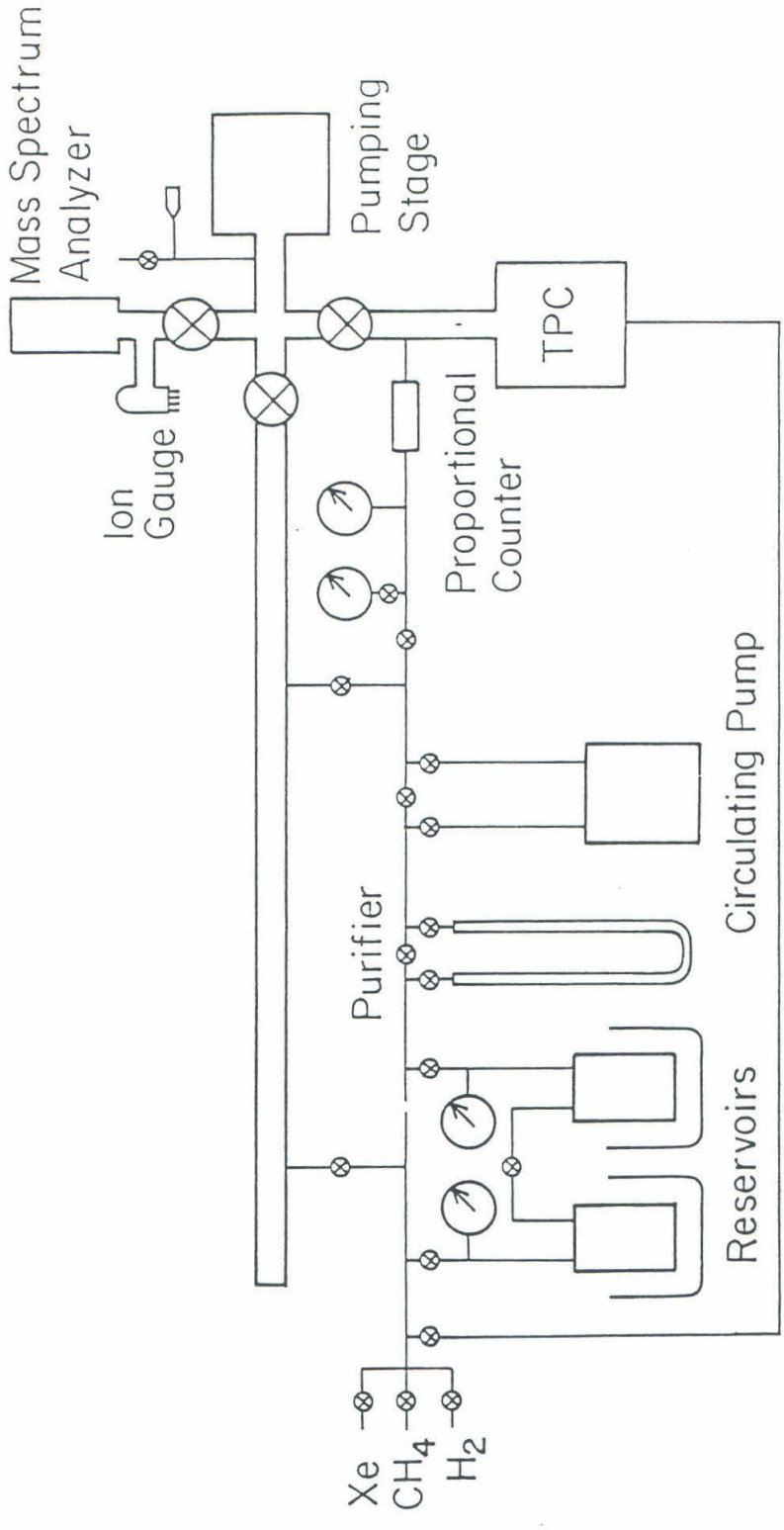

Figure (3.2) Schematic representation of the gas handling system.

monitor possible contaminants, an on-line, mass spectrum analyzer (Model M-100, Dycor Electronics Inc.) was connected to the system. Since xenon is very susceptible to contamination, the gas had to be constantly circulated through a purifier using a metal bellows pump (Model MB-302, Metal Bellows Corp.). Initially, a commercial purifier (Hydrox Purifier, Model 8301) was used to remove contaminants like O_2 and water vapor. However, it was found that this purifier also removed N_2 from the gas mixture. Since measurements with N_2 as an admixture in the fill gas were required, a new purification system was developed.

It was possible to operate this purification system at room temperature and once overloaded, it could be easily regenerated. The purifier consisted of two stainless steel columns which contained MnO and molecular sieve (4A). The MnO removed O_2 from the circulating gas while the molecular sieve trapped water molecules. Both O_2 and water vapor are undesirable since they are electronegative and remove the drifting electrons by forming negative ions. The gas-handling system also had two stainless steel reservoirs where the fill gas could be condensed with liquid nitrogen. The two reservoirs were found to be very useful for the temporary storage and purification by fractional distillation of certain gas mixtures.

3.4 The Readout Electronics

During the charge multiplication, the anode wires produced a negative pulse. Each wire was connected to a current sensitive preamplifier (based on the LeCroy TRA 1000), which generated a fast pulse with a few hundred nanosecond time constant. The pulses from the pads had opposite polarity

because they were produced by the image charges. To produce the same polarity signals from all the channels, the inverted output from the pad preamplifiers were used. The preamplifier signals were then shaped and amplified by shaping amplifiers. With this prototype, precise information about the total energy or the dE/dx along the track could not be obtained. However, using the available electronics, it was possible to reconstruct the tracks of charged particles. To do this, the output signals of the shaping amplifiers were converted into TTL signals. At this point all the energy information from the pulses was lost, and they were used for timing purposes only. The TTL signals from the anode wires and the pads were then fed into two 2K x 8 RAM ICs so that each bit of the 8-bit word corresponded to a channel. A start (or time-zero) signal set the RAM ICs in the write state and at the same time started incrementing the address with a 5 MHz clock so that each address corresponded to a time bucket of 200 ns. The address counter stopped after a predetermined time, and the status of each channel was stored in the RAM as a function of time. The RAMs were then read by the computer (PDP 11/23) using a CAMAC dataway. A simple CAMAC decoder was designed, which interfaced the RAMs and the associated electronics with the computer.

3.5 Results

3.5.1. Scintillation

Scintillation is a complex process involving the formation of diatomic molecules ([45], [46], [47]) during three-body collisions. Xenon, which is a good scintillator, has a light output that is about seven times greater than the light output of argon [48]. The continuous emission spectrum is broad (1475-

2200 Å). The sharp atomic lines at 1473 Å can be seen only at very low pressures. Originally, it was planned to use the primary scintillation as the time-zero trigger in the TPC. However, after extensive research, it was concluded that it is not possible to have good imaging and energy resolution simultaneously with a good scintillation yield.

The fact that xenon scintillates in the far UV region complicates light detection. Either a phototube with a special UV window (e.g., MgF_2, LiF_2) or a wavelength shifter in conjunction with an ordinary glass window is required. Several wavelength shifters, including p-Quaterphenyl, p-Terphenyl butadiene and Tetraphenyl butadiene were used. All of these, especially scintillation grade Tetraphenyl butadiene, worked very well. A pyrex glass window was coated by vapor deposition with the wavelength shifters. The UV-to visible conversion was insensitive to the film thickness in the range 50 to 300 $\mu g/cm^2$. However, because these wavelength shifters were organic compounds, special handling precautions had to be followed while using them in a system containing pure xenon, such as coating the wavelength shifter with a thin layer of MgF_2.

Undoped xenon generates the maximum light output. In the TPC, xenon cannot be used in the pure form because the drift velocity of electrons in pure xenon is known to be small, [49] and as a consequence, the diffusion of the electrons is large. Since this experiment has a low count rate, a large drift velocity that would sweep the charges to the readout plane as soon as possible is not essential. However, the diffusion of the electrons would severely limit the spatial resolution. In pure xenon at atmospheric pressure, it was found that electrons in the presence of a drift field of 100 V/cm diffuse almost 1 cm in a drift distance of 1 m [50]. By adding hydrocarbons (CH_4) or molecular gases (CO_2), which thermalize the electrons, the diffusion rate can be reduced.

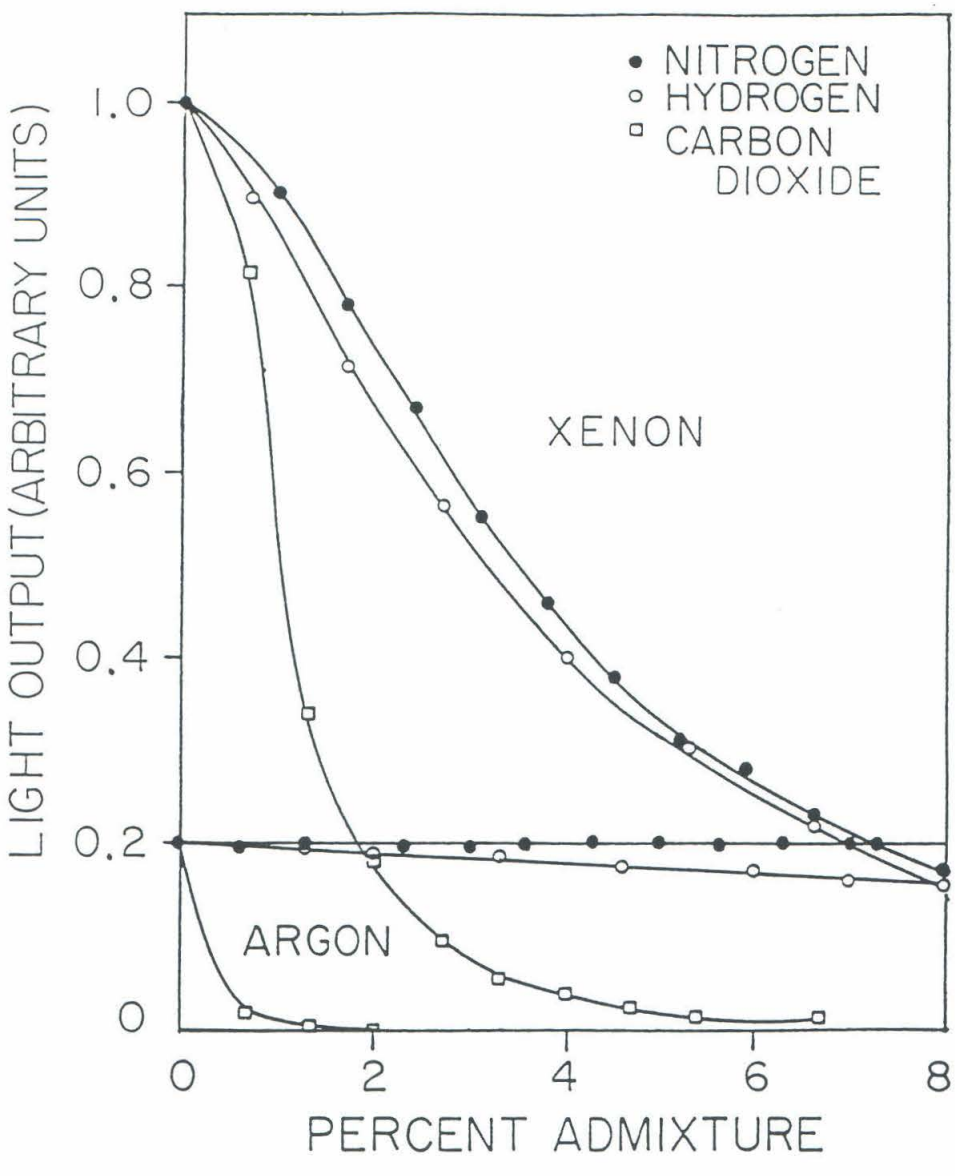

Figure (3.3) The scintillation light yield of xenon and argon as a function of different gas mixtures.

Several gas mixtures designed for improving the drift and diffusion properties were added to xenon, and the resulting scintillation was studied. For a comparison the process was repeated, using argon. The results are shown in Figure (3.3) for admixtures of N_2, H_2 and CO_2 to xenon and argon. It was found that a small admixture (less than 1%) of CH_4 and C_2H_4 quenched the scintillation light in xenon and argon. It can be seen that using the system described above that the light output in xenon was at at least a factor of 5 higher than the light output in argon. In argon, N_2 works as a wavelength shifter, and the UV light lost in the quenching process is transformed into visible light, resulting in a minimal net loss. However, in the case of xenon, the above is not true. The conclusion of the study was that gas admixtures (CO_2, CH_4) that improve the drift and diffusion drastically cut down the scintillation yield.

The phenomenon known as secondary scintillation was also found to be a strong hindrance to using scintillation light as a time-zero trigger. In addition to the primary light, the drifted electrons generate some secondary scintillation in pure xenon. This scintillation is produced by the collisions of the electrons in the very strong electric fields present around the anode wires. The secondary scintillation starts well before the charge multiplication, and at the working voltage the intensity is typically a few orders of magnitude stronger than that of the primary scintillation. The background produced by the secondary scintillation made the time-zero triggering particularly difficult even when using a clever timing scheme. The far UV nature of the scintillation also increased background problems through the production of photoelectron emission from the walls of the detector. This was clearly demonstrated by the signals generated when pure xenon was contained in a cylindrical proportional counter, 2.5cm in diameter. The successive pulses generated by the photoelectrons

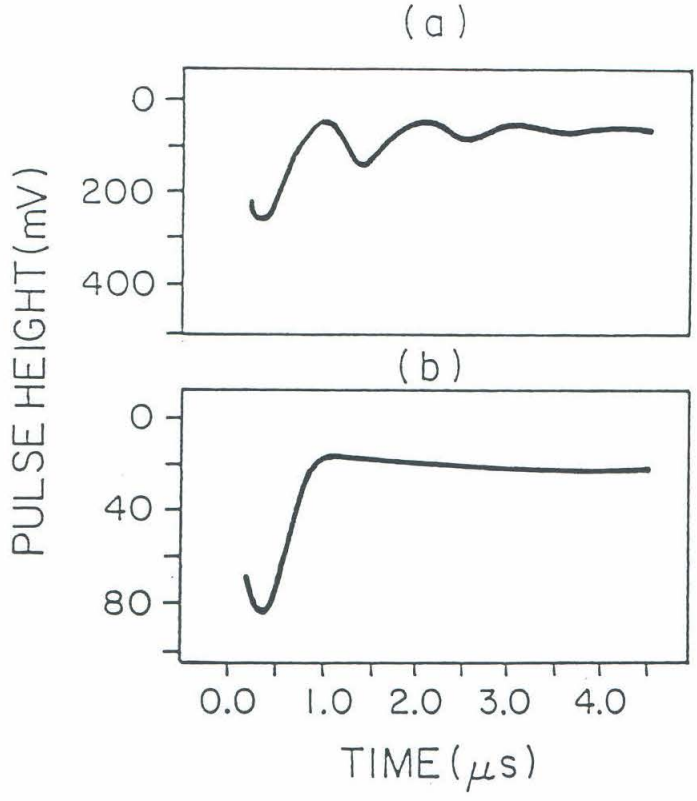

Figure (3.4) (a) Signal from the proportional counter when filled with pure xenon. (b) The same signal when 1 % of CH_4 was added.

produced when the UV photons from the secondary scintillation strike the walls are shown in Figure (3.4a). The separation time of the pulses represents the time for the electrons to drift from the wall to the anode wire. Figure (3.4b) shows the same pulses when the scintillation was quenched by adding 1% CH_4. It can be seen that the secondary pulses associated with the scintillation have now completely dissappeared.

The same proportional counter was used to study the proportional properties of different gas mixtures. With pure xenon in the counter, an energy resolution of about 10% for an ^{55}Fe x-ray (5.9 keV) source was achieved. However, the range of working voltage was very small (50 V out of 1400 V for the geometry used), and even within this working range the operation was not very stable against high voltage breakdown. It was found that with a 5% admixture of CH_4, xenon became stable against breakdown, the diffusion problem was solved, and the drift velocity was increased. Since the scintillation light was now completely quenched, the problem of photoelectron emission was also eliminated. It was decided to use this Xe-CH_4 mixture since it allows good imaging and energy resolution, which are the main goals of the TPC even though the tradeoff was the loss of a time-zero scintillation trigger.

3.5.2 Track Reconstruction

The prototype TPC was used for imaging the tracks of various charged particles. The electronics were developed using a standard drift gas p-10 (90%Ar + 10% CH_4) at 1 atm. Two plastic scintillators, which sandwiched the TPC, generated a time-zero trigger for the cosmic ray muon tracks. Once it was established that the electronics functioned satisfactorily, the p-10 gas was replaced with a Xe-CH_4 mixture. Initially a 1% admixture of CH_4 was used. To keep the system stable against high-voltage breakdown, this admixture was

later increased to 5%. This gas mixture performed quite well, and it was possible to image the tracks of charged particles (cosmic ray muons, alpha particles or electrons). Except in the case of cosmic ray muons where a trigger was available, the image recording process was started by the first available signals from the anode wires. For diagnostic purposes the recording was also triggered by a randomly chosen channel. The part of the track that arrived at the readout plane after the triggering was then reconstructed. A muon track and an electron track are shown in Figure (3.5). At 1 atm of xenon, the 155 keV conversion electron from a ^{139}Ce source produced a track 10 cm long. Because of multiple scattering, this track is normally very erratic. To demonstrate the resolution of the system, a relatively straight track was selected. The first two columns in the Figure show the projections of the tracks in the xz and yz planes as a function of time. Here x, y, and z represent the anode wire, pad, and the drift directions, respectively. The drift distance z is obtained from the product of the drift time, which is shown in the figures and the drift velocity.

3.5.3 Energy and dE/dx measurements

In the design of this prototype, no provision was made for an energy measurement. However, to get an idea of the energy resolution and dE/dx along the track, the signal induced on the Frisch grid was studied. This grid picked up the signals from all the anode wires in the correct time order. Some information on the total energy and in some cases on the dE/dx was obtained by using the following set up. The grid was connected to a preamplifier, which kept it at a virtual ground, and so the drift field inside the TPC remained unchanged. During an event the grid signal was digitized using a transient recorder (LeCroy TR 8837F). Some examples of the digitizer output are shown in the third column of Figure (3.5). Here the time development of the charge

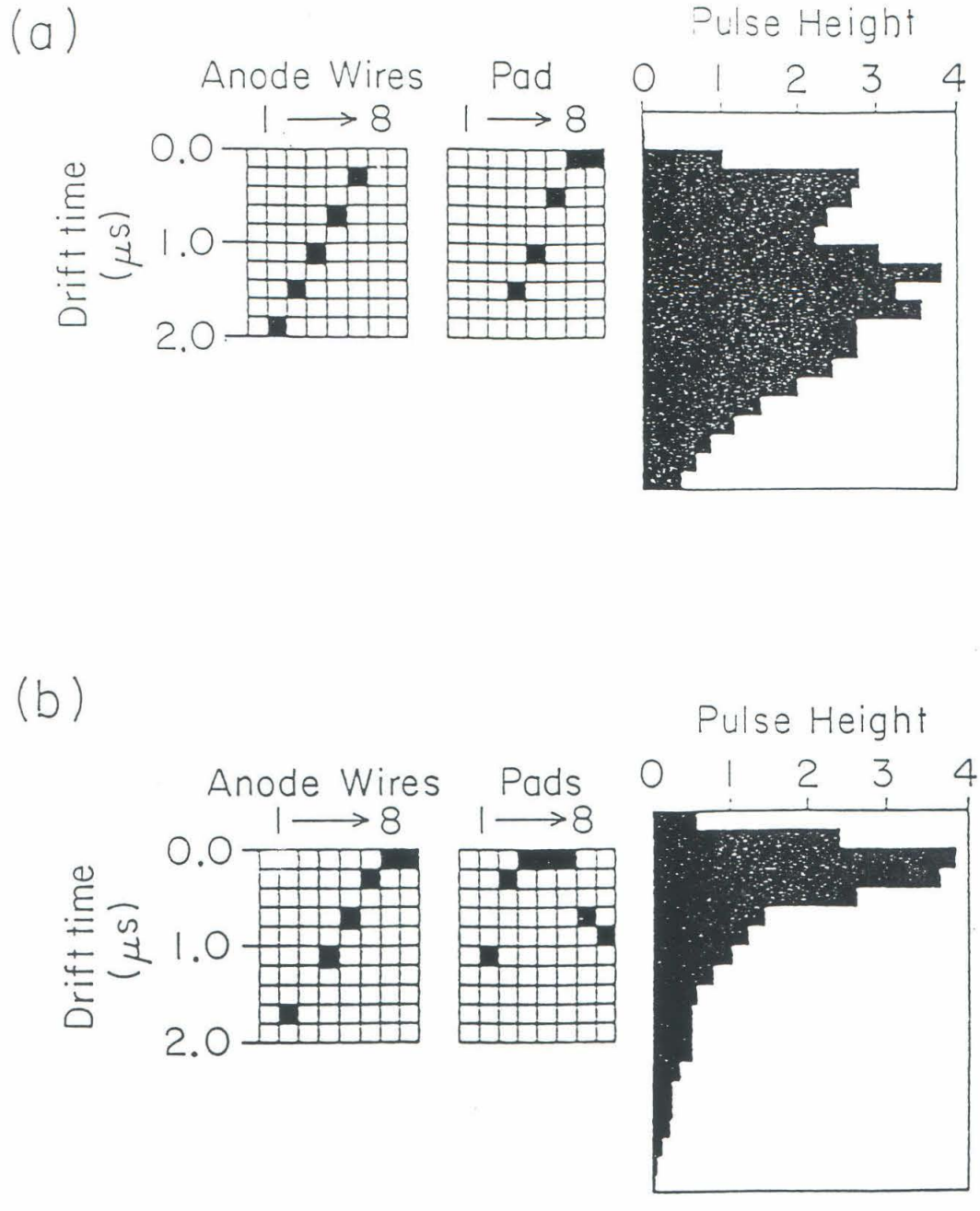

Figure (3.5) (a) A cosmic ray muon track. (b) A 155 keV electron track.

collection in the anode wires is shown. In a straight track, such as a muon track, the time development corresponds directly to dE/dx. In the zigzag track of electrons that undergo multiple scatterings, this is no longer true since charges from different parts of the track may be collected at the same instant inducing a large, unresolved pulse. However, the integrated signal in all the cases will correspond to the total energy. An energy spectrum based on 10000 events for 155 keV electrons from a ^{139}Ce source is shown in Figure (3.6). The peak is resolved but the energy resolution is poor. This is not surprising since the grid had a large capacitance and, consequently, was very noisy. Also, since only two field shaping rings were used, the electric drift field was not very uniform around the edges. Because of the small size of the TPC, not all the events were fully contained in the drift volume. This fact along with the coarseness of the spatial resolution prevented the detection of the charge blobs produced at the end of an electron track. However, on comparing the charge deposition per unit length in the minimum ionizing region (2.5 MeV per cm) to the deposition of a low-energy electron (155 keV), it was determined that the average charge deposition per unit length for the low energy electrons was roughly a factor of 4 higher.

3.6 Conclusion

Most of the necessary information required for the design of the final TPC was provided by this prototype. In particular, it was found that imaging with good resolution is difficult to achieve while observing the scintillation light. It was also found that xenon with a 5% or more admixture of CH_4 had the required drifting properties and stability against high-voltage breakdown and so made a suitable fill gas for the TPC. Tracks of various charged particles

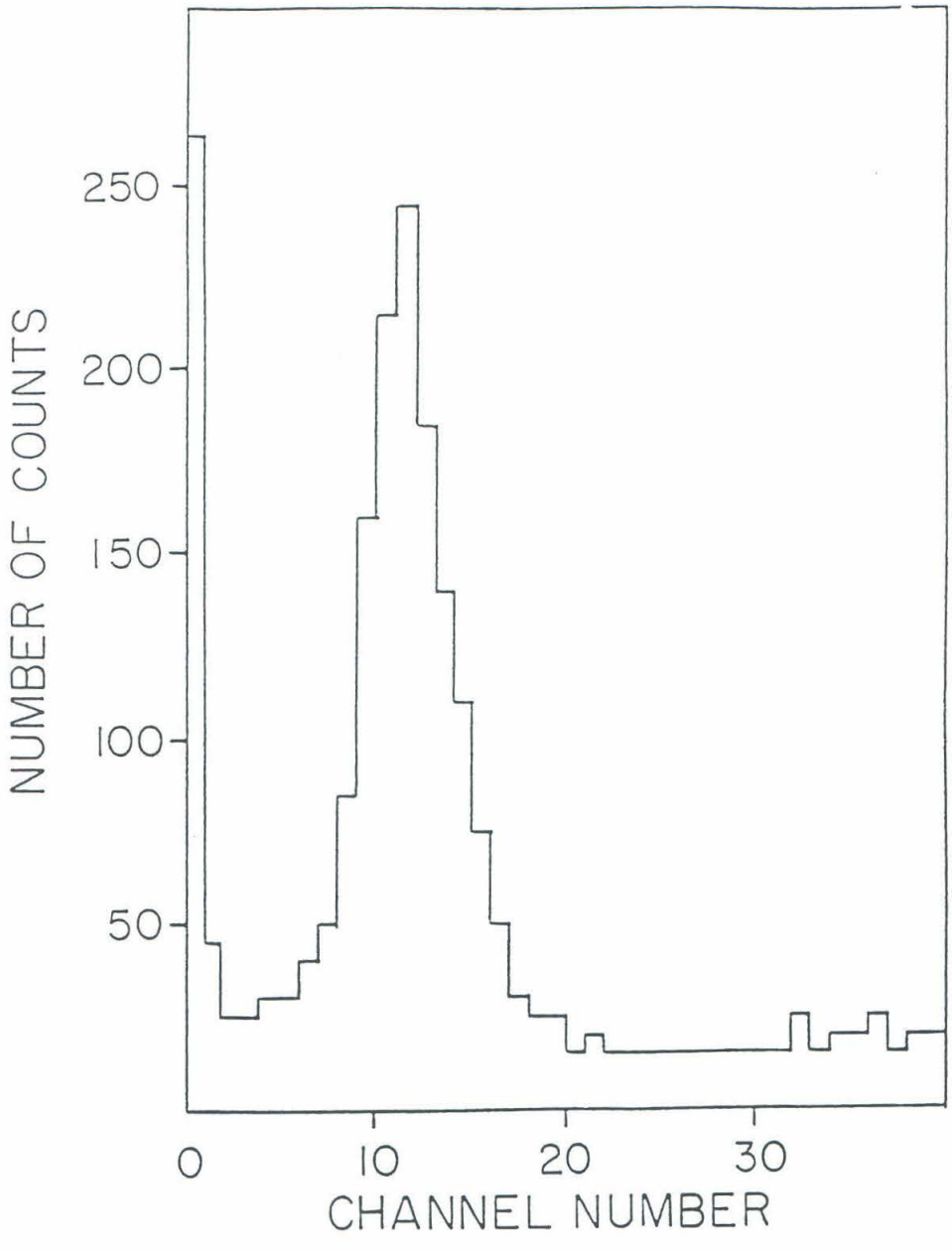

Figure (3.6) Energy spectrum from a 155 keV electron source.

like alpha particles, cosmic ray muons, and electrons were reconstructed using the available electronics. Although the system was not designed for energy and dE/dx measurements, some qualitative information was obtained from the induced signals collected on the grid.

To generate realistic tracks and to further investigate the charge blobs, the Monte Carlo code discussed in the next chapter was developed.

CHAPTER FOUR

Monte Carlo Simulation

4.1 Introduction

The design of the TPC depended on a precise knowledge of electron trajectories in xenon gas. To simulate electron trajectories in a gas at high pressure, a Monte Carlo code was developed. This chapter presents a discussion of the theory of multiple scattering, the details of the code and the results obtained that are relevant for the design of the high-pressure xenon TPC. The calculation is quite general and can be extended to a large range of gas pressures and electron energies. Information on the following items was obtained from the Monte Carlo simulation:

(1) The maximum extent of the trajectory of the electron emitted in the decay as a function of gas pressure. These data determined how the efficiency (the percentage of the total number of decays that are fully contained in the chamber) of the TPC depended on its volume.

(2) The detailed structure of the electron trajectory used to determine the spatial resolution required to reconstruct the trajectory accurately.

(3) Charge deposition per unit volume. Multiple scattering complicates the recognition of the vertex of the two trajectories of the electrons emitted in a double beta decay. The increased dE/dx for the low energy electrons at the end of a trajectory results in a large rise in the number of electron ion pairs produced. This rise leads to a charge blob at the end of a trajectory. A double beta decay event will be a trajectory with charge blobs at each end. Recognition of such a charge blob will depend on the spatial resolution.

(4) The number of times (if any) that the trajectory crossed itself. At a crossing point there may be a higher level of charge concentration that could be mistaken for a charge blob. For a given spatial resolution, the probability of finding several charge blobs in the same trajectory was calculated. This gave an indication of how effective the double blob idea is at background rejection.

(5) A realistic electron trajectory with charge density along the path, for the development of software capable of reconstructing a trajectory.

4.2 Theory of multiple scattering

A theory of multiple scattering of electrons on atoms was first developed by Goudsmit and Saunderson in 1940 [51]. Its application to a specific scattering problem required the knowledge of single scattering by an isolated atom. In 1948 Molière [52] presented a theory of multiple scattering for fast-charged particles scattered by a screened Coulomb field. This theory made use of a small angle approximation and was based on a nonrelativistic cross section. In 1953 Bethe [53] showed that Molière's theory could be made exact and relativistic by multiplying Molière's results (at large angles where the angular distribution is essentially single scattering) by the ratio of the exact single-scattering cross section to the cross section which Molière used. To simulate an electron trajectory in high-pressure xenon gas, the expressions derived in Bethe's paper were used.

The number of electrons in the angular interval $d\theta$ after traversing a thickness t in a material of atomic number Z is given by

$$f(\theta)\theta d\theta = \frac{\theta d\theta}{\chi_c^2}\int_0^\infty y dy J_o\left(\frac{\theta y}{\chi_c}\right)\exp\left[\frac{1}{4}y^2\left(-b+\ln\frac{y^2}{4}\right)\right], \qquad (4.1)$$

where

$$b = \ln\left(\frac{\chi_c^2}{1.167\chi_a^2}\right).$$

The angle parameter χ_c is defined in such a way that the probability of a single scattering through an angle less than χ_c is identically zero. It is given by

$$\chi_c^2 = \frac{4\pi N t e^4 Z(Z+1)}{(pv)^2}, \tag{4.2}$$

where N is the number of scattering atoms per cm^3, p is the momentum, and v is the velocity of the scattered electron. χ_a is the characteristic screening angle and according to Molière's approximation it is given by

$$\chi_a = \chi_o\sqrt{1.13+3.76\,\alpha'^2}. \tag{4.3}$$

χ_o is the angle below which deviations from the Rutherford scattering law $(1/\theta^4)$ that are due to nuclear effects begin to appear and is given by

$$\chi_o = \lambda/(0.885 a_o Z^{-1/3}), \tag{4.4}$$

where λ is the deBroglie wavelength of the electron, a_o is the Bohr radius and $\alpha' = \alpha Z/\beta$, α being the fine structure constant and $\beta = v/c$.

Molière evaluated Equation (4.1) for all angles, by defining a new parameter B and a new variable x such that

$$B - \ln B = b \tag{4.5}$$

$$x = \theta/(\chi_c\sqrt{B}). \tag{4.6}$$

Then the distribution function f(x) was expanded in a power series in 1/B,

$$f(x)xdx = xdx[f^{(0)}(x) + B^{-1}f^{(1)}(x) + B^{-2}f^{(2)}(x).....], \tag{4.7}$$

where

$$f^n(x) = \frac{1}{n!}\int_0^\infty u du J_o(xu)\exp(-\frac{u^2}{4})\left\{\frac{u^2}{4}\ln(\frac{u^2}{4})\right\}^n. \tag{4.8}$$

For the first three functions $f^n(x)$, Molière gave the following asymptotic

formulae:

$$f^{(0)}(x) = 2e^{-x},$$

$$f^{(1)}(x) = \frac{2(1-5x^{-2})^{-4/5}}{x^4},$$

$$f^{(2)}(x) = \frac{16}{x^6}\frac{(\ln x + \ln 0.4)}{(1-9x^{-2}-24x^{-4})}.$$

In the Monte Carlo simulation, the above expressions were used for values of x greater than 4. For x less than 4, Table 4.1 from Bethe's paper (see Table 1) was used to determine $f^{(1)}(x)$ and $f^{(2)}(x)$.

In the derivation of Equation (4.1), the approximation used was $\chi_0 << \chi_c$, which is generally true ($\chi_c/\chi_a \approx 100$) for foils of moderate thickness. The ratio $(\chi_c/\chi_a)^2$ is a measure of Ω_0, the mean number of scatterings that occur in a thickness t of the material. Hence, for low-pressure gas in a finite volume, Molière's theory of small-angle multiple scattering is no longer valid. In fact, Molière considered his method to be good for $B > 4.5$ and $\Omega_0 > 20$. In this calculation (details to be discussed later), it was found that for a 1 MeV electron travelling 4 mm in xenon gas at 5 atm $\Omega_0 \approx 100$ and $B \approx 6$.

4.3 Range of electrons

4.3.1 Average Energy Loss

The Bethe-Bloch formula [54] for the average energy loss by collisions was derived for electrons under the assumption that above a certain fractional energy transfer, the atomic electrons can be regarded as free, so that Moller's cross section [55] for the scattering of free electrons at rest in the Born approximation is valid. Using Bethe's theory, Rohrlich and Carlson [56] derived a formula to calculate the energy loss by collision. This formula takes into account

(x)	1000 $f^{(1)}(x)$	1000 $f^{(2)}(x)$
0.0	845.6	2492.9
0.2	703.8	2069.4
0.4	343.7	1048.8
0.6	-77.7	-4.4
0.8	-398.1	-606.8
1.0	-528.5	-635.9
1.2	-477.	-308.6
1.4	-318.3	52.5
1.6	-139.6	242.3
1.8	-0.6	238.6
2.0	78.2	131.6
2.2	105.4	19.6
2.4	100.8	-46.7
2.6	82.62	-64.9
2.8	62.47	-54.6
3.0	45.5	-35.68
3.2	32.88	-19.23
3.4	24.02	-8.47
3.6	17.91	-2.64
3.8	13.66	0.05
4.0	10.638	1.0741
4.5	6.140	1.2294
5.0	3.831	0.8326
5.5	2.527	0.5368
6.0	1.739	0.3495
7.0	0.9080	0.1584
8.0	0.5211	0.0783
9.0	0.3208	0.0417
10.0	0.2084	0.0237

Table (4.1) Numerical values of the functions $f^{(1)}(x)$ and $f^{(2)}(x)$ as determined by Bethe [53].

hard collisions and collisions involving low-energy transfer. The formula is given by:

$$\left(\frac{dE}{dX}\right)_{coll} = 4\pi r_0^2 \frac{mc^2}{\beta^2} NZ \left[A + B\right], \tag{4.9}$$

with

$$A = \ln\left(\frac{\beta\gamma\sqrt{\gamma-1}mc^2}{I}\right)$$

and

$$B = \frac{1}{2\gamma^2}\left(\frac{(\gamma-1)^2}{8} + 1 - (2\gamma^2 + 2\gamma - 1)\ln 2\right) - \delta,$$

where

$\left(\frac{dE}{dX}\right)_{coll}$ = energy loss by ionization in MeV/cm

r_o = classical electron radius in cm

$\gamma = (1-\beta^2)^{-1/2}$

N = number of atoms per unit volume

Z = the atomic number

δ is a corrective factor that is due to the polarization and dielectric properties of the medium

I is the mean excitation potential of the material in eV. For $Z \geq 13$ an approximation for I is given by the emperical formuala of Sternheimer [57]:

$$I = 9.76Z + 58.8Z^{-0.19}\ eV.$$

Theoretical and emperical formulae exist for the δ term [57]. The

importance of the density effect is shown in [58].

4.3.2 Energy loss by Bremsstrahlung emission.

The energy lost by bremsstrahlung emission can be written as:

$$\left(\frac{dE}{dX}\right)_b = N\frac{E}{mc_2}\Phi(E)\,,$$

where

$$\Phi(E) = \frac{1}{E}\int_0^T E_\gamma d\sigma(E_\gamma)$$

and $d\sigma(E_\gamma)$ is the probality of creation of a photon of energy E_γ from an electron of energy E. The function Φ_f varies with E and E_γ and can be represented in an approximate way by different analytical formulae according to the energy region considered and the approximation valid in this region.

4.3.3. Computation of $(dE/dX)_{total}$

Pages et al [58] calculated the energy lost by electrons in collisions and through bremsstrahlung emission for several elements and compounds. They used the Bethe formula, Sternheimer's theoretical density-effect correction and the Koch-Mortz bremsstrahlung cross section. They tabulated the energy losses in 55 energy steps over the range 10 keV to 100 MeV [58]. For primary electrons with an energy less than 10 keV, the energy losses by emission of bremsstrahlung radiation cannot be calculated, but at these energies the radiative energy loss is negligible in comparison to the energy loss that is due to collisions. In the Monte Carlo calculation, the tabulated values of Pages et al [58] were used to determine the total energy loss per cm. A detailed account of the method used is presented in [59].

4.4 Generation of f(θ)

The most important part in the Monte Carlo simulation of an electron track is the generation of f(θ). Although f(θ) can be approximated as simple functions such as $2e^{-x^2}$ for small x and $1/x^3$ for large x, it is not a simple function for the total range of interest. Therefore, rejection techniques were used to generate f(θ) and the procedure was as follows.

The simplest approach of generating f(x) and accepting x if f(x)/f(0) < y (both x and y are random numbers between 0 and 1) is not very efficient since f(x) is a very sharply falling function. To generate f(x) efficiently, x is generated in a similar distribution g(x), which is always greater than f(x)/f(0) for the values of x in the region of interest. The random number x is accepted if f(x)/f(0) < y g(x), where y is a second random number between 0 and 1. There is a tradeoff in choosing the trial function g(x), since the increase in efficiency is associated with a smaller range of x. An obvious choice for the trial function g(x) is e^{-ax^2}, and Figure (4.1) shows the efficiency of generation of f(x) for different choices of a.

The generation of f(x) was compared with several experimental results. In Figure (4.2a) the angular distribution of 15.7 MeV electrons scattered from a gold foil of thickness 18.66 mg/cm ^{2} [60] is shown along with the Monte Carlo histogram. Figure (4.2b) shows the same comparison obtained by the EGS2 and EGS3 Monte Carlo programs [61]. Figures (4.3) and (4.4) show how the results of this Monte Carlo compare with the experimental results of Kulchitsky and Latyshev [62] for electron scattering at the lower energy of 2.25 MeV from aluminum and copper foils. Because of a lack of experimental results, the generated angular distribution cannot be compared with scattering in a gaseous medium at the MeV level; however, since for xenon at 5 atm the ratio $\chi_c/\chi_a \approx 10$, the anticipated error is small. The main source of error is in the evaluation of f(x) through not taking enough terms in the expansion of Equation (4.7).

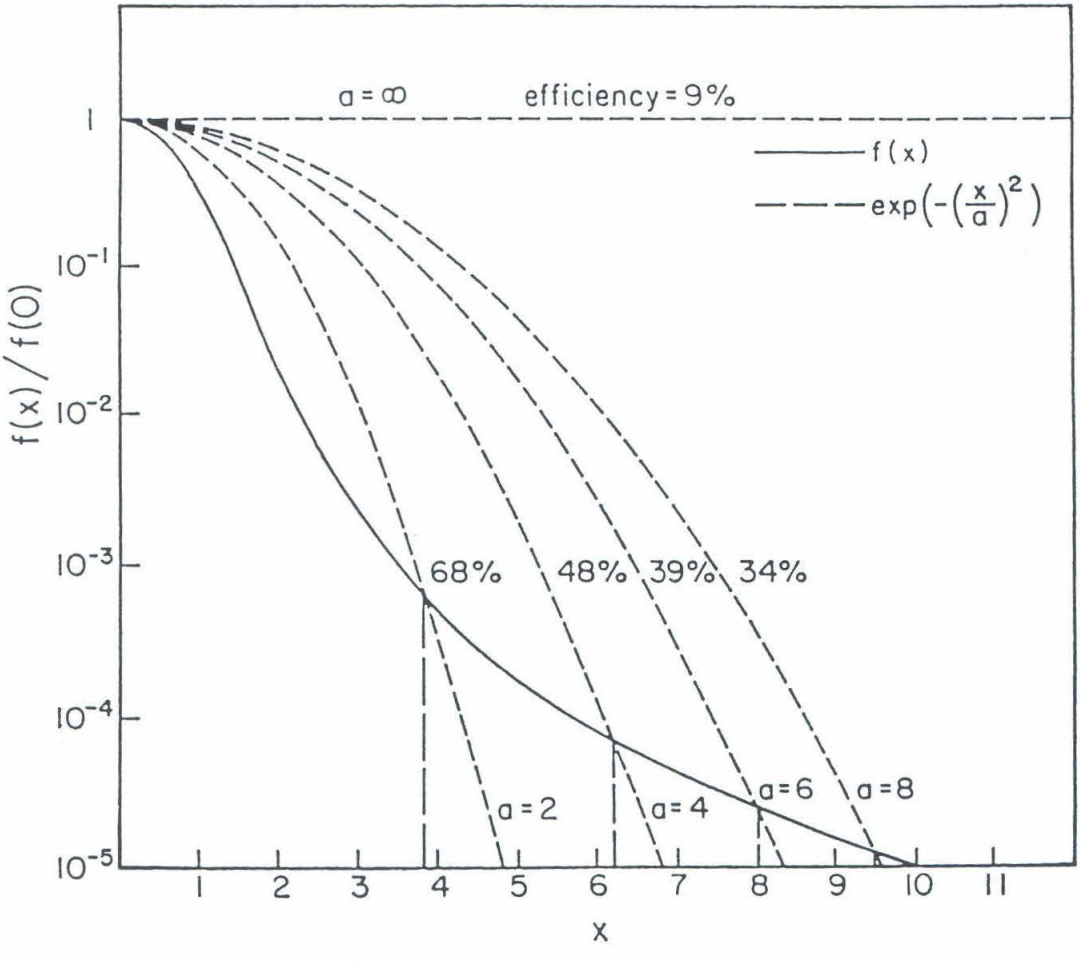

Figure (4.1) Efficiency of generation of f(x) for different choices of the parameter a in the trial function $e^{-(x/a)^2}$. The vertical dashed lines mark the valid region of x for a given trial function.

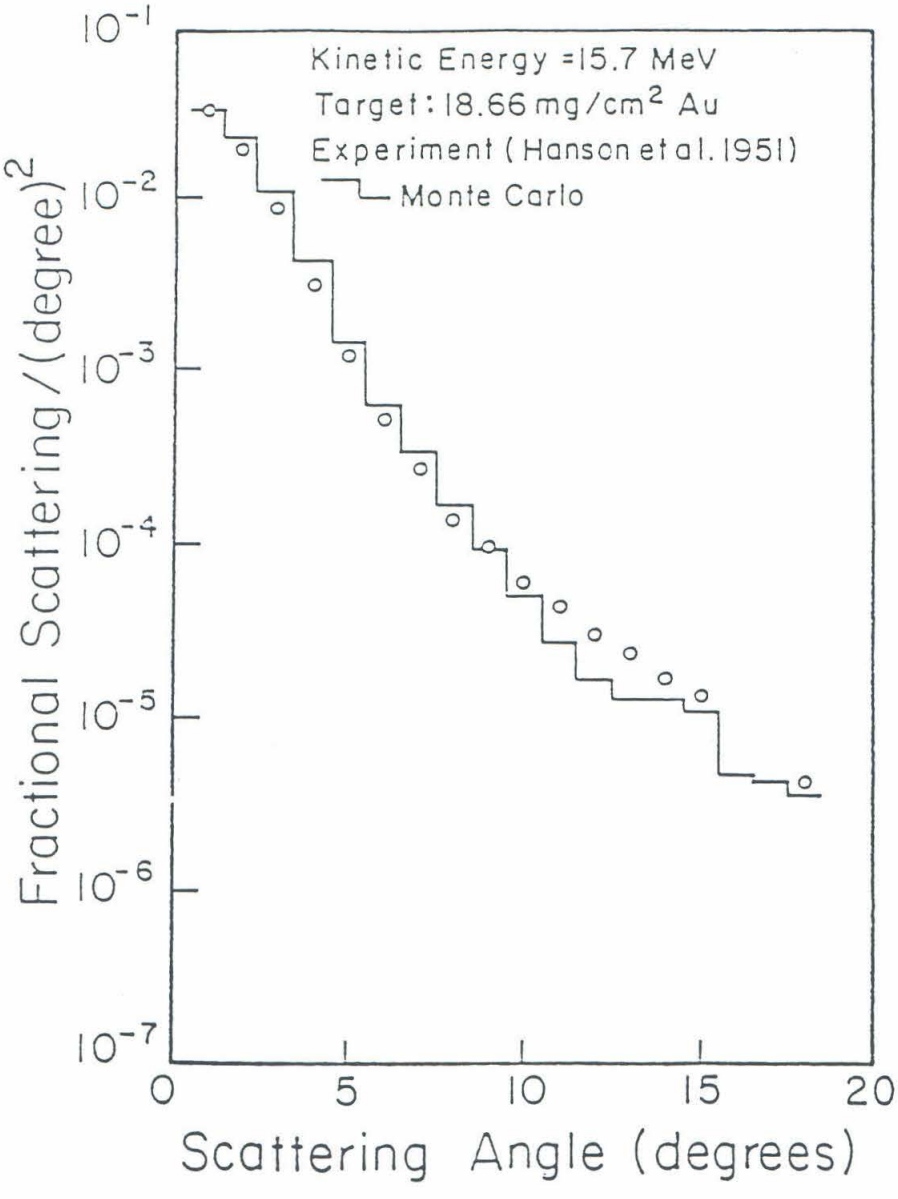

Figure (4.2a) Comparison of the Monte Carlo with the experiment by Hanson et al. (1951).

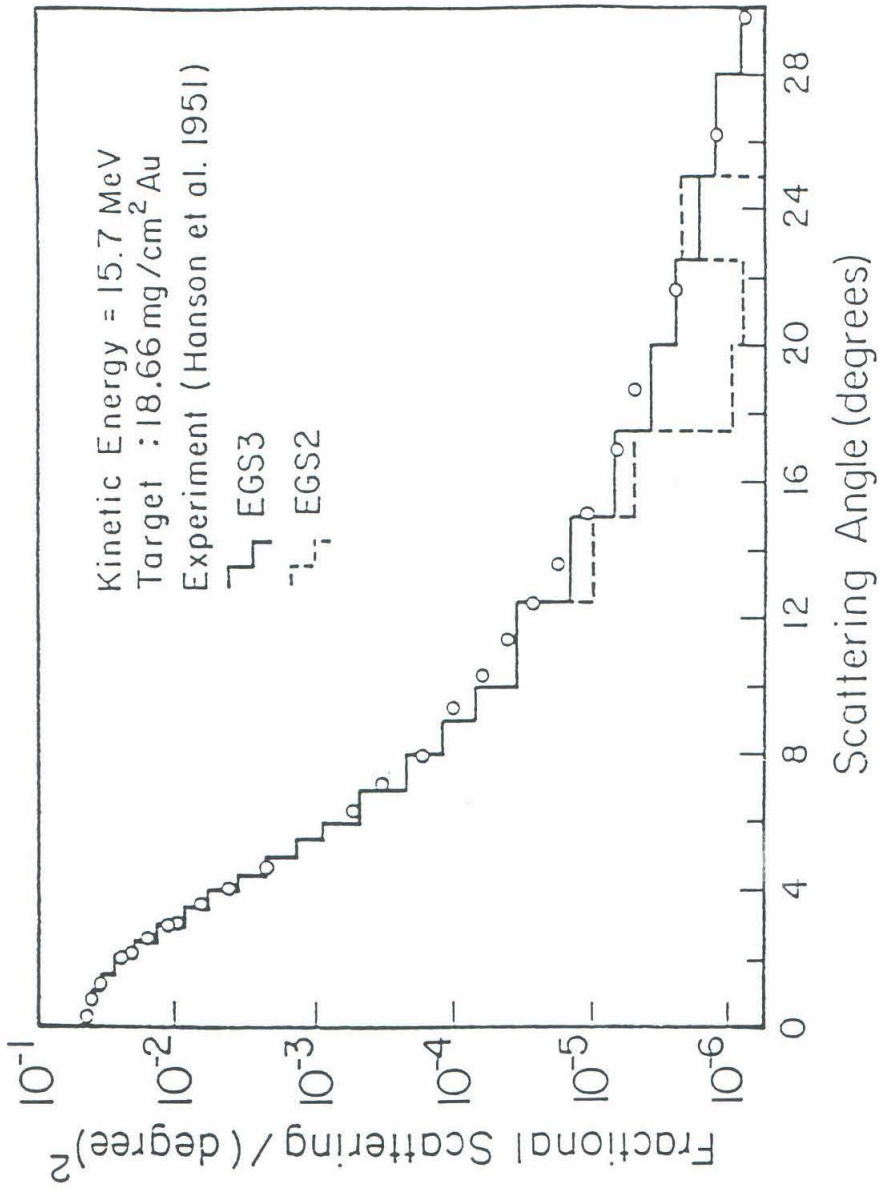

Figure (4.2b) Comparison of the EGS Monte Carlo (Versions 2 and 3) with the experiment by Hanson et al. (1951).

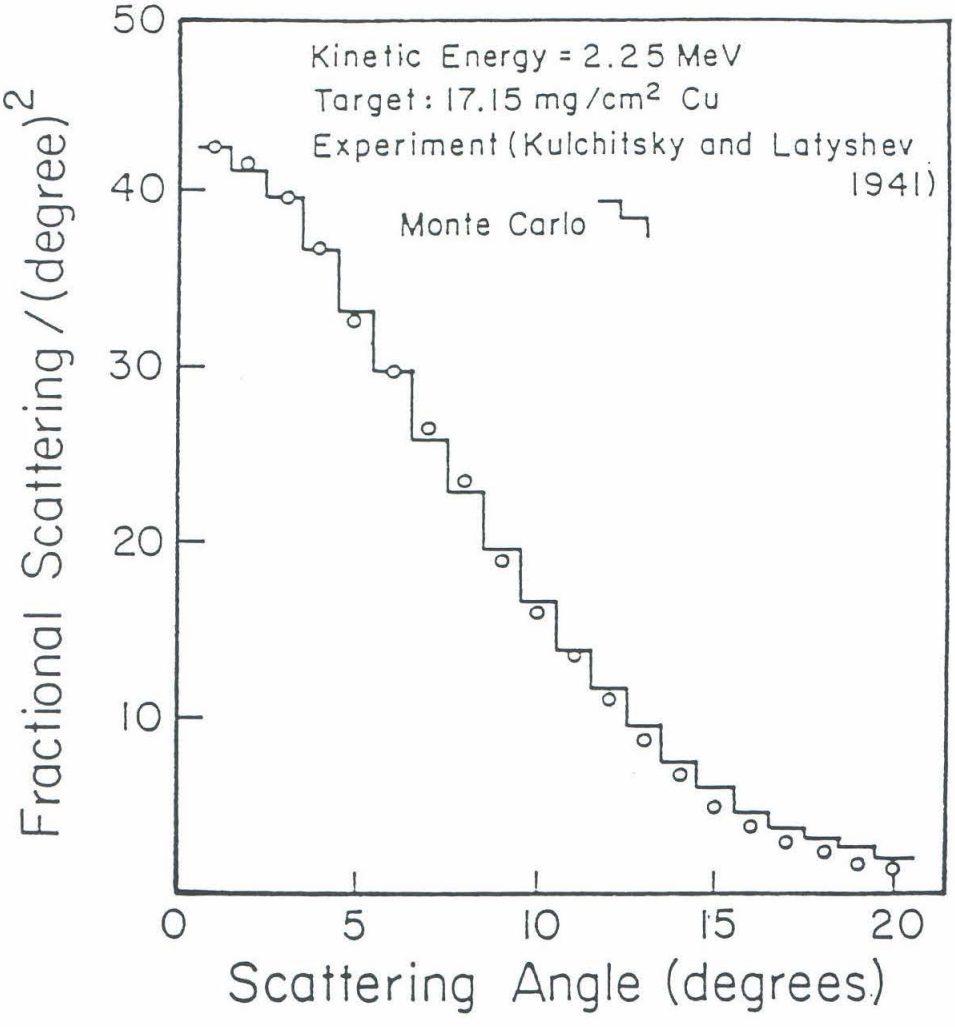

Figure (4.3) Comparison of the Monte Carlo with the experiment by Kulchitsky and Latyshev (1941).

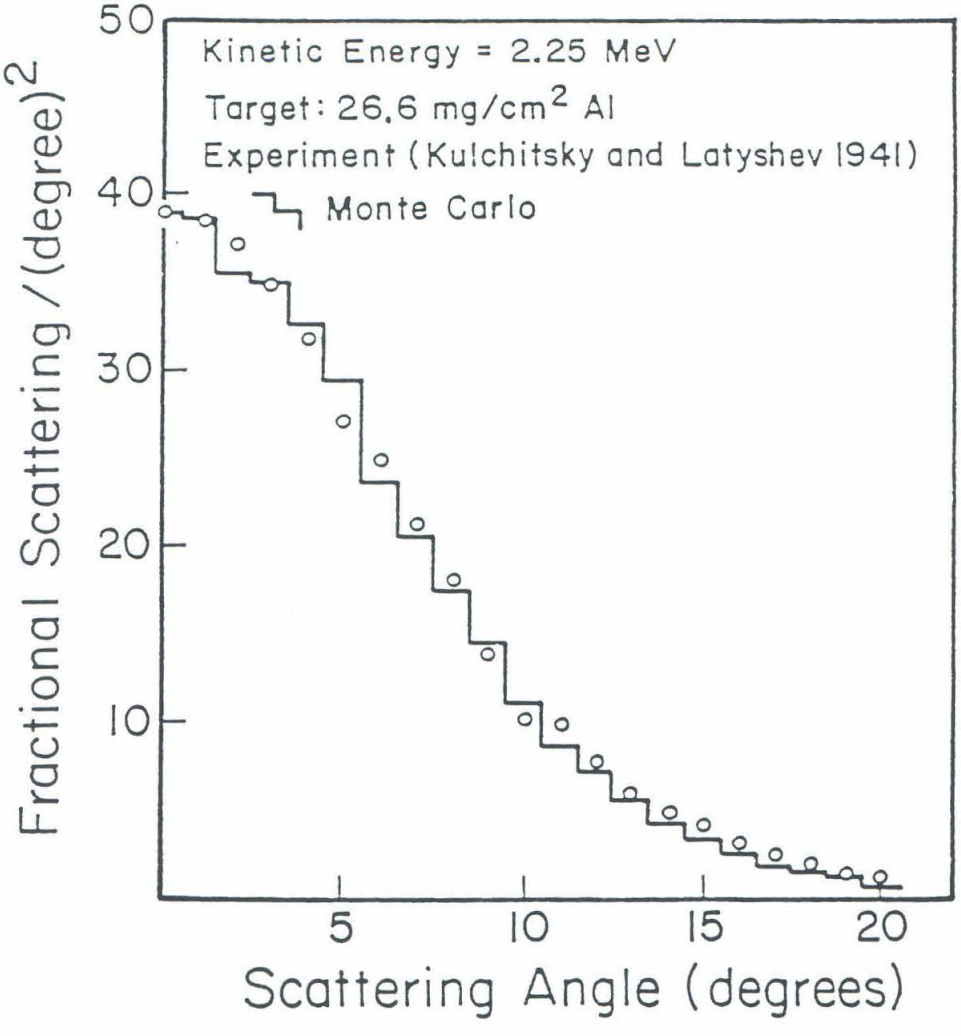

Figure (4.4) Comparison of the Monte Carlo with the experiment by Kulchitsky and Latyshev (1941).

4.5 Monte Carlo Simulation

The Monte Carlo code generated the energy and position of an electron as it moved through a gas in a cylindrical detector of radius r and height h. The starting point was chosen at random inside the detector. Initially the full energy (E_i) of the electron was used and the range R was calculated for a given amount of energy loss (dE), which was small compared to the total energy. Once the length traversed in that energy step was calculated, χ_c and B were evaluated. Then θ was generated according to the function $f(\theta)$ as described in the last section, and the azimuthal angle ϕ was generated randomly from 0 to 2π. Once R, θ and ϕ were known, the location of the electron, after the given energy loss, was found. Then the probability of producing a delta electron with an energy E_δ greater than dE was calculated. A discussion of delta electrons is given in Section 4.7. Starting from this position the next segment was calculated using the new energy (E_i - dE - E_δ), and the process was continued until the energy of the electron was reduced to zero or until χ_c/χ_a reached a given error limit below which the derivation broke down. At the end of each track segment, the electron coordinate frame (in which θ and ϕ were determined) was rotated back to the fixed laboratory coordinate system, and the transformed angles Θ and Φ were then used to calculate the x, y, z coordinates of the electron. The transformation is given by the following equations:

$$\cos\Theta = -\cos\phi \sin\theta \sin\theta_0 + \cos\theta \cos\theta_0 ;$$

$$\cos\Phi = \frac{1}{\sin\Theta} [\cos\phi_0 \cos\theta_0 \cos\phi \sin\theta - \sin\phi_0 \sin\theta \sin\phi + \sin\theta_0 \cos\theta \cos\phi_0] ;$$

θ, ϕ, θ_0 and ϕ_0 are the angles for the current and previous segments, respectively.

In the TPC the trajectory is reconstructed from the charge deposited by the primary electron as it passes through the chamber. The track width is limited by the spatial resolution of the xy readout and the accuracy of the drift

time and the drift speed. The charge deposited in a small volume element (with a size corresponding to the spatial resolution of the TPC) was calculated in the following way. A three-dimensional grid (sized according to the spatial resolution of the TPC) was overlaid on the track. Moving along the track, a bin coordinate was assigned to each segment; then the energy deposited in the track segment was divided by the segment length and dE/dx was evaluated along the trajectory. The values of dE/dx from the current and the previous segments were averaged. This average value of dE/dx was then used to calculate the energy deposited in a given bin. The total number of electrons produced in a bin was determined by dividing the energy deposited in the bin by the mean ionization potential (22.2 eV) for a xenon atom [63]. The foregoing procedure was repeated for each step of the track. Finally, the total number of electrons at crossing points in the track was counted. The program flowchart is shown in Figure (4.5).

4.6 Results

The Monte Carlo simulation was used to simulate electron trajectories at various energies and at various pressures. Typical electron trajectories at 1.25 MeV in three different pressures (5, 10, 15 atm) are shown in Figure (4.6). It can be seen that at high energies the scattering involves small-angle deflections, whereas at the end of the trajectory, the larger angle scatterings become more frequent and the path starts to curve around. The stretched length of the trajectory goes down with increased pressure as expected. However the required volume of a TPC is not determined by the stretched length. Because of the multiple scatterings, a significant number of trajectories are enclosed in a much smaller volume.

To estimate an optimum volume for the TPC the Monte Carlo code was used to look at how the efficiency of the detector varied with detector size and

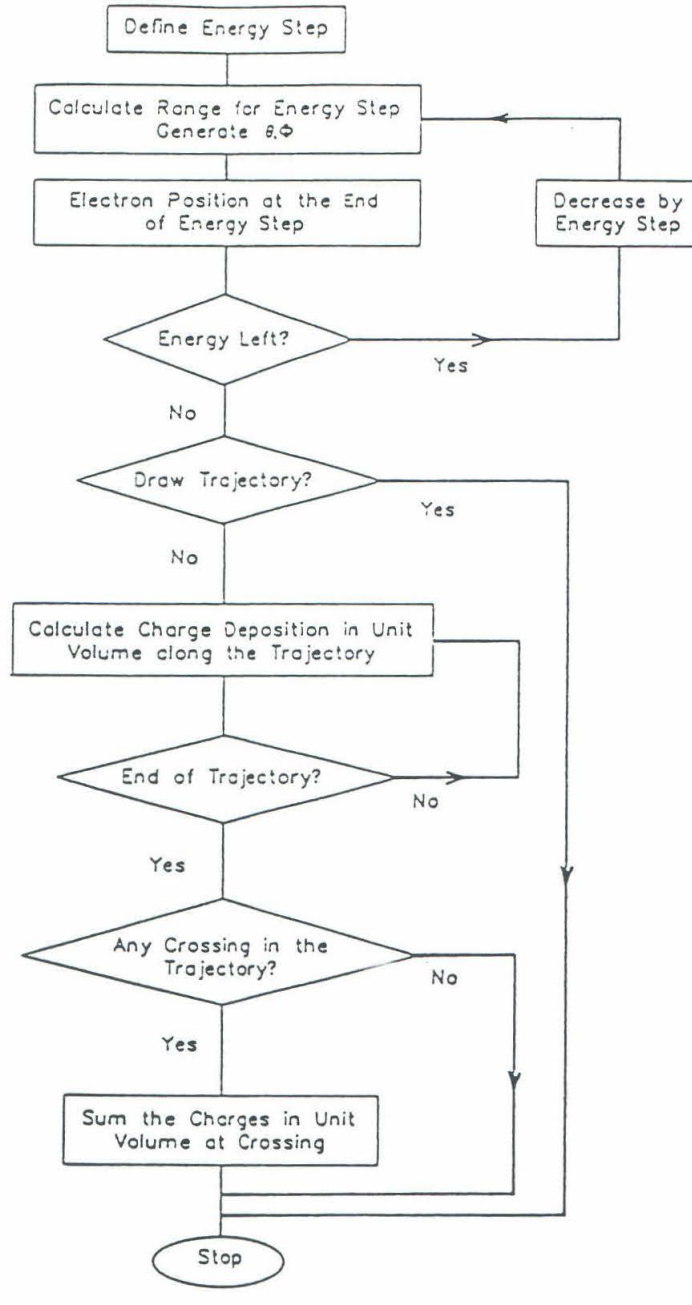

Figure (4.5) Flow chart of the Monte Carlo program for the simulation of electron trajectories.

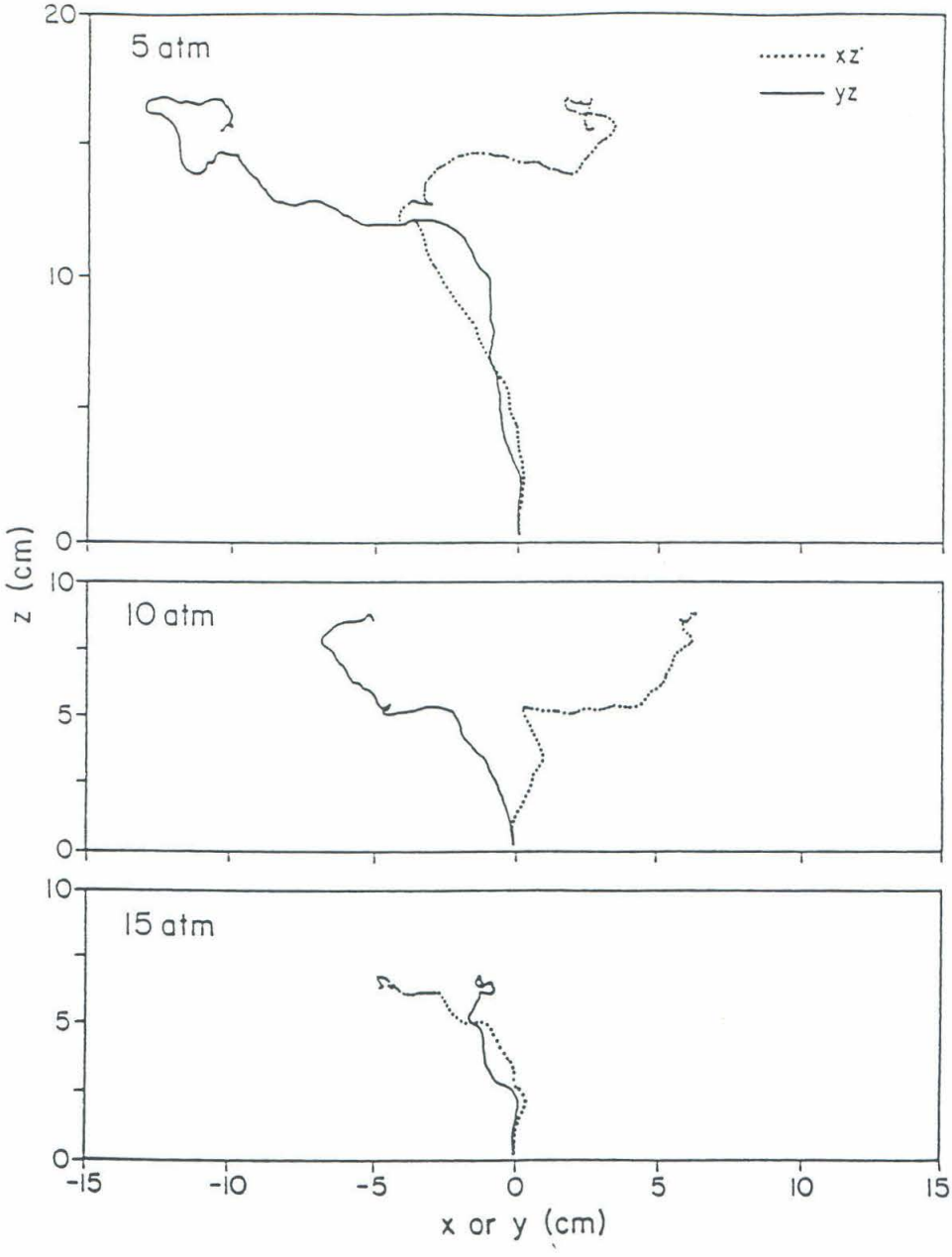

Figure (4.6) The trajectory of a 1.25 MeV electron in 5, 10 and 15 atm of xenon, ejected along the z axis from the origin, as simulated by the Monte Carlo calculation. Projections on the xz and yz planes are shown.

gas pressure. The efficiency is defined as the fraction of the total number of trajectories formed by electrons emitted in a xenon double beta decay, which are fully contained in the detector. The energy distribution for a single electron in neutrinoless double beta decay was used, and the function $(1 - \overline{\beta_1}\overline{\beta_2})$ was used for the angular distribution. Figure (4.7) shows how the efficiency depends on the radius R, of a cyclindrical chamber (height 2R), for gas pressures in the range 5 atm to 20 atm.

The background rejection in the TPC depends on the dE/dx measurement in a trajectory. As an electron slows down at the end of a trajectory (Figure (4.8)), the charge deposition increases and produces a charge blob. Thus a double beta decay event will produce a charge blob at each end of the track in contrast with most background events, which will have only a single blob. To investigate the possibility of blob identification, a three-dimensional grid was imposed on the trajectory, and the number of electrons produced in each cubical box was calculated as described earlier. The maximum charge per unit box is shown in Figure (4.9) along with the average charge deposition. Figure (4.10) shows at what point in the trajectory the maxima in charge deposition, as shown in Figure (4.9), occur. This result shows that for a spatial resolution of 3mm, the maximum charge will be within the last cm. Further, it can be seen that with this spatial resolution, a simple discriminator set at the 0.3 fC level, corresponding to 1800 electrons, will be able to discriminate the charge blob against the charge deposition resulting from minimum ionization with an efficiency of 95%. This calculation motivated the adoption of a readout consisting of a simple on/off trigger for each channel with an additional discriminator for charge blob identification. This scheme is much more economical than pulse-shape digitization and as discussed in Chapter 6, it turns out to be entirely adequate for this experiment.

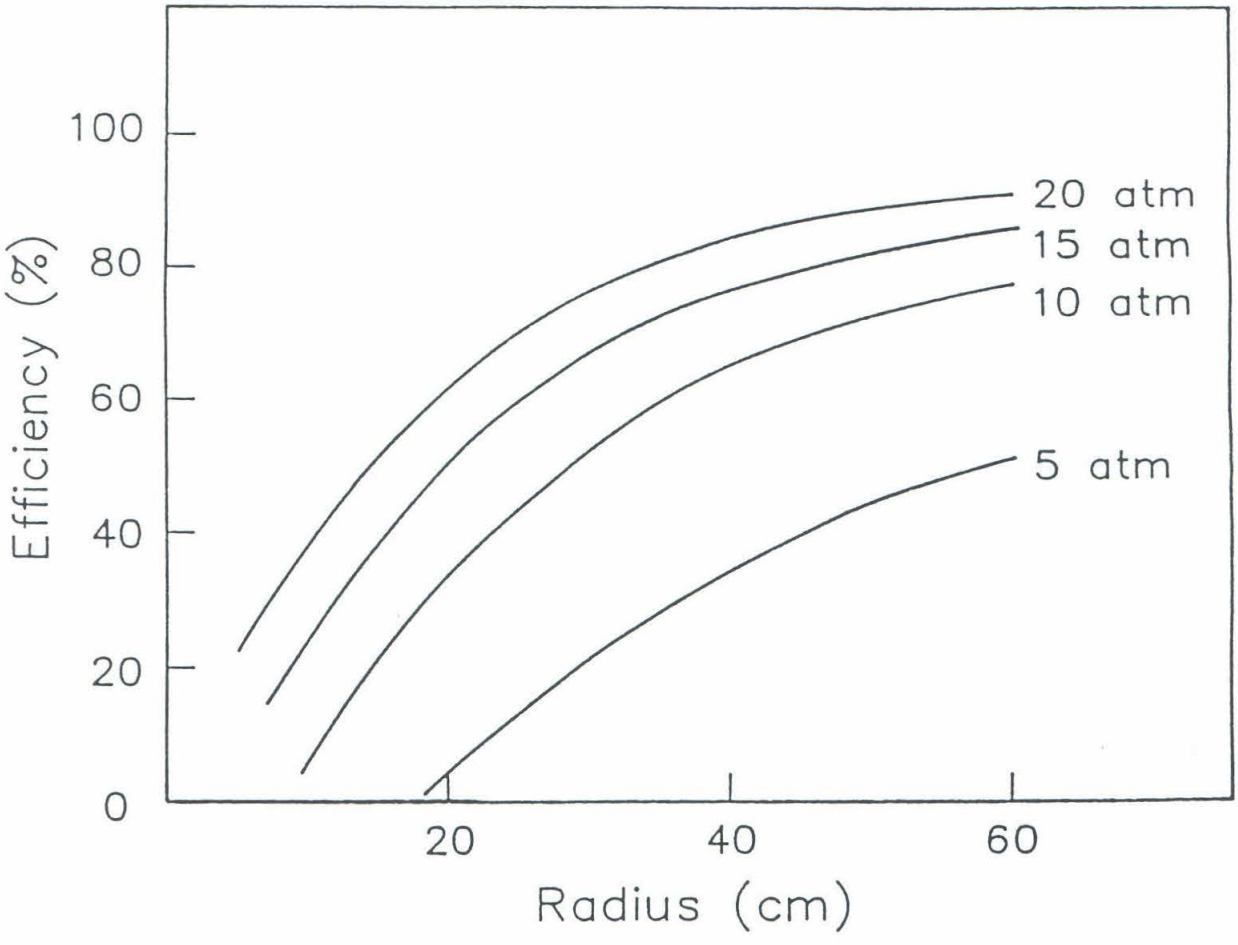

Figure (4.7) Efficiency of the TPC as a function of its size for gas pressures in the range 5 to 20 atm.

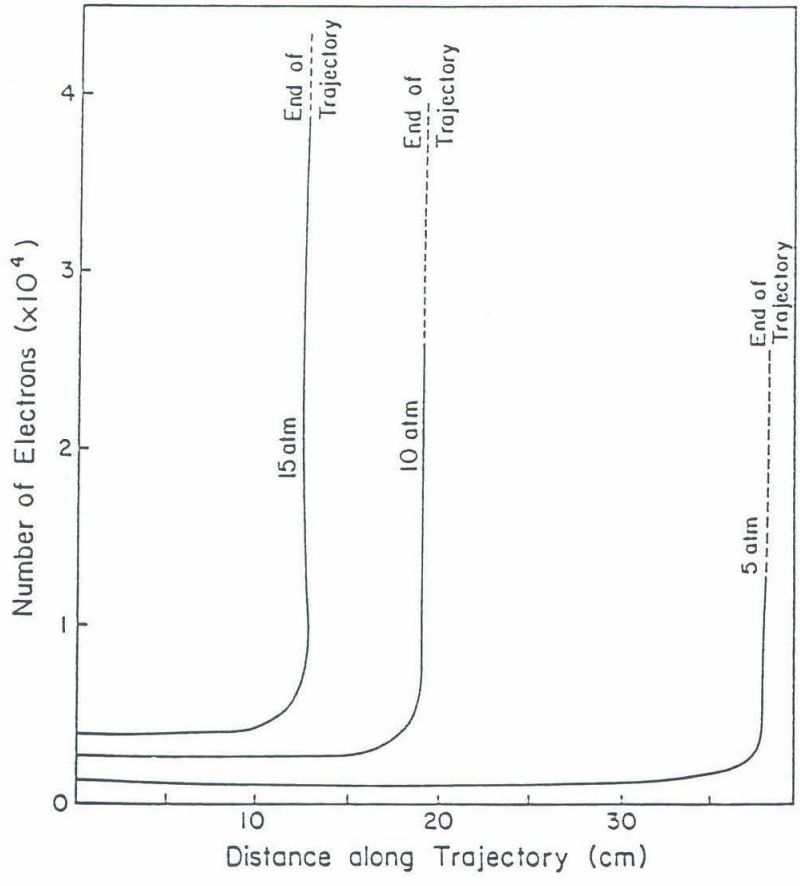

Figure (4.8) Charge deposition along the trajectory of a 1.25 MeV electron in 5, 10 and 15 atm of xenon.

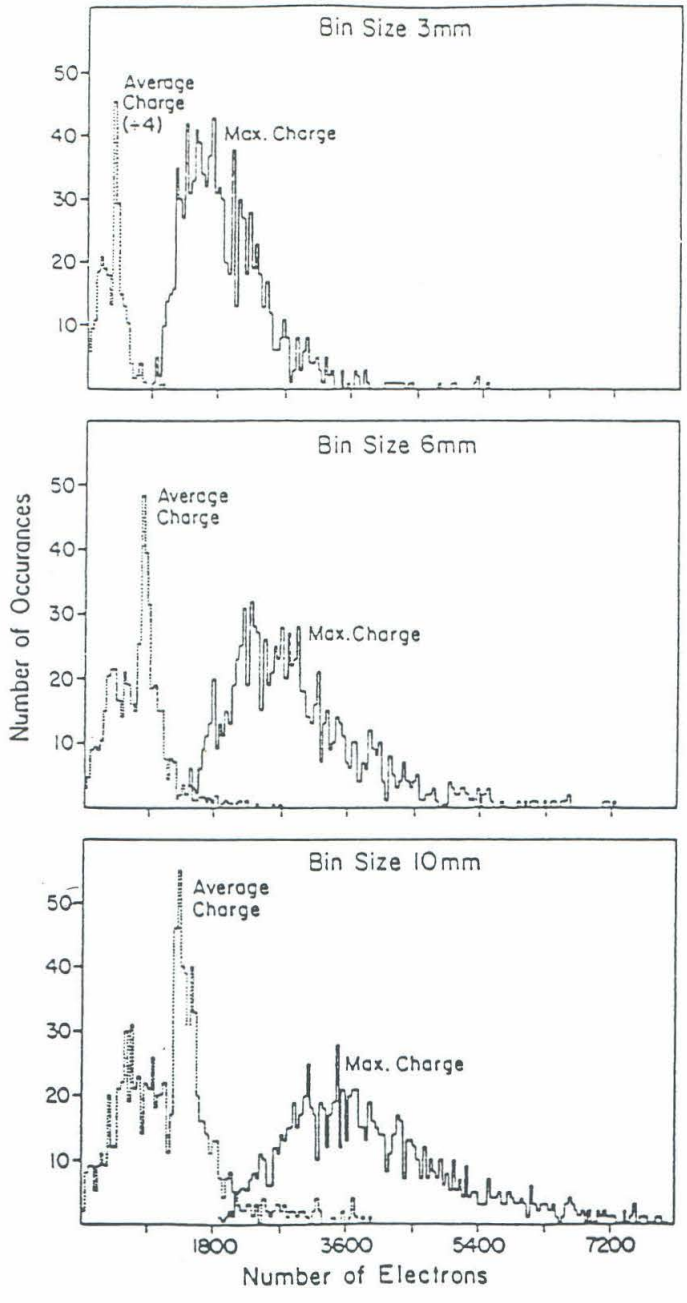

Figure (4.9) Distribution of maximum and average charge per unit bin for bin sizes of 3 mm, 6mm and 10 mm.

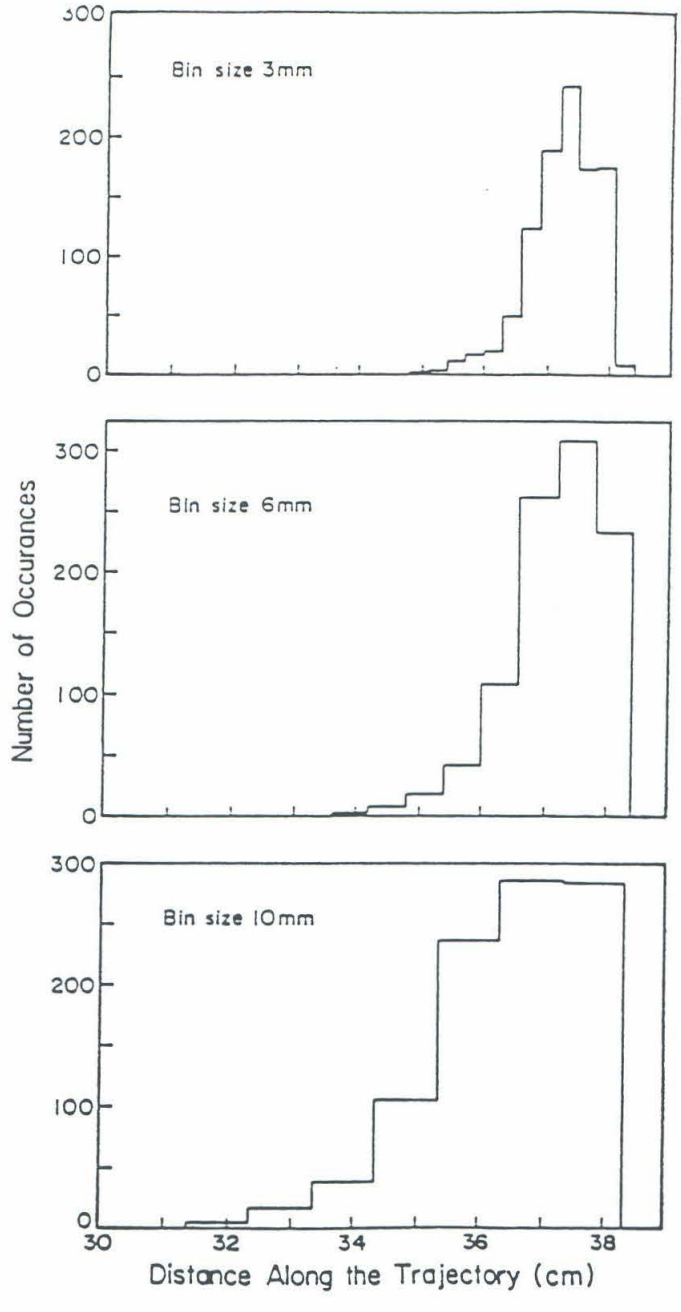

Figure (4.10) The position along the trajectory where the maximum charge deposition occurs for bin sizes of 3 mm, 6mm and 10 mm.

4.7 Delta Electrons

Primary electrons can emit energetic (>30 keV) secondary electrons (δ electrons) at the beginning portion of its trajectory. These delta electrons produce a charge blob. Thus, a single electron (energy 2.48 MeV) with a delta electron at the beginning of the track cannot be discriminated against a $\beta\beta$ decay event by using the "blob at two ends" rejection technique. The original Monte Carlo code was modified to include the effects of delta electrons.

The probability that a primary electron with energy E emits a delta electron of energy E_δ when it travels through a distance x of the gas is given by [64]:

$$P(E_\delta)dE_\delta = \frac{2\pi N_A e^4 Z \rho x}{\beta^2 m_e c^2 A} \times \frac{dE_\delta}{{E_\delta}^2},$$

where

N_A is Avogadro's number

Z is the atomic number of the gas

A is the atomic mass of the gas

β is the velocity of the primary electron as it entered the x^{th} step of its path through the gas.

The above formula is valid in the range $I < E_\delta < E$, where I characterizes the binding of the electrons in the gas. In xenon, I is about 580 eV. A detailed account of the delta electron simulation technique is presented in [59].

When delta electron production was incorporated into the program, it was found that typically in 5 atm of xenon, in a 2.5 MeV electron track, four to five delta electrons were produced. About 6% of the above events had a delta electron produced in the first centimeter of the track.

4.8 Bremsstrahlung Effects

For a 2.5 MeV electron, about 8% (200 keV) of the incident energy is lost by radiation. For a detector resolution of 5%, this radiative energy loss is large enough to modify the energy spectrum. Further, a percentage of those photons created by bremsstrahlung leave the volume of the TPC and decrease the efficiency of the TPC for completely enclosing $\beta\beta$ events.

Bremsstrahlung was incorporated into the Monte Carlo code and the resulting photons monitored as they moved through the TPC. Details of the simulation are presented in [59]. For electrons with an energy of 2.5 MeV in 5 atm of xenon, it was found that the percentage of bremsstrahlung photons that are completely contained in the TPC was 68%. For a double beta decay event, the above percentage was found to be 76%. In Section 4.6 it was found that in 5 atm of xenon, the efficiency of the TPC for completely containing an electron with an energy of 2.5 MeV was 22%, while for a double beta decay, the efficiency was 33%. Including the effects of bremsstrahlung, the total efficiency of the TPC (filled with xenon at 5 atm) for a 2.5 MeV electron was 15% and for double beta decay events, the efficiency was 25%.

CHAPTER FIVE

Design and Construction of the 200 liter TPC

1.1 Introduction

As discussed in Chapter 2, a viable double beta decay experiment must be capable of probing life-times of greater than 10^{23} years. In other words, the detector must be capable of detecting and identifying a few counts per year. The xenon TPC is ideally suited for such a sensitive search, since it can achieve excellent background rejection through a combination of trajectory recognition, energy-loss (dE/dx) measurements, and total energy measurements. This chapter presents a description of the various parameters of the TPC and a detailed account of the anode readout design.

5.2 Pressure

A double beta decay experiment requires a source with a large number of candidate decay nuclei and a detector that has a reasonable efficiency for detection of the decays. These requirements strongly suggest the use of a high-pressure gas TPC. However, at high pressures there is a high probability of the electron undergoing multiple scattering, resulting in shortened trajectories. Since electron diffusion is the primary limitation on the spatial resolution, working at too high a pressure may result in the loss of trajectory information. The Monte Carlo results suggested that a pressure of 5-10 atm was an optimal range for a high-pressure xenon TPC. At higher pressures the attenuation of the drifting electrons by contaminants (which varies as the square of the pressure) drastically reduces the charge collected on the anode

wires, and the higher voltages needed for the drift field and for proportional multiplication become difficult to handle.

5.3 Volume

Key considerations for setting the lower limit included the following: The active volume of the TPC had to be sufficiently large to contain enough candidate decay nuclei to give a reasonable signal to background ratio (recall that a 1 mole sample with $T_{1/2} = 10^{23}$ y will have only 4 disintegrations per year). Also, there had to be a large enough volume to allow a reasonable efficiency (i.e., the percentage of events that are fully contained and deposit all of their energy in the active volume) for double beta decays. From the Monte Carlo simulation, it was found that a cylindrical volume with height and diameter of 70 cm and 60 cm, respectively, when filled with a Xe-5%CH_4 mixture to 5 atm has a double beta decay efficiency of 25%. If the same system is operated at 10 atm, the efficiency increases to 53%. For the TPC, a cylindrical active volume, 70 cm high with a diameter of 61.5 cm was chosen. A gap of 5 cm from the inner wall in all directions protects against high voltage breakdown of the cathode and field shaping rings. A 208 l TPC operating at 5 atm and containing xenon enriched by 60% in ^{136}Xe will hold 1.7×10^{25} ^{136}Xe atoms (28 moles).

5.4 Main Chamber

The main chamber of the TPC is a cylindrical OFHC (oxygen-free high conductivity) copper vessel having a diameter, height, and a wall thickness of 72.9 cm, 78 cm, and 5.1 cm, respectively. The vessel was designed for a maximum pressure of 15 atm. The lower cover contains the high voltage feedthrough to the cathode, whereas the readout system composed of the grid, anode and field wires, and the XY pad is mounted beneath the top cover.

5.5 Gas Composition

For the various reasons discussed in Chapter 3, pure xenon is not suitable for a TPC. To reduce electron diffusion, increase the electron drift speed, and enhance stability against high voltage breakdown during charge multiplication, a quenching gas must be added to the xenon. In this experiment, where the electrons have to be drifted up to 70 cm, the quench gas of 5% CH_4 increases the electron drift speed from 1 mm/μs to 1 cm/μs in an electric field of 200 V/cm-atm and reduces the diffusion by a factor of 10.

5.6 Gas purification and gas handling

The system had a gas manifold to which was attached a turbomolecular pump, a gas analyzer (Dycor), pressure gauges, and cylinders of xenon, argon and methane. Before introducing the fill gas, the system was evacuated to high vacuum. When xenon was used as the fill gas, it was recovered from the system by immersing the xenon recovery cylinder in liquid nitrogen.

The TPC performance is degraded by electronegative contaminants (O_2, H_2O etc.), which attenuate the drifting secondary electrons. In order to keep this attenuation below 1% at 5 atm, contamination must be kept below 0.1 ppm. Hence, a continuous gas purification was needed. This was accomplished using a gas circulating pump, which moved continuosly the gas through a commercial purifier (Hydrox). A schematic of the system is shown in Figure (5.1).

5.7 Electric Drift Field

TPCs are usually used in high-count rate experiments. Thus, a large drift field is used since a large drift speed is required to move the electrons created in the ionization process to the readout system as soon as possible. Since double beta decay involves a low count rate, a large drift field is not crucial for the

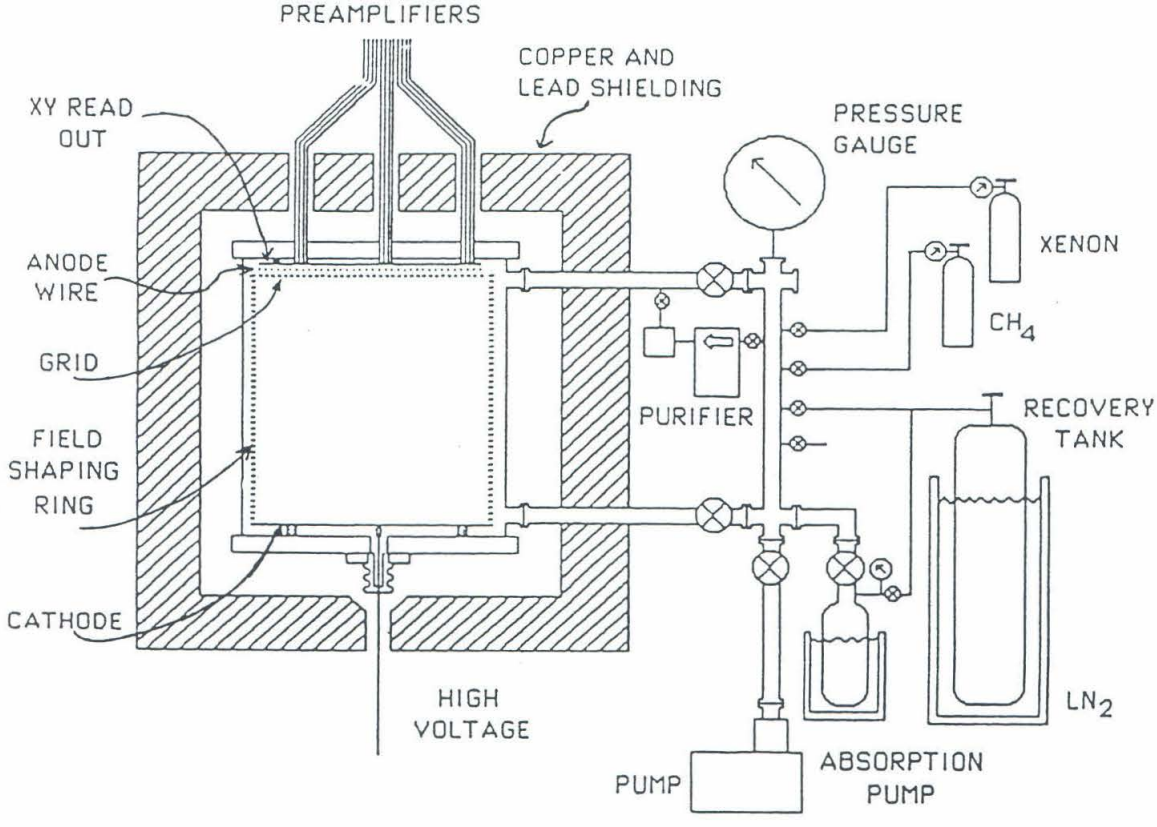

Figure (5.1) Schematic representation of the gas purification and gas handling system of the TPC.

xenon TPC. Actually, a small drift speed allows slower electronics and gives better spatial resolution along the drift direction. However, at these lower drift speeds, the diffusion of the secondary electrons increases, becoming a serious problem. In order to obtain an acceptable 1 cm/μs drift speed and limit the diffusion to 2 mm over a drift distance of 70 cm at an operating pressure of 5 atm, it is necessary to apply a voltage of the order of 60 kV at the cathode.

To insure that all secondary electrons drift parallel to the axis of the chamber at a constant speed, the electric field inside the active volume of the TPC must be uniform. Uniformity is achieved by using layers of field shaping rings at the edge of the detector. A calculation using relaxation techniques showed that rings of 0.15 cm thickness separated by 0.5 cm gave a field nonuniformity of less than 0.1% everywhere. This nonuniformity corresponds to a trajectory distortion well below the maximum diffusion width of 2 mm. At present, 70 field shaping rings, formed from 0.15 cm thick OFHC copper ribbon and with 10 MΩ resistors separating each ring, have been installed. The rings are supported by 3 delrin rods with delrin spacers between each ring. The resistors are the carbon composition type which, based on tests, appear to be free of radioactive contaminants.

5.8 Anode System

In the xenon TPC all the anode wires are tied together, and the summed signal from the wires is used to measure the energy of the electron (or any other particle traveling through the TPC). Basically, the system is a set of 200 proportional counters connected in parallel. As shown in Figure (5.2) each counter consists of an anode wire, two field wires, and a section of the XY pad. The function of the field wires is to enhance proportional multiplication and to ensure that charge multiplication at a point triggers only those pads directly above. A 95% transparent grid between the anode wire plane and the topmost

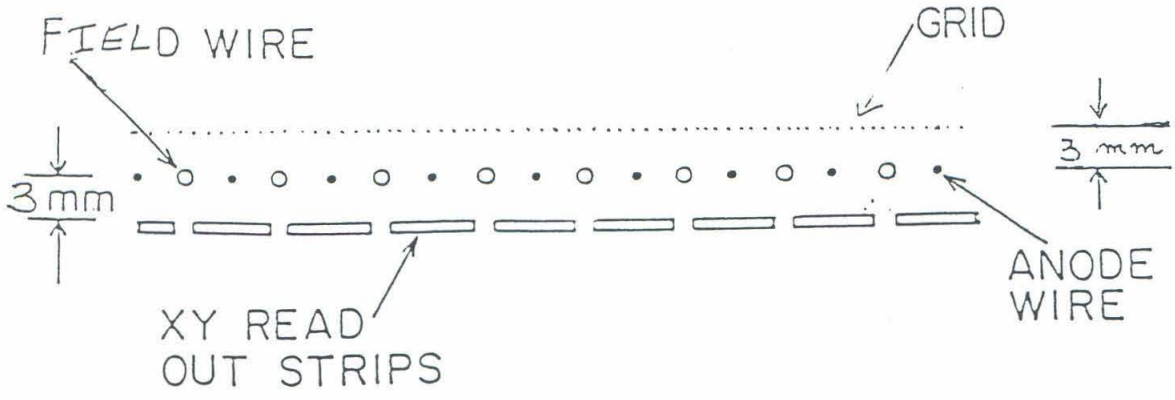

Figure (5.2) Schematic representation of the anode readout system.

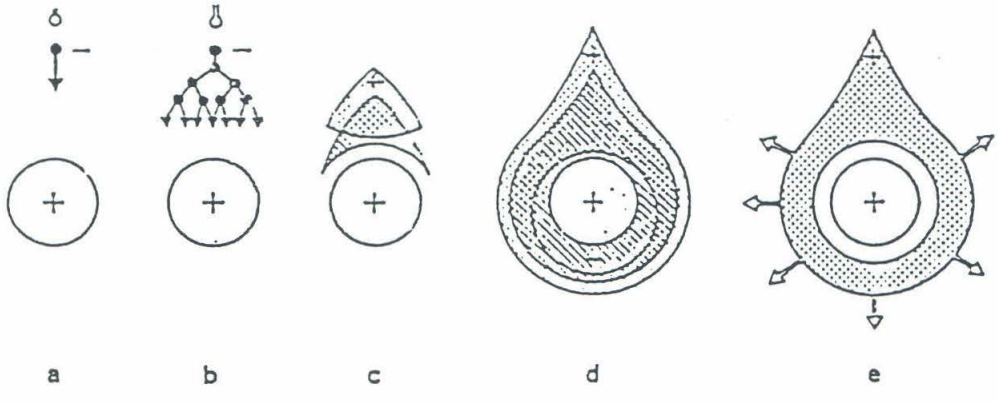

Figure (5.3) Simplified representation of the avalanche process around thin wires, [68].

field shaping ring isolates the readout system from the drift field region.

To help in understanding the operation of the anode system, a brief review of the theory of gas multiplication and the factors determining the energy resolution of a proportional counter will be presented in the following sections.

5.9 Basic Operation of a proportional counter

Usually, proportional counters are cylindrical chambers with a very thin wire stretched axially at the center of the chamber. The chamber wall is normally grounded and a positive voltage is applied to the central wire. The space between the electrodes, the chamber wall which constitutes the cathode and the central wire forming the anode, is filled with a gas. All or part of the energy of the ionizing particle passing through this space is dissipated through the formation of electron-ion pairs. Both the electrons and ions so produced move under the influence of the electric field. This motion of the charges induces a measurable current on the electrodes. The particles can be counted individually by transforming the charge produced by the radiation into a pulse and by counting the pulses.

When the electric field strength inside the counter exceeds a certain value, the electrons moving under the influence of the field acquire sufficient energy between collisions to produce new ions. Thus, more electrons are liberated, which in turn produce more electron-ion pairs. The net effect of this process is multiplication of the primary ionization. This phenomenon is called gas multiplication, also called gas gain, avalanche or gas amplification. For the cylindrical setup, as described above, the electric field is a maximum at the surface of the anode wire, and it rapidly decreases as 1/r towards the cathode. By using thin wires, very high electric field strengths are obtained close to the anode surface.

A schematic of the avalanche (multiplication) process is presented in Figure (5.3). The avalanche begins at a distance less than three wire radii from the anode surface. Since the drift speed of the electrons is about 5 cm/μs in this region (with p-10 (Argon + 10% Methane) as the fill gas), the avalanche takes place in less than 1 nanosecond. By this time the electrons have been collected on the anode and the positive ion sheath has begun drifting toward the cathode with decreasing speed. The detected signal *negative* on the anode and *positive* on the cathode is the result of the change in energy of the system caused by the movement of charges.

In the absence of nonlinear effects, the charge Q, which is developed in a pulse from a proportional counter can be assumed to be the sum of the charges from each avalanche. If the incident radiation creates N_o electron-ion pairs and if M represents the average multiplication factor from all the avalanches that contribute to a given pulse, then

$$Q = N_o e M .$$

The pulse amplitude is proportional to Q. Because both N_o and M show some inherent variation, the pulse amplitude fluctuates from pulse to pulse, even in the case of equal energy being deposited by the incident radiation. Assuming N_o and M are independent, the predicted relative variance in Q is given by:

$$\left[\frac{\sigma_Q}{Q}\right]^2 = \left[\frac{\sigma_{N_o}}{N_o}\right]^2 + \left[\frac{\sigma_M}{M}\right]^2 \qquad (5.1)$$

Since

$$M = 1/N_o \sum_{i=1}^{N_0} A_i = \overline{A},$$

where A_i, is the multiplication factor for the avalanche triggered by the i^{th} electron-ion pair, then

$$\sigma_M{}^2 = \sigma_A{}^2 / N_0,$$

where it is assumed that each avalanche is independent. Hence,

$$\left[\frac{\sigma_Q}{Q}\right]^2 = \left[\frac{\sigma_{N_o}}{N_o}\right]^2 + \frac{1}{N_0} \times \left[\frac{\sigma_A}{\overline{A}}\right]^2 \tag{5.2}$$

or in other words, the fractional variance of the pulse amplitude is made up of the ion pair fluctuations and the single-electron multiplication variations.

The first term can be expressed in terms of the Fano factor F [65],

$$\left[\frac{\sigma_{N_o}}{N_o}\right]^2 = \frac{F}{N_o}.$$

In a model proposed by Byrne [66], the single-electron multiplication variations are predicted to be

$$\left[\frac{\sigma_A}{\overline{A}}\right]^2 = \frac{1}{\overline{A}} + b,$$

where $b \equiv (1+\theta)^{-1}$ (θ is a parameter related to the fraction of electrons whose energy exceeds a threshold energy for ionization). For large values of the multiplication $\overline{A}$,

$$\left[\frac{\sigma_A}{\overline{A}}\right]^2 \simeq b.$$

Now, Equation (5.2) can be written as

$$\left[\frac{\sigma_Q}{Q}\right]^2 = \frac{F+b}{N_o}. \tag{5.3}$$

Typically, for the gas mixtures used in proportional counters, F ranges from 0.005 to 0.2, and b is between 0.4 and 0.7. Thus, the variance in the pulse amplitude is dominated by the fluctuations in the avalanche size. Since N_o = E/W, where E is the energy deposited by the incident radiation and W is the energy needed to form one ion pair,

$$\frac{\sigma_Q}{Q} = \left(\frac{W(F+b)}{E}\right)^{1/2} = \left(\frac{C}{E}\right)^{1/2} . \qquad (5.4)$$

Consequently, the statistical limit of the energy resolution in a proportional counter is expected to vary inversely with the square root of the energy deposited by the incident radiation.

In the real world, to get an estimate for the energy resolution, the factors affecting the multiplication M must be determined. By controlling these factors, the statistical limit should be approachable.

The goal is to achieve an energy resolution of 5% at 2.5 MeV. Substituting typical values of F and b for xenon at 2.5 MeV into Equation (5.4), the statistical limit on the energy resolution is $\approx$ 1%. In order to achieve the goal resolution, great care must be taken to minimize the effects of electronic noise, geometrical nonuniformities in the chamber, and variations in the operating parameters of the detector. These latter two effects influence the variation in M. The noise level of the electronics used here was of the order of 1%, which was a negligible contribution compared to the variations in M.

5.10 Dependence of M on mechanical tolerances

Various analytical expressions relate the gas multiplication factor to the counter parameters. Among the most widely used is that by Diethorn [67], which can be written as follows:

$$\ln M = \frac{V}{\ln(b/a)} \cdot \frac{\ln 2}{\Delta V} \left[\ln \left(\frac{V}{pa \ln(b/a)} \right) - \ln K \right] , \qquad (5.5)$$

where

V = applied voltage

a = anode radius

b = cathode radius

p = gas pressure

Δ V corresponds to the potential difference through which an electron moves between successive ionizing events, and K represents the minimum value of E/p; E is the electric field below which multiplication cannot occur. ΔV and K are constants for any given fill gas. For Xe with 10% CH_4, ΔV = 33.9 V and K = 3.62 x 10^4 V/atm cm.

As can be seen from Equation (5.5), the gas multiplication depends on, among other things, the geometrical parameters of the counter setup. The pressure, p, is set at 5 atm and for the selected fill gas, the parameters ΔV and K are fixed. Hence, the only variables are a, b and V. First, though, the required value of M has to be determined. In a Xe-CH_4 gas mixture at 1 atm, a minimum ionizing particle deposits about 6.5 keV/cm. With a drift speed of 1cm/μs, typical current pulses of the order of 50 pA are obtained. The preamplifier used has a gain of 270 mV/μA with a noise level of 5 mV. Hence, to get a reasonable signal-to-noise ratio, a multiplication of the order 10^3-10^4 is needed.

Since the multiplication at a given operational voltage depends on the detailed shape and value of the electric field in the multiplication region, it can change along a wire or from wire to wire as a result of mechanical variations. The maximum tolerable difference in multiplication depends on the required energy resolution.

Working with Equation (5.5), it can be determined how variations in a, b, p and V affect the multiplication. First, define the following:

$$C \equiv \ln b/a;\ A \equiv \frac{V \ln 2}{\Delta V};\ B \equiv \frac{V}{paK}.$$

Differentiating M with respect to each of the above gives the following:

$$\left(\frac{\Delta M}{M}\right)_{b,p,V} = \frac{\Delta a}{a}\left(\frac{\ln M}{C} + \frac{A}{C}\left(\frac{1}{C} - 1\right)\right).$$

$$\left(\frac{\Delta M}{M}\right)_{a,p,V} = \frac{\Delta b}{b}\frac{1}{C}\left(\ln M + \frac{A}{C}\right)$$

$$\left(\frac{\Delta M}{M}\right)_{a,b,V} = \frac{\Delta p}{p}\left(\frac{A}{C}\right)$$

$$\left(\frac{\Delta M}{M}\right)_{a,b,p} = \frac{\Delta V}{V}\left(\ln M + \frac{A}{C}\right) \qquad (5.6)$$

In this experiment two anode systems were used. The first one, Mark 1, has an anode wire spacing of 7 mm. 20 μm stainless steel wires were used for the anode wires, and 75 μm copper wires were used for the field wires. Mark 2 had an anode wire spacing of 3.5 mm. 20 μm stainless steel wires were used for the anode wires and 37.5 μm stainless steel wires were used for the field wires. Using the values of a and b used in Mark 2 and the operating pressure, voltage, and multiplication, the following are obtained:

$$\left(\frac{\Delta M}{M}\right)_{b,p,V} = 3\frac{\Delta a}{a}$$

$$\left(\frac{\Delta M}{M}\right)_{a,p,V} = 2\frac{\Delta b}{b}$$

$$\left(\frac{\Delta M}{M}\right)_{a,b,V} = 5\frac{\Delta p}{p}$$

$$\left(\frac{\Delta M}{M}\right)_{a,b,p} = 12\frac{\Delta V}{V}. \qquad (5.7)$$

In order to achieve the desired energy resolution, percentage variations in M must be kept below 5% and can be achieved by constructing the system to the tolerances listed below:

(1) The diameter of the wire used for the anode should be uniform to within 2%. Stainless steel wire of 20 μm diameter supplied by the California

Fine Wire Company was used in the subject study as explained later. The diameter was certified to vary by less than 0.01% from the specified diameter. The wire was thoroughly cleaned before and during installation, because any grease or other contaminants on the wire result in insensitive regions for amplification and worsen the energy resolution.

(2) Variations in b must be kept below 2%. To do this, the location of each wire and the separation between the anode plane and the XY pad must be uniform to within 30μm. This latter restraint requires that the XY pad be flat to within 30μm and that the frame supporting the anode wire be such that it will not cause variations in the wire locations in excess of 2%. These latter tolerances proved to be most difficult to attain. First, it was not easy to construct the system within these tolerances. Second, the wires had to be mounted such that they would not be displaced by the electrostatic forces acting on them. This problem of electrostatic forces and how it was solved will be discussed in more detail in the next section.

(3) A stable power supply must be used to provide the voltage to the anode wires. An ORTEC 456 high voltage supply was used, the output of which has a ripple of a mV/kV, or at typical operating voltages, the voltage was stable to 0.0025 %. To keep fluctuations in M to less than 5%, the voltage supply should be stable to 0.5%; the selected power supply more than met the required tolerance. Again, it should be stressed that the anode system must be kept as clean as possible. Otherwise, microdischarges occur, which draw current from the power supply and cause variations in V.

(4) Pressure fluctuations should be kept to less than 1%. In the TPC, pressure variations were negligible below the 0.1 % level.

5.11 Electrostatic Forces

In the anode setup, the anode wires are not in a stable equilibrium condition when a difference of potential is applied. If one wire is slightly displaced from the middle plane, the wire will be attracted more to the side of the displacement and less to the other side. The movement would continue indefinitely if it were not for the restoring force of the mechanical tension in the wires.

In this section the critical tension that must be applied to the anode wires for stability is calculated. The anode system is composed of a large number of identical cells as shown in Figure (5.2). Each cell consists of a single anode wire suspended between 2 ground planes equidistant from two grounded field wires. Suppose the anode wire is displaced by a small distance, u, towards a field wire. The force per unit length between the line charge q_o on the anode wire and q_1 on the field wire is

$$F = -4\pi\varepsilon \frac{V_o^2}{d^2} \left(\frac{\ln \frac{2sd^2}{a^2 b}}{\ln 2s/a \, (\ln d^2/ab)^2} \right) u \, , \qquad (5.8)$$

where

V_o is the voltage applied to the anode

s is the separation between the anode and the ground plane formed by the X-Y pad

d is the separation between the anode and field wires

a is the radius of the anode wire

and b is the radius of the field wire.

If T is the mechanical tension of the wire, the restoring force per unit length is

$$R = T \frac{d^2 u}{dx^2} \, ,$$

where u = u(x) is the displacement along the length of the wire with the

boundary conditions u(o) = u(L) = 0 and L the total wire length. For equilibrium, the following must hold:

$$T\frac{d^2u}{dx^2} = -4\pi\varepsilon \frac{V_o^2}{d^2}\left(\frac{\ln\frac{2sd^2}{a^2b}}{\ln 2s/a\ (\ln d^2/ab)^2}\right) u\ .$$

Solving this equation and satisfying the boundary conditions give the following:

$$T_{af} = \frac{L^2V_o^2}{d^2}\ \frac{4\varepsilon}{\pi}\ \frac{\ln\frac{2sd^2}{a^2b}}{\ln 2\frac{s}{a}\left(\ln\frac{d^2}{ab}\right)^2}\ . \tag{5.9}$$

For tensions larger than T_{af}, no solution is possible other than u(x)≡ 0, which means that the anode wires remain stable against deflections towards the neighboring field wires. In a similar way, to keep the wires stable against deflections toward the ground planes, it is necessary to apply a tension greater than

$$T_{ag} = \frac{L^2V_o^2}{s^2}\ \frac{4\varepsilon}{\pi}\ \frac{\ln\frac{2sd^2}{a^2b}}{\left(\ln 2\frac{s}{a}\right)^2 \ln\frac{d^2}{ab}}\ . \tag{5.10}$$

In the TPC Mark 2 anode readout system, s = 3mm, d = 1.75mm, a = 10μm, and b = 19μm. Using these values and Equations (5.9) and (5.10) gives the following expressions for the critical tensions:

$$T_{af} = 10.0\ V_o^2\ L^2 \tag{5.11}$$

$$T_{ag} = 5.2\ V_0^2\ L^2\ , \tag{5.12}$$

where T, L and V_o are expressed in grams, meters, and kV, respectively. If there is a tension T_c where $T_c > T_{af}$ is applied, then the wires should be stable

against deflections towards the field wires and the X-Y pad.

The maximum mechanical tension that can be applied before inelastic deformation depends on the material and the diameter of the wire. Using thinner wires allows the use of a lower voltage, V_o, for a given multiplication; however, the amount of tension that can be applied before the wire breaks is also limited. By studying the interplay between all these factors, it was finally decided to use 20 μm stainless steel wire for the anode. Since the TPC operates at 5 atm using a Xe - 5% CH_4 mixture, a voltage of about 2750 V must be applied to give the necessary gain. However, to give a reasonable range of voltages to work with, the system was designed to operate at 3.5 kV. Thus, a tension of 51g was applied to the anode wires. Since the breaking strength of the wire is 73 g, the wires were comfortably away from the inelastic deformation region. A 100g force was applied to the field wires. The wires that form the grid were wound on the opposite side of the supporting frame. To assist in keeping this frame rigid, a force of 150g was applied to these 50μm diameter stainless steel wires. The total number of wires on each side of the frame of course is the same. A more detailed description of the actual construction process is presented in [59].

5.12 Space - Charge Effects

As mentioned earlier, the electrons produced in the avalanche process are collected quickly on the anode, whereas the positive ions move more slowly. The ions, which are formed preferentially near the anode wire, form a space-charge that reduces the electric field in the region around the anode wire. The normal field is completely restored only when all the ions have been collected at the cathode. When in the proportional mode, the extension of the avalanche is small, between 0.1 mm and 0.5 mm; thus, the field modification is confined to a small region of the counter. If this modification is large enough, it can

reduce considerably the size of the output pulse. Since the amount of reduction is likely to vary depending on the detailed geometry of each ionizing event, these space-charge nonlinearities can have quite an effect on the energy resolution.

Space-charge effects fit into two different categories: self-induced effects and general space-charge effects. Self-induced effects arise when the gas gain is sufficiently high to cause positive ions formed during a given avalanche to alter the field and to reduce the number of electrons produced in further stages of the same avalanche. This effect depends on the magnitude of the multiplication and the geometry of the counter, but is independent of the pulse rate. The other category, the general space-charge effect, is the cumulative effect of positive ions produced from many different avalanches. Sauli [68] has derived an equation that calculates the approximate change in the anode potential V_o caused by a flux R of ionizing events, which produce nMe ion pairs in the avalanche, as follows:

$$\Delta V = \frac{nMeRT}{4\pi^2\varepsilon} = kMR \,, \tag{5.13}$$

where T is the total drift time of positive ions. Using the above and the expression for M, the corresponding change in the gain can be obtained. For small variations of ΔV it can be shown that

$$M = M_o \, e^{-\Delta V} \,. \tag{5.14}$$

Thus, the gain decreases exponentially. This is why, in general, most people working with proportional counters recommend using multiplication factors that are as low as possible, consistent with the signal- to-noise requirements, in order to avoid potential loss of energy resolution because of space-charge effects within the counter. In order to keep the anode system stable against electrostatic deflections and to limit the effects of space-charges on the energy resolution the TPC anode system operated at the relatively low multiplication

factor of 1000.

Chapter 6 gives a detailed description of the electronics for the anode readout.

5.13 X - Y Readout and feedthroughs

A schematic of the X-Y readout system is shown in Figure (5.4). The design was etched on one side of a copper-cladded Rexolite 1422 board [Oak Materials Group Inc.]. An identical pattern, horizontally shifted by one unit, was etched on the other side of the board. Forty thousand plated through holes connect the two sides, resulting in continuous channels. Adjacent channels are separated by 3.5mm (this defines the best achievable x-y resolution). The whole pattern fills a circle, 60 cm in diameter, giving 168 channels in both x and y.

Rexolite 1422 was chosen to reduce internal background. Typical circuit boards use glass fiber for structural support. However, Rexolite 1422 is made of pure resin; thus, the possibility of contamination from ^{40}K is minimal. However, unlike typical circuit boards, this material has no structural stability. Making the board stable and flat to the tolerances specified earlier had to be solved. The board was flattened through the use of a honeycomb structure constructed from 0.5 mm delrin strips, one side of which was attached to the Rexolite board using an epoxy made from Shell 826 epon resin and Versamid 140 polyamide resin, and the other side to a 0.5 mm thick OFHC copper disk. With this structure the board was uniformly flat to within 25 μm.

The connections between the pads and the feedthroughs on the cover were made using 20 ASWG stranded OFHC copper wire, which had a 75 μm teflon sleeving. The wires were soldered to the pad terminals using 63/47 solder. Based on tests, both the solder and the resins were not contaminated

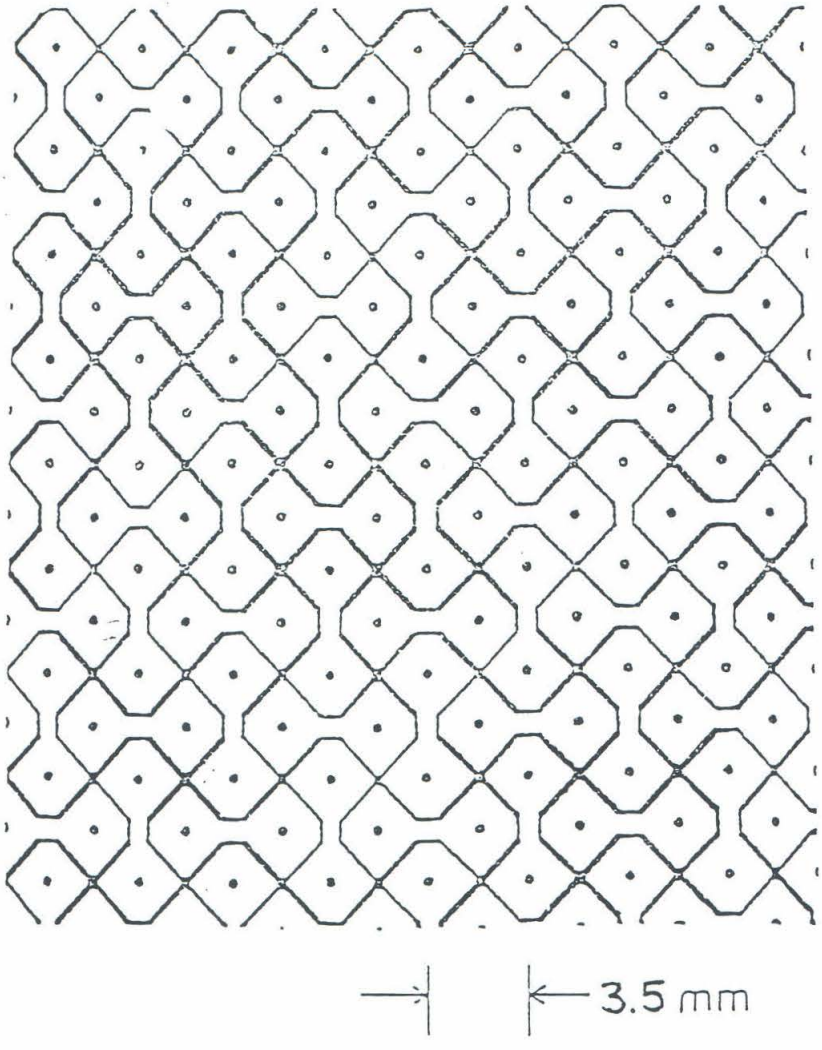

Figure (5.4) Schematic of the X-Y readout pattern. The black lines represent regions where the copper was etched off the circuit board, while the dots represent the plated through holes. The x channels are horizontal and the y channels vertical.

with radioactive materials. The feedthroughs were made from "clean" materials: copper, delrin, and teflon. There were a total of 16 feedthrough units, 4 of which contained 21 connector pins and 1 high voltage connector, 12 of which had 25 connector pins.

5.14 Veto System

In the laboratory at Caltech, three hardware vetos for reducing background events were used. The first one was a 2 mm copper ring, divided into four sectors, around the outside of the X-Y readout strips. Every time a trajectory crossed the cylindrical boundary, the signal from the sector over which the particle passes was used to veto the incomplete event. The second veto was an energy cut. Since ^{85}K is expected to be the dominant background at energies below the ^{85}K beta spectrum endpoint at 683 keV, all events below this energy were vetoed. A more detailed description of the ^{85}K issue is given in Section 5.16. The third veto was a 147 cm x 147 cm x 12 cm liquid scintillator panel which was used to veto cosmic ray events.

5.15 Shielding and Calibration

The system is designed so that the main chamber can be surrounded with up to 30 cm of copper and lead shielding. The electronics and gas-handling apparatus will be outside this shielding. At Caltech no shielding was used.

At Caltech the anode wire signals were calibrated using the internal conversion sources ^{113}Sn and ^{207}Bi, which were placed at the center of the cathode. Vertical muons traveling through the TPC was used to check the uniformity of the electric field, to adjust signals from the readout strips, and to measure the drift velocity and hence monitor the Xe - CH_4 ratio.

5.16 Background Sources

For this low count rate experiment, a proper understanding of the background is very important. The various background sources are discussed below:

Cosmic Rays:

In the laboratory at Caltech, the rate of muon-induced events in the TPC is about 100 per sec. The veto ring surrounding the readout pads and the scintillator panels reject most of these events. Thus, the only contribution these events make is 60 ms per second to the system dead time. However, the problem of muon capture in the copper and lead shielding could affect the experiment. This muon capture process can produce neutrons which, when captured, will produce high energy gamma rays. The gamma rays can then interact to produce electrons in the TPC. How these electrons contribute to the background is discussed in the section titled Gamma Rays. To reduce this muon induced background, the TPC has been installed in an underground laboratory located in the St. Gotthard tunnel in Switzerland. This location has a rock overburden of approximately 1000 m, which provides about 3000 m water equivalent of shielding. Thus, the muon flux is attenuated by a factor of 10^5. In this underground laboratory the expected muon flux through the TPC is of the order of thirty per day. Tracks from these events will be stored and used for calibration purposes.

At sea level the fast neutrons contained in the cosmic rays can interact with the copper in the TPC to produce unstable isotopes. These isotopes decay, once the experiment is moved underground and the intensities of the emitted decay lines decline.

^{85}Kr:

Commercial xenon contains about 15 ppm of krypton, about 1 part in 10^{12} of which is ^{85}Kr, a beta emitter with an endpoint energy of 0.68 MeV and half-life of 10.7 years. This will give a low energy background at the rate of about one event per second in the TPC. In order to reduce the dead time of the electronics, events below the ^{85}Kr endpoint energy are rejected using a hardware veto. If necessary, the krypton contamination can be reduced by fractional distillation, and use of the TPC with enriched ^{136}Xe should significantly reduce the background from the ^{85}Kr.

Gamma Rays:

Even though the TPC is constructed from low background materials and is surrounded by elaborate shielding, there will always be some gamma-ray-induced background because of natural radioactivity from sources both internal and external to the TPC. The major contribution to the background are electrons produced inside the TPC by Compton scattering. At the cost of electronic dead time and computer CPU time for data analysis, most single electron trajectories can be rejected as they will not have charge blobs at both ends. The gamma-ray-induced background events that look similar to double beta decay events (electron trajectories with a charge blob at each end) include:

1) *Single Electrons with initial Charge Blobs*. Single electron trajectories can be produced by Compton scattering and photoelectric absorption of the incident photon. In xenon for a 2.5 MeV gamma ray, the photoelectric cross section is about a factor of thirty less than the cross section for Compton scattering. Most single electron trajectories can be rejected at the cost of the electronic dead time. However, an electron may produce energetic secondary electrons (δ electrons), which give high charge accumulation at the beginning of the trajectories. The Monte Carlo calculation showed that $\approx$5% of electrons, with an energy of 2.5 MeV, have charge blobs in the first 5 mm of the track, making it

difficult to distinguish these from real events. For these cases, the increase in the second derivative of the trajectories at both ends will be investigated, single electron events will have a low second derivative at the begining of the track.

2) *Pair production.* In the TPC, it is not possible to distinguish electrons from positrons; thus, a pair production event will look similar to a double beta decay event. However, the vertex of the trajectory produced by pair production is sharply peaked ($< 70^{\circ}$ when the two leptons have comparable energy). Thus, events with a sharp vertex near the center portion of the trajectory can be rejected. Also, 8% of the 511 keV positron annihilation gamma rays will produce a Compton electron inside the TPC, thus allowing further rejection of pair production events by looking for multiple tracks within the same event.

3) *Double Compton Scattering.* The photon, following a Compton scattering, can scatter again within 3 mm (the resolution of the TPC) so that the two trajectories cannot be separated.

5.17 Estimation of background events

The probability that an incoming photon will produce an event inside the TPC filled with 5 atm of xenon has been estimated. The gamma ray flux in the underground laboratory has been carefully measured [42], and was found to drop exponentially with energy. The rate was about $6x10^6$/MeV-y-cm^2 at 2.5 MeV and $4x10^5$/MeV-y-cm^2 at 3.5 MeV. The 30 cm of lead shielding around the TPC together with the 5 cm wall thickness of the copper vessel will attenuate the intensity of the 2.5 MeV and 3.5 MeV gamma rays by a factor of $6.6x10^{-8}$ and $1.5x10^{-7}$, respectively, [69]. The Monte Carlo calculated the efficiency for completely enclosing a 2.5 MeV electron in the TPC to be 5 %. For pair production and double compton scattering events the calculated efficiency was 20 %. The rejection efficiency for single electrons events was estimated by the Monte Carlo to be 95%. If it is assumed that inside the TPC

the average path length of the gamma rays is about 60 cm ($2gm/cm^2$ for 5 atm of xenon) [69], the total number of background events caused by pair production and Compton scattering can be estimated. Using the efficiencies as calculated by the Monte Carlo and an energy resolution of 5% at 2.5 MeV, the contribution to the background (B) from external gamma rays in an energy window (2480 ± 62) keV was estimated to be 0.57 counts per year (Table 5.1).

At this stage of the experiment, contributions to the background from possible internal radioactive contaminants cannot be estimated. However, by carefully selecting the construction materials of the TPC and using lead shielding, it should be possible to keep this contribution considerably lower than that of the external sources.

5.18 Estimation of a $0\nu\beta\beta$ decay lifetime limit

In a time interval t the number of $0\nu\beta\beta$ decays is given by

$$N_{decay} = N_o \left[1 - e^{-\frac{t \ln 2}{t_{1/2}}}\right],$$

where

$$N_0 = \frac{VPN_AE}{V_m},$$

V = active volume of the TPC in liters

P = operating pressure of the TPC in atms

N_A = 6.02×10^{23} atoms/mole

V_m = 22.4 liter-atm/mole

E = concentration of the source

t = the runtime of the experiment

$t_{1/2}$ = $0\nu\beta\beta$ halflife.

	2.5 MeV	3.5 MeV
γ ray flux per MeV - y - cm^2 [42]	6.1×10^{6}	4.4×10^{5}
Attenuation that is due to shielding from 30 cm of lead and 5 cm of copper [69]	6.6×10^{-8}	1.5×10^{-7}
Compton electrons produced per MeV - y [a]	380	74
Pair production at 2.5 MeV per MeV - y [b]	---	19
Background events from Compton electrons per year (5 % detector efficiency, 3 % with initial charge blob, 5 % energy resolution)	0.09	---
Background events from pair production per year (20 % detector efficiency, 5 % energy resolution)	---	0.48

Table (5.1) Estimation of background events in a 125 keV window at 2.5 MeV.

(a) It was assumed that γ-ray makes Compton electrons below its energy with equal probability. Total probability of interaction is given by approx. 1-exp(-μt), wher μ for Xe is (0.032-0.026) cm^2/g for 2.5-3.5 MeV. It was assumed that the average path length for the γ rays was 60 cm.

(b) Probability approx 1-exp(-μt), where for Xe μ = 0.01 cm^2/g and an average path length for γ rays of 60 cm was assumed.

For $t << t_{1/2}$,

$$N_{decay} \approx \frac{N_0 t \ln 2}{t_{1/2}} .$$

If, in the time t, a total count rate equal to C is observed, and the background count rate is B then

$$N_{decay} = \frac{C-B}{\varepsilon} ,$$

where ε is the efficiency of the TPC for $0\nu\beta\beta$ decay events. Thus, the halflife can be expressed as

$$t_{1/2} = \frac{N_0 t \varepsilon \ln 2}{C-B} . \qquad (5.15)$$

The first issue one needs to resolve is the following: Given C observed counts (with an average of B background events), does a $0\nu\beta\beta$ decay signal r=C-B exist? The probability that an average of B background events will fluctuate to greater than or equal to C observed events,

$$P(\text{background} \geq C) = 1 - \sum_{n=0}^{C-1} \frac{e^{-B} B^n}{n!}$$

is calculated. If this number is small (e.g. $P<0.05$) then one can claim that a signal is present. If the above is true then the most likely value of the signal (r_0) and the associated upper and lower limits of r_0 are calculated.

A conservative estimate of the lower limit of the halflife can be obtained by estimating a 90% upper confidence limit for the expected $0\nu\beta\beta$ decay signal r = C - B, and taking the minimum values of N_o and ε.

The probability of obtaining C counts (C=r+B) is [70],

$$P(C) = \frac{e^{-(r+B)} (r+B)^C}{C!} .$$

The probability density function (p.d.f.) of r after the experiment (g(r)) can be obtained by using Bayes theorem [71],

$$g(r \mid C) = \frac{P(C \mid r)\, P(r)}{\int P(C \mid r)\, P(r) dr} . \tag{5.16}$$

Equation (5.16) can be interpreted in the following way: g (r|C) expresses the degree of belief in where the true value of r lies given the result C of the experiment. P(r) gives the state of belief in where the true value of r lies prior to the current experiment, i.e. P(r) is the "prior" probability distribution. In this analysis it is assumed that we have no prior knowledge of r and the popular expression of ignorance P(r) = constant (in the allowed region) is used. A detailed discussion of this issue is presented in [72] and [73]. Substituting P(r) = Θ(r) (where Θ(r) is the step function, Θ(r) = 0 if r<0 and Θ(r) = 1 if r $\geq$0) into equation (5.16) gives the following

$$g(r \mid C) = g(r) = \frac{N_1 e^{-(r+B)}\, (r+B)^C}{C!} , \tag{5.17}$$

where N_1 is a normalization constant such that

$$\int_{-\infty}^{\infty} g(r) dr = 1.$$

Equation (5.17) is valid when the background is exactly known or has a negligible standard deviation. If the above is not the case then g(r) is given by

$$g(r) = N_2 \int_0^{\infty} \frac{e^{-(r+B)}\, (r+B)^C}{C!}\, f(B)\, dB , \tag{5.18}$$

where N_2 is a normalization constant and f(B) is the background p.d.f..

In this analysis it is assumed that f(B) has a Gaussian shape and a conservative estimate of the error in determining B (σ_B) is that σ_B is of the order of 10% of B. In the actual experiment B will be measured along with σ_B.

In the estimate of the 90% CL upper limit of r, (R), the value B-σ_B was used for B in equation (5.17). By solving the following equation,

$$0.90 = \frac{\int_{r=0}^{R} \frac{e^{-(r+B-\sigma_B)}\,(r+B-\sigma_b)^C}{C!}}{\int_{r=0}^{\infty} \frac{e^{-(r+B-\sigma_B)}\,(r+B-\sigma_B)^C}{C!}}, \qquad (5.19)$$

R was calculated for various values of C and the results are presented in Table 5.2. Actually in the integral in the denominator ∞ is replaced by the value of r where the likelihood function goes to 0.

In the case of the enriched isotope the values of the various parameters are as follows: E=(62.11±0.75)%, V=(208.7± 0.9) liters and P=(5± 0.005) atm. Using the above values of E, V and P, N_0 was estimated to be equal to $(1.74\pm0.02)\times10^{25}$ atoms. The error in ε was estimated by running the Monte Carlo simulation many times and then calculating the statistical error. The result so obtained was ε=(25± 0.6)%. Thus, the minimum values of N_0 and ε are; N_0-ΔN_0 = 1.72×10^{25} atoms and ε-$\Delta\varepsilon$ = 24.4%. Hence, the conservative estimate for the upper limit on the halflife is

$$t_{1/2}^{90\%} = \frac{2.9\times10^{24}}{R}\ \text{y},$$

for a runtime of 1 year. Using the values of R as given in Table 5.2, $t_{1/2}^{90\%}$ was calculated for various values of C. The results are presented in Table 5.3.

Note that while ΔN_0 and $\Delta\varepsilon$ contribute to the systematic error in the halflife estimate, the 90% CL upper limit on r is the statistical error. Running the experiment twice as long reduces the latter but not the former error.

Given that a signal is observed one would like to quote a measured life-time. To do this the value of r where the likelihood function is a maximum (r_0) is calculated. The central values for N_0(1.74×10^{25} atoms), ε(25%) and r_0 are then used to obtain a lifetime $t_{1/2}^{meas}$

$$t_{1/2}^{meas} = \frac{3.02\times10^{24}}{r_0}\text{y},$$

for a runtime of one year. Using the values of r_0 as given in Table 5.2, $t_{1/2}^{meas}$ was calculated for various values of C. The results are presented in Table 5.3.

As shown in Figure (5.5) the likelihood distribution is asymmetric. Thus the upper and lower errors on r_0 are also asymmetric. These errors are obtained by taking the values of r (r_{low} and r_{upp}) which have an equal likelihood and such that the range r_{low} to r_{upp} encloses 68.3% of the total (apriori allowed) probability, (see Figure (5.5)). For each value of r_0, r_{low} and r_{upp} were calculated and the range of $t_{1/2}^{meas}$ was calculated (lower limit $t_{1/2}^{ll} = 3.02\times10^{24}/r_{upp}$ years and the upper limit $t_{1/2}^{ul} = 3.02\times10^{24}/r_{low}$ years).

If one count is observed in a 250 keV bin at 2.5 MeV, from Table 5.3 it can be seen that the a conservative estimate for the $0\nu\beta\beta$ decay halflife (at the 90% CL) is of the order of 8×10^{23} years. According to calculations [21,22], and considering the mass mechanism for $0\nu\beta\beta$ decay, the above lifetime corresponds to a neutrino mass in the range 0.3 to 3.3 eV.

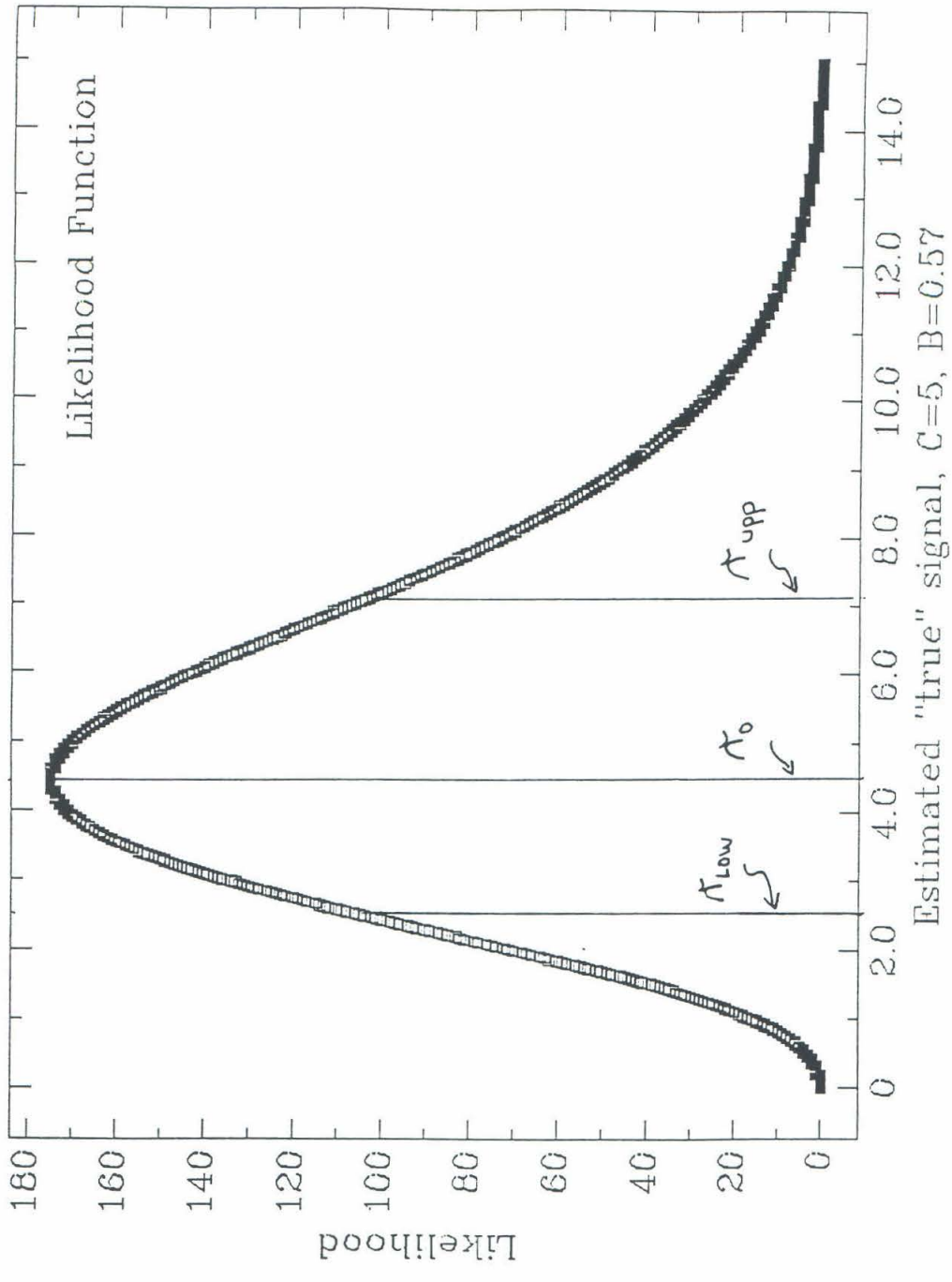

Figure (5.5) Likelihood Distribution of the "true" signal when 5 counts are observed and the background count is 0.57.

Estimated Background = 0.57 counts/250 keV.year at 2.5 MeV

C	f(B≥C)	R	r_0	r_{low}	r_{upp}
0	0.44	2.3	0	-	-
1	0.44	3.5	0.44	-	-
2	0.11	4.84	1.44	0.32	3.22
3	0.02	6.16	2.44	1.0	4.54
4	3×10^{-3}	7.48	3.42	1.72	5.82
5	3×10^{-4}	8.76	4.44	2.48	7.06
6	3×10^{-5}	10.02	5.42	3.28	8.24
7	2×10^{-6}	11.25	6.42	4.1	9.4
8	2×10^{-7}	12.4	7.42	4.96	10.52

Note: C=observed number of counts in 1 year in a 250 keV bin at 2.5 MeV, f(B≥C)=the probability that an average of B background events will fluctuate to ≥C observed events, R=90% CL upper limit on the $0\nu\beta\beta$ decay signal r, r_0 = the most likely value of r (r_0=C-B), r_{low} and r_{upp} are the values of r which have an equal likelihood and are such that the range r_{low} to r_{upp} encloses 68.3% of the total (apriori allowed) probability.

Table 5.2 Estimate of R, r_0, r_{low} and r_{upp} for various values of C.

C	$t_{1/2}^{90\%}$ --- (10^{24}yrs)	$t_{1/2}^{meas}$ --- (10^{24}yrs)	$t_{1/2}^{ll}$ --- (10^{24}yrs)	$t_{1/2}^{ul}$ --- (10^{24}yrs)
0	1.3×10^{24}	-	-	-
1	0.83	6.9	-	-
2	0.60	2.1	0.94	9.5
3	0.47	1.2	0.67	3.0
4	0.39	0.88	0.52	1.8
5	0.33	0.68	0.43	1.2
6	0.29	0.56	0.37	0.92
7	0.26	0.47	0.32	0.74
8	0.23	0.41	0.29	0.61

Table 5.3 Estimate of the $t_{1/2}^{90\%}$, $t_{1/2}^{meas}$, $t_{1/2}^{ll}$ and $t_{1/2}^{ul}$.

CHAPTER SIX

Data Acquisition and Processing System

6.1 Introduction

With a spatial resolution of 3.5 mm in both the x and y directions, the TPC has a total of 336 channels. The signals induced on the XY pads by the proportional multiplication around the anode wires need amplification. Unfortunately, since the electronic components used in making the preamplifiers contain possible sources of natural radioactivity, the preamplifiers cannot be located inside the TPC close to the XY pads. However, with the charge multiplication obtained from the anode system, the signals are large enough to carry outside the shielding (a distance of approximately 30 cm), where they are fed into the preamplifiers. Since to reconstruct the trajectory the time development of the signals is required, all the channels are connected to current sensitive preamplifiers.

As discussed in Chapter 4, it is possible to reconstruct a trajectory from the timing of the signals induced on the pads alone; therefore, the analog signal is not needed. Also, because of the multiple scattering, the analog signal cannot be used effectively for a center-of-gravity fit, which generally gives a better spatial resolution [74]. However, to look for the charge blob at the end of a trajectory, it is necessary to know the amplitudes of the signals from each channel. From the Monte Carlo simulation, as discussed in Chapter 4, it was found that full-scale digitization requiring flash ADC's in each channel is not necessary. Instead, a simple discriminator with two threshold levels suffices. One threshold is set slightly above the noise level of the XY pad signals, while the other is set at a level approximately 5 times higher. This arrangement allows

monitoring of the higher dE/dx (charge blobs) at the end of a trajectory. The discriminators have been designed in a modular fashion, thus allowing easy replacement by a flash ADC system, if necessary.

The schematic of the electronics and the data acquisition system is shown in Figure (6.1). Since the TPC does not have a time zero trigger, the recording of an event is started by a start trigger produced in the anode wire. Data within the next 64 μs (this being the longest drift time expected) are recorded. The inverted (positive) output of the anode preamplifier is digitized continously by a commercial transient recorder, the Le Croy TR8837F, at an 8 MHz rate. This recorder is a single-width CAMAC module, operates with standard CAMAC commands, has 8-bit digitization, programmable sampling speed (up to 32 MHz), memory size (up to 8 k) and pretrigger size. The CAMAC controller board provides the stop pulse for the transient recorder and so saves the energy information. The anode output is also integrated on line to find the total energy of an event. It is used to produce the energy trigger for those events with energy above the energy threshold. The output is also passed through the same discriminator system as the XY pad signals. The output of the higher threshold level provides the blob trigger. During this time the signals from the XY pads travel through preamplifiers and discriminators. The discriminator outputs are temporarily stored in the memory banks of the CAMAC interface modules. As mentioned in Chapter 5, using a Xe-CH_4 mixture, the electron drift speed is about 1cm/μs, using a drift field of 200 V/cm atm. Thus, if the XY signals are sampled at a rate of 8 MHz, a spatial resolution of 1.25 mm in the drift (z) direction can be achieved. To assist in computer interfacing, the interface modules were designed according to the CAMAC standard.

For a good event the memory banks in the CAMAC modules are read off by a PDP 11/73, which acts as a front-end processor. The PDP 11/73 compresses the data and sends it via Ethernet to a UNIX host (Tektronix

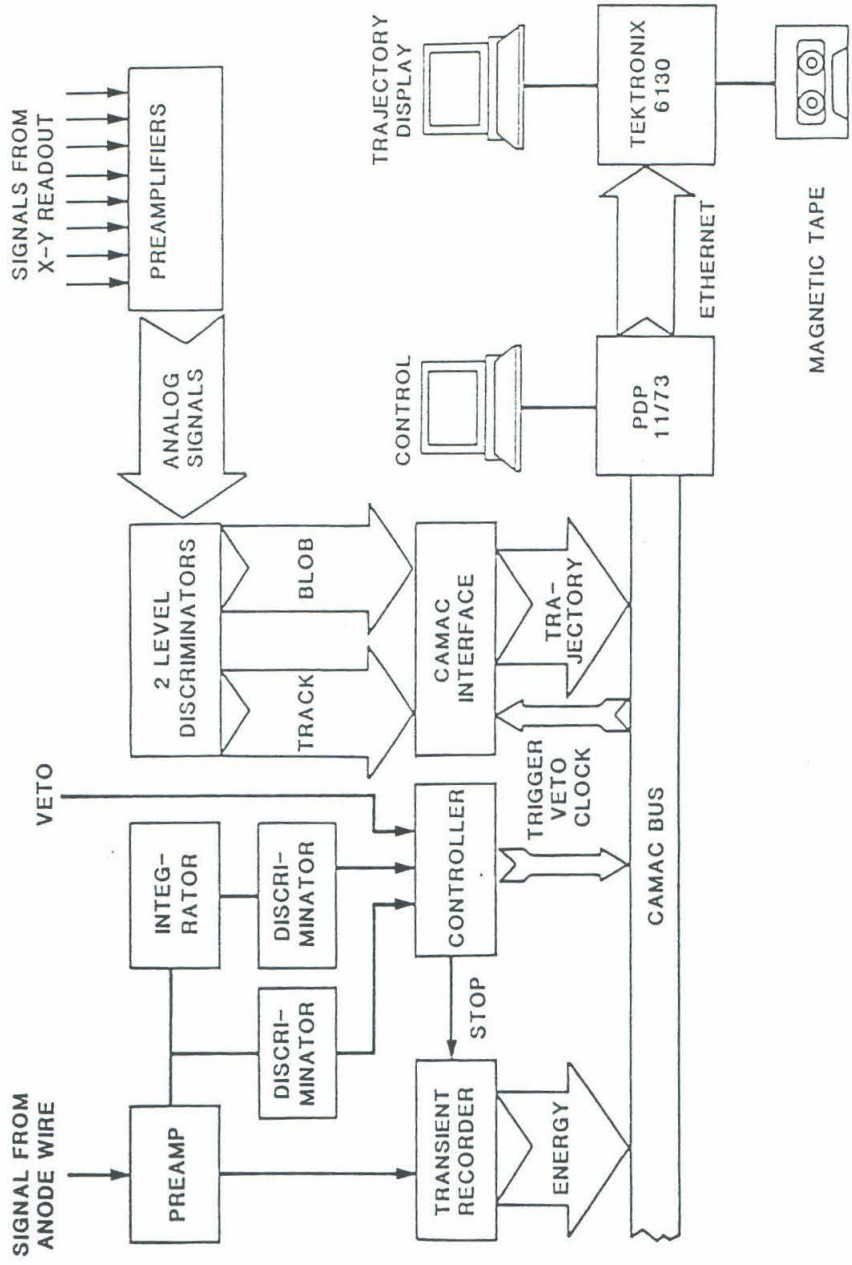

Figure (6.1) Schematic representation of the electronics and data acquisition system.

6130).

Basically, the readout electronics can be divided into 3 main parts: the preamplifiers, dicriminators, and the CAMAC interface. In the next few sections, a discussion of the individual components will be given.

6.2 Preamplifiers

In xenon at 5 atm, a minimum-ionizing electron deposits about 30 keV per cm of gas it passes through, resulting in the formation of about 1500 electron-ion pairs. For the case of a vertical trajectory, drifting these secondary electrons at a speed of 1 cm/μs to the readout system produces a current pulse greater than 0.25 nA. A proportional multiplication of 1000 boosts the current up to the μA level. By using a preamplifier with a current gain of a few 100 mV/μA, a reasonably sized output is obtained. The preamplifiers were designed using the Le Croy TRA1000 IC as the core. Figure (6.2) shows a schematic of the circuit. The preamplifier gain is 270 mV/μA. Twelve preamplifiers are mounted on a single board. These boards along with the required $\pm$ 12V power supply are mounted in a modified NIM crate. The complete electronics requires 28 such boards. The preamplifiers are capable of producing 800 mV pulses with a noise level of $\approx$ 5-10 mV; typically, during operation the pulses are about 200 mV.

The high voltage preamplifier that processes the anode signal uses the same circuit, except that the input capacitor is replaced with a high voltage capacitor (6kV, 100pF). The high voltage is applied through a 22 MΩ resistor; this is done so as to limit the current drawn from the power supply. To minimize the noise level, this preamplifier has been installed in a shielded box with a separate power supply.

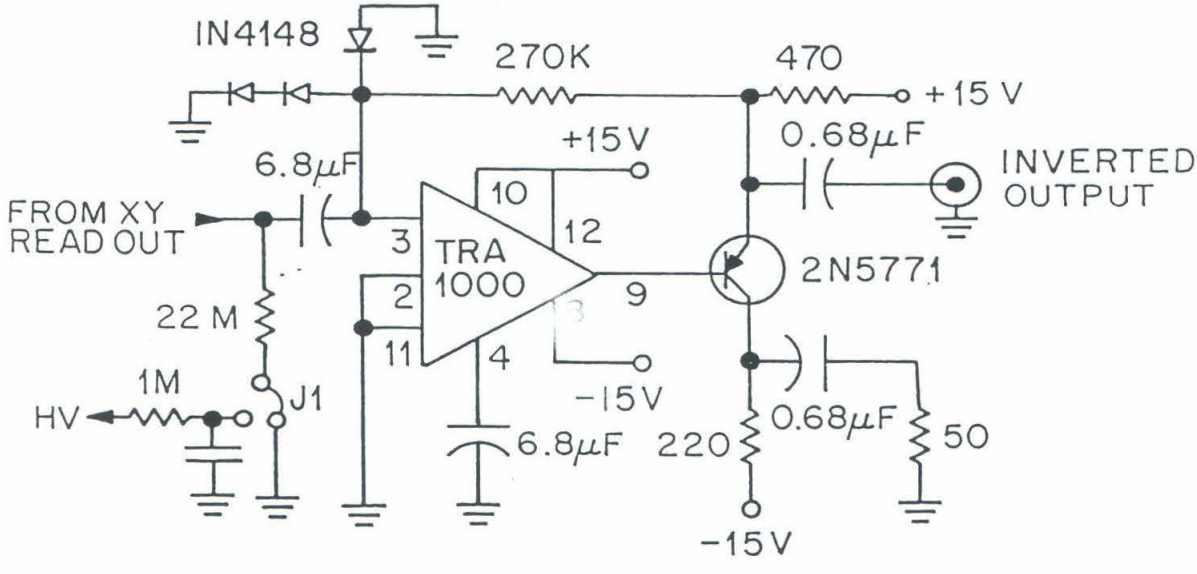

Figure (6.2) The circuit diagram of the preamplifier. For the X-Y readout channels, the inverted (negative) output was used. For the high voltage operation, the input capacitor was replaced by a high voltage blocking capacitor, and the jumper J1 was connected to the high voltage instead of ground.

6.3 Discriminators

Since a spatial resolution of a few mm corresponds to a few 100 ns drift time, a discriminator with a propagation time of a few 100 ns can be used. The discriminators were designed using low cost voltage comparators (LM319). The circuit diagram for one such unit is given in Figure (6.3). The input signal is fed into 2 comparators, each having a distinct threshold level, which can be adjusted using trimpots mounted on the front panel of the discriminator unit. Eight channels are grouped together and share the 2 threshold levels. Three such groups (24 channels) are mounted on a circuit board, which is mounted in a single width NIM module. For the complete electronics, a total of 14 such units are needed. The comparator outputs are TTL compatible. From noise consideration TTL low has been taken for the signal. The outputs pass through a properly terminated 74LS240 IC, and can be transmitted up to 3m through ribbon cables. Identical discriminators, each in a separate shielded box, are connected to the amplified signals of the anode system and the veto ring.

6.4 CAMAC Interface

The TTL outputs of the discriminators are stored in the memory banks located in single width CAMAC modules. Each module has 48 input lines and so can handle the output of a single discriminator module. The complete electronic system requires 14 such modules, all of which fit into a CAMAC crate. The modules can be run by an internal or external clock up to a maximum clock speed of 8 MHz. The memory size is programmable up to 2048. A single controller board receives the various triggers and veto signals and provides them to all the modules via the unused lines of the CAMAC bus. The controller board also provides the clock pulses to all the modules.

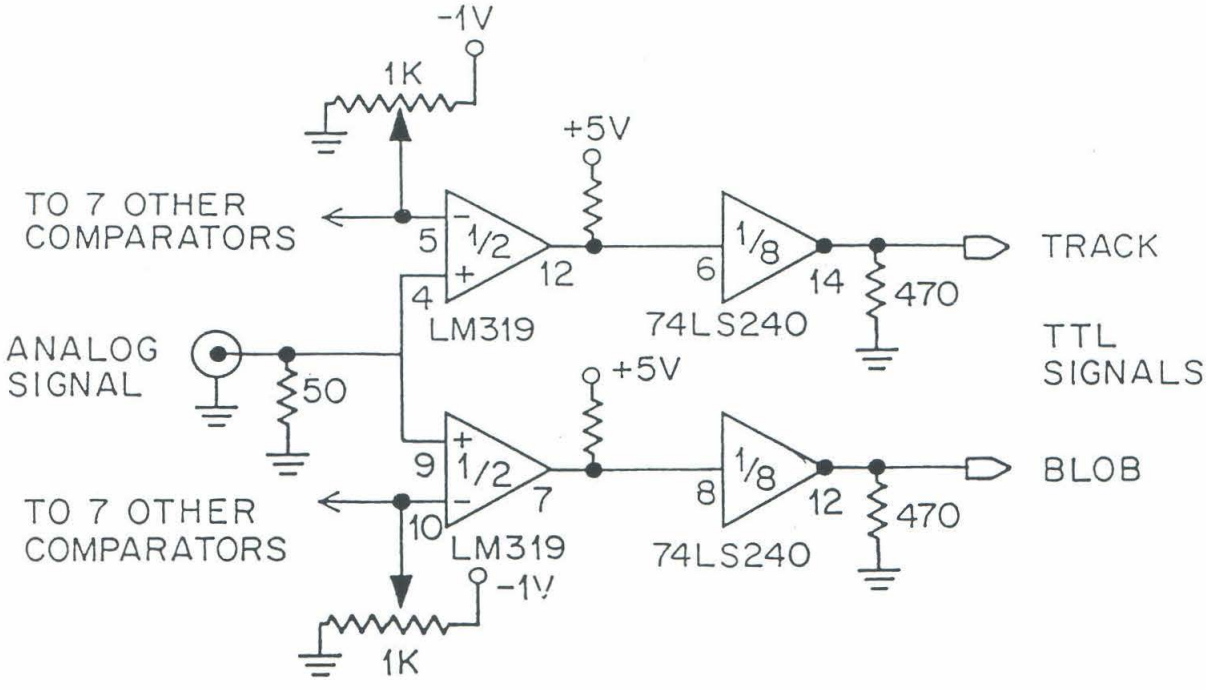

Figure (6.3) The circuit diagram for one unit of the discriminator.

A schematic diagram of the CAMAC interface circuit is shown in Figure (6.4). The modules have been designed so that the output signals from the low and high threshold levels of the discriminators are stored in 2 different memory blocks, the "track" and the "blob" blocks, respectively, which can be read independently. The modules can be in either the WRITE state (W line is low) or the READ state (R line is low). The WRITE/READ state can be selected using the CAMAC command F24/F25 (or C/Z for the whole crate). When in the WRITE state, the two input buffers and the RAM ICs are enabled. After the controller board receives the start trigger, the clock pulses increment the counter which, in turn, advances the RAM address for a predetermined time. In this manner the trajectory information is stored in the increasing address of the RAM IC as a function of time.

The data for the event are saved and a LAM signal is produced only if all the following conditions are satisfied:

(1) The start trigger is continuous and longer than a time selected by a switch on the front panel of the controller board. This condition will reject all short events that are due to noise and low energy (< 100 keV) electron tracks.

(2) There is a blob trigger. This condition helps in the rejection of all minimum ionizing events, for example, events generated by muons passing through the TPC.

(3) There is an energy trigger within one event period after the start trigger. This condition will cause the rejection of all those events whose energy is below a preselected energy.

(4) A veto signal is not received during the event, or within a period equal to the drift time before the start trigger.

The LAM signal produced at the end of a good event instructs the PDP 11/73 to read the memory. The status of the CAMAC interface is changed into the READ state, so that the input buffers are disabled and the outputs of the RAM ICs are enabled. The track and blob memory blocks are tested to see if

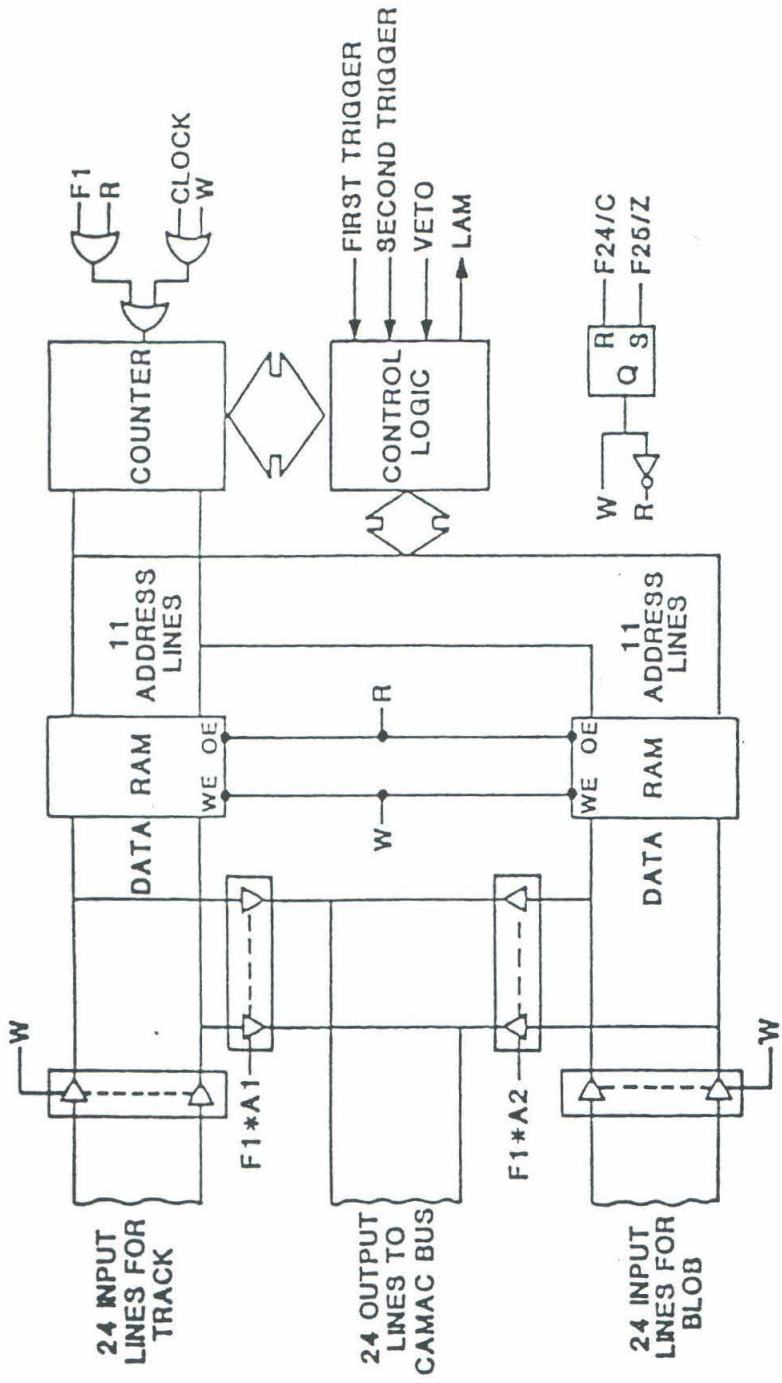

Figure (6.4) Schematic representation of the CAMAC interface module.

they contain any data by the CAMAC command F8*A1 for the track, and F8*A2 for the blob. When the counter is incremented by F1 pulses, those blocks containing data are read by F1*A1 and F1*A2, respectively.

There is one other interesting feature of the CAMAC interface design. For an 8 MHz clock rate, only 512 of the available 2048 k memory size are used for an event. The unused part is used to store delayed events that might occur within some specified time after the first event. These delayed events could prove useful in resolving some possible unusual background events.

6.5 Data Transfer

When the LAM is generated at the end of an event, the PDP 11/73 works as a front-end processor and accesses the transient recorder and the memory of the CAMAC modules via a standard CAMAC DMA interface. Typically, an event consists of about 50 kbytes of data. The data acquisition system can handle about 5 events per second, giving a total data rate of about 250 kbytes per second. However, most of the data consists of zeroes corresponding to inactive XY channels. Because in reconstructing the trajectory, only the data from the active channels need to be stored; the primary task of the PDP 11/73 is to compress the data by removing the nonfiring channels. Then, after implementing several simple software cuts (energy, delayed events, etc.), the PDP 11/73 encodes the data to reduce the total data rate to 15 kbytes per second. Finally, it packs the data into Ethernet format for transmission to a UNIX host (Tektronix 6130). The Ethernet connection between the PDP 11/73 and the Tektronix 6130 is completely modular, and if it turns out that more computing power is needed for data analysis, the PDP 11/73 can send alternate events to two or more hosts. Similarly, the front end processing can be subdivided.

The function of the Tektronix 6130 is to collect the data from the network, unpack and decode it, and assemble it into a four-dimensional array of X, Y, Z (time), and charge for use in the trajectory reconstruction and energy signal

display algorithms.

This data transfer process uses up only about 15% of the CPU time of the Tektronix 6130, leaving the rest of the time for on-line data analysis. The analysis routines will apply various software cuts to the data. The data which survive these cuts are stored on 61TC01 60 Mbyte cartridge tapes or on hard disks.

The real time data acquisition of the TPC, which uses a DEC-RT11 to UNIX UDP-TCP/IP interface, is discussed in more detail in [75].

6.6 Software analysis

The analysis facilities on the Tektronix 6130 include track reconstruction in the (x,z) and (y,z) projections, statistical histogramming of individual channels, plotting of energy spectra, graphic output to a laser printer, on-line display and various other diagnostic facilities. The preliminary analysis algorithms concentrate on handling the data from the xz and yz projections separately. For each projection, programs have been written to select the electron track from a point source, to calculate lengths of tracks and to identify discontinuous or multiple tracks in one event. A program has also been written that locates charge blobs and determines whether they are at the end of a trajectory.

One of the tasks still under way is to fold the information from the (x,z) and (y,z) projections into a three-dimensional track and also to identify the background events. With track reconstruction alone, muons and alpha particles can be rejected with 100% efficiency. As discussed in Chapter 5, the main background events are single electron production from Compton scatterings and electron-positron pair production. The Monte Carlo simulations that were performed indicated that it should be possible to reject 95% of single electron tracks by summing up and comparing the charge depositions at both ends of the tracks. By looking at the second derivatives of the trajectories at the ends,

an even higher rejection efficiency can be achieved. This can be done because single electron tracks have relatively straight beginnings, whereas at both ends of a double beta decay event, large angle multiple scatterings occur. A more detailed discussion of the software analysis is presented in [59].

CHAPTER SEVEN

Performance of the Xe TPC and Preliminary Results

7.1 Introduction

The TPC was shipped to Switzerland during July 1988 and is now operating at the University of Neuchatel. During its stay at Caltech, the electronics for the complete readout system was made and installed, and the data acquisition system was fully developed. To have more flexibility during the preliminary diagnostic studies, readily available materials were used for some components. Prior to shipment most of these temporary components were replaced by their low background counterparts. Extensive studies were made of the track reconstruction abilities and energy resolution of the TPC. Various gas purification schemes were investigated, and a xenon gas recovery system was developed.

The performance of the TPC at Caltech will be discussed in this chapter.

7.2 Energy Resolution

Three anode systems were used to study the energy resolution of the TPC. The first system (Mark 1) had an anode wire spacing of 7 mm. Stainless steel wire with a diameter of 20 μm was used for the anode wire, and 75 μm diameter copper wire was used for the field wires. The wires were tensioned by hand and soldered onto copper rings, which were etched on a circuit board with an inner diameter, outer diameter, and thickness of 612 mm, 711 mm, and 1.6 mm, respectively. Figure (7.1) depicts a schematic of the system. The ring used to anchor the anode wires was on the upper side of the circuit board, whereas

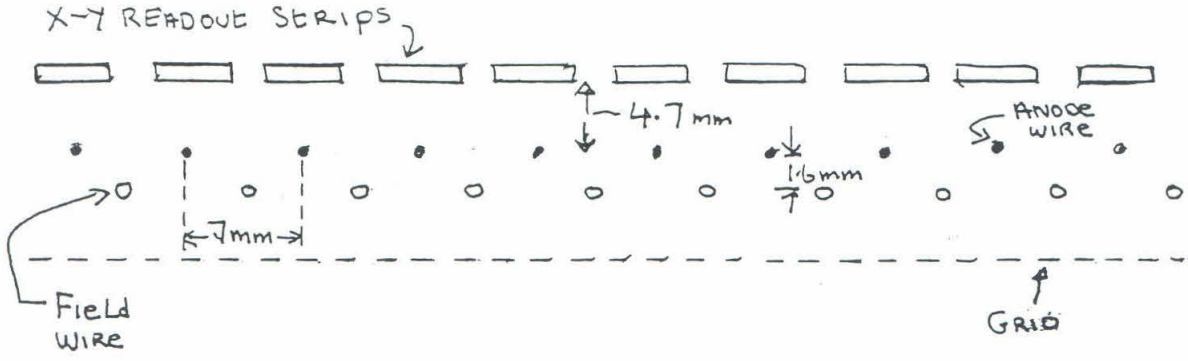

Figure (7.1) Schematic representation of the Mark 1 anode system.

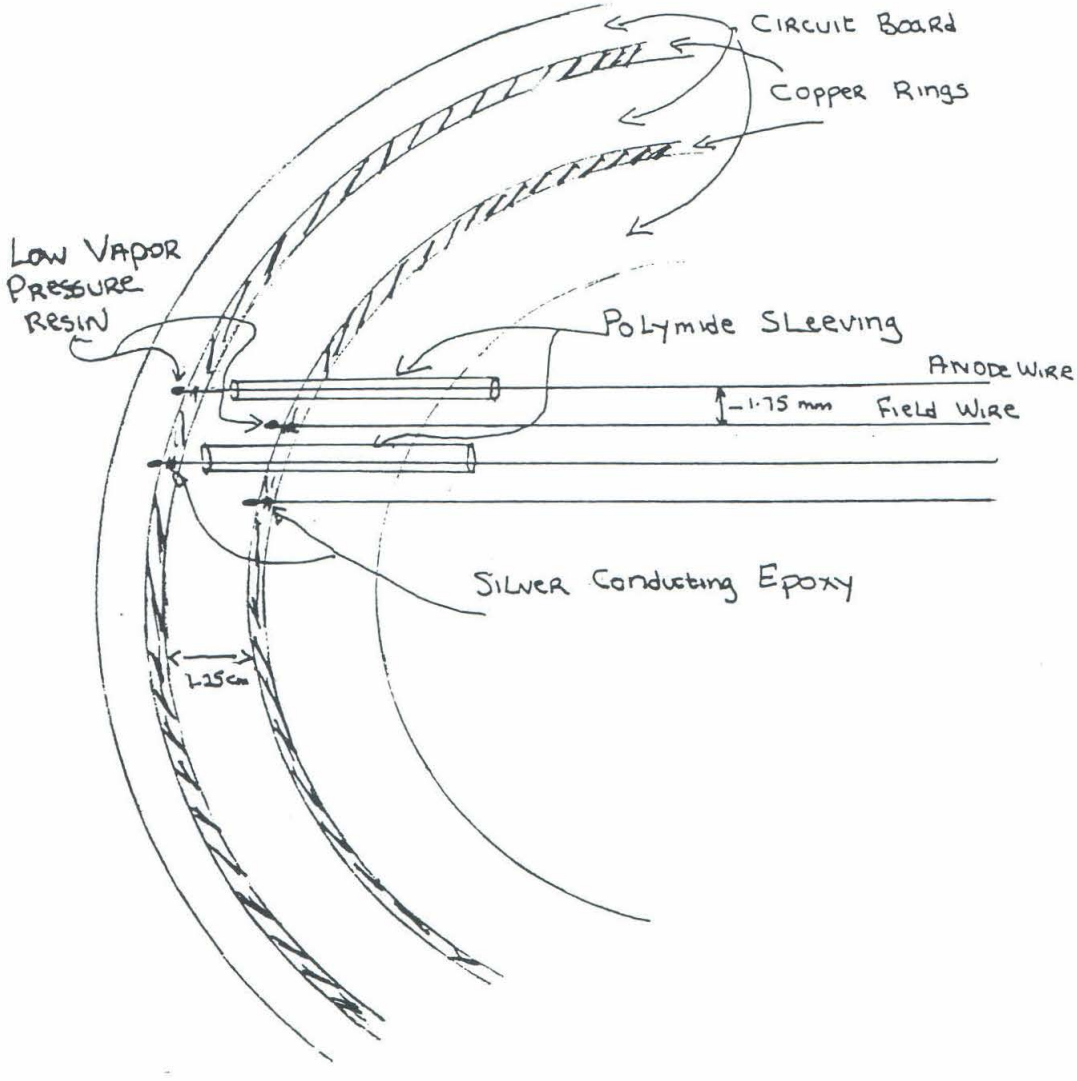

Figure (7.2) Schematic representation of the Mark 2 anode system.

the ring for anchoring the field wires was on the other side. To stabilize the anode wires against electrostatic deflection, seven nylon wires 225 μm in diameter were wound orthogonal to the wires. The anode-field wire frame was separated from the xy pad by 4.2 mm. Geometrical uncertainties in the system were about 635 μm.

The second anode system (Mark 2) had an anode wire spacing of 3.5 mm. Anode wires were stainless steel wires 20 μm diameter, and the field wires were stainless steel wires 38 μm diameter. Figure (7.2) depicts a schematic of the system. The tension applied to the anode wire was 50 g, and a tension of 100 g was applied to the field wires. The grid, which was made from 50 μm stainless steel wires, was mounted on the underside of the anode-field wire frame. The grid wires were tensioned to 150 g, to balance the force put on the other side of the frame by the anode field wire combination. The wires were anchored to the circuit board using a low vapor pressure resin epoxy (Varian Torr seal). To make the electrical contact to the copper ring on the circuit board ECCOB, solid 56-C silver conducting epoxy was applied to the wire and underlying section of the ring. Geometrical uncertainties were about 254 μm.

The third anode system (Mark 3) was identical to Mark 2 except that the xy pad was replaced by a double-sided copper clad, 1.6 mm thick circuit board. This circuit board had a trigger pad (50 mm diameter) at the center and a veto ring 584 mm in diameter. The board was flat to within 25 μm, and the variation in the separation of the anode wire-circuit board was 152 μm.

Two sources were used to study energy resolution: ^{113}Sn and ^{207}Bi. During a measurement the source was placed on the center of the TPC cathode. Figure (7.3a) shows the internal conversion spectrum of ^{113}Sn. The two peaks correspond to K electrons (363 keV) and L electrons (387 keV). Figure (7.3b) shows the ^{207}Bi internal conversion electron spectrum obtained with a Si-Li detector. The energy measurements were done using p-10 at 5 atm and Xe-CH_4 at 2 atm. The energy resolution obtained in both cases was comparable.

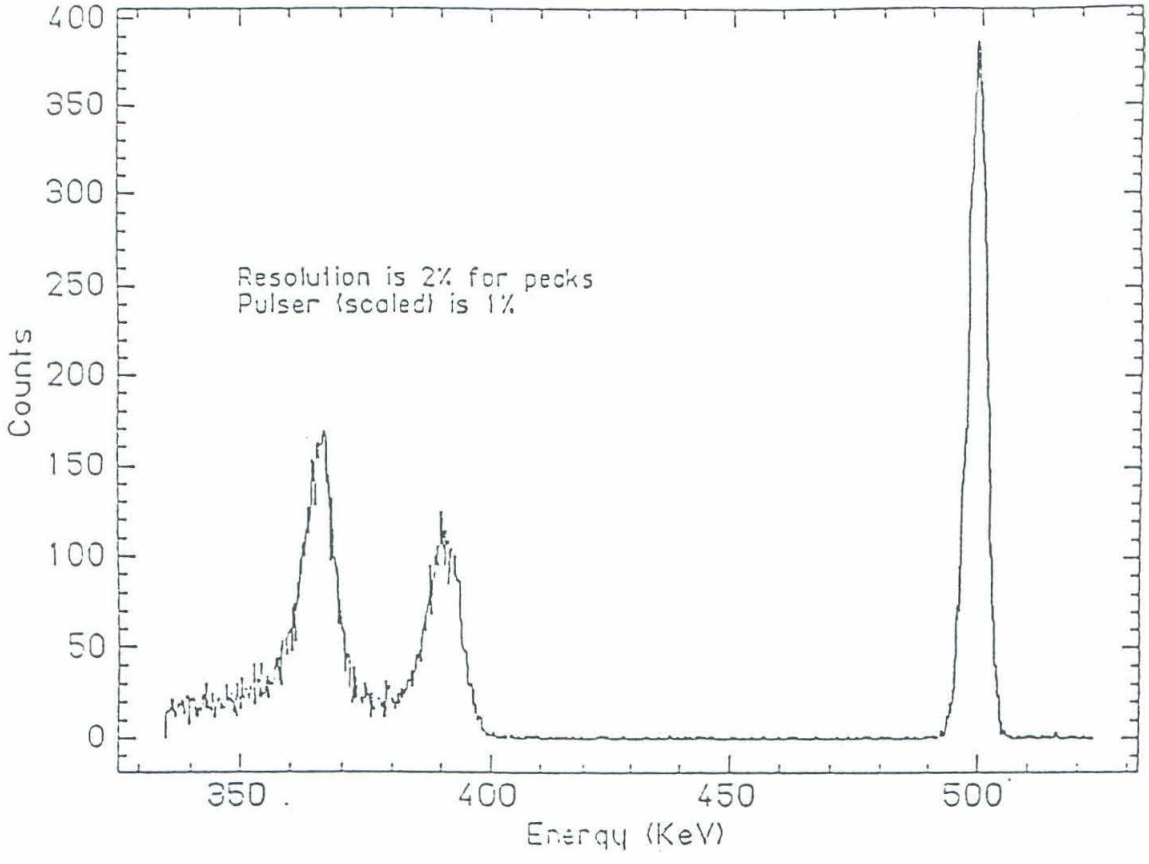

Figure (7.3a) Spectrum of ^{113}Sn source in a Si-Li detector.

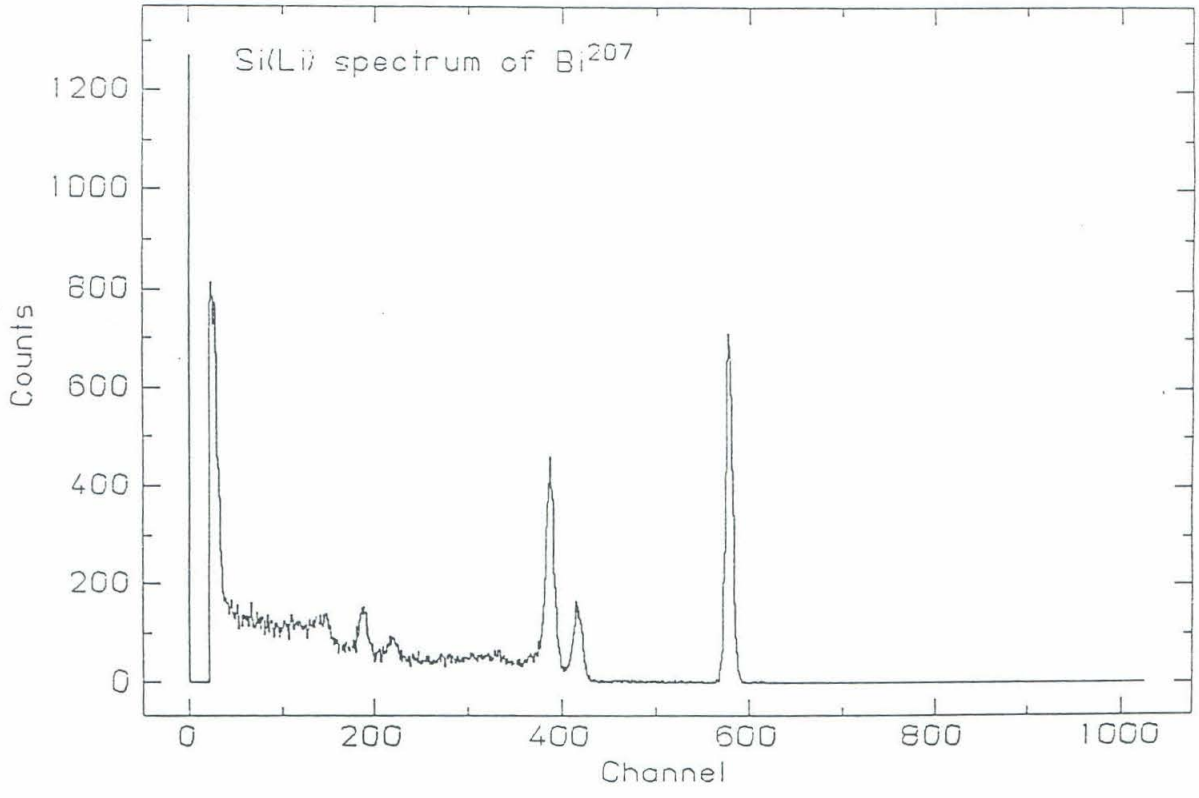

Figure (7.3b) Internal conversion electron spectrum of ^{207}Bi as obtained with a Si-Li detector.

The ^{113}Sn spectrum was measured only with Mark 1 in 2.5 atm of p-10. Figure (7.4) shows the measured spectrum. From Figure (7.3a), it can be seen that there are two peaks (363 keV and 387 keV). In the TPC the peaks are difficult to resolve since the detection efficiency of the 28 keV X-rays first had to be estimated. The measured width of the 400 keV peak was 128 keV. With this anode sytem the variation in charge gain throughout the anode-pad system was investigated. A cathode that had eight alpha sources (^{212}Bi) screwed into one quadrant was rotated, and the pulse height was measured as a function of the anode wire location. A 3-D gain plot was then made, as shown in Figure (7.5). Measurements showed that there was a variation in the anode wire-xy pad separation of 1.5 mm. The separation mapping matched the gain plot quite closely; regions of high gain occurred where the separation was smallest. Spacers were inserted between the xy pad and the anode wire frame, and the separation and charge gain variations were remeasured. The anode wire-xy pad separation was more uniform, but some gain variation still existed. A program was developed that compensated for the gain variations. The measured peak width now gave a resolution of 25 % at 400 keV.

Using Mark 1, the measured width for the 1 MeV peak (the fused peaks at 975 keV and 1048 keV) of ^{207}Bi was between 160 and 200 keV, giving a resolution of between 16 and 20 %. The spectra obtained are shown in Figure (7.6). Using Mark 3 the measured width for the above 1 MeV peak gave a resolution of (14 ± 1)%. If it is assumed that the TPC was detecting the two electron lines in an intensity ratio of 3:1, then the resolution at 1 MeV was (11 ± 1)%. If the energy resolution scales with energy as $\sqrt{E^{-1}}$ (Chapter 5), then the above result implies a resolution of (7.0 ± 0.7)% at 2.5 MeV. In taking the energy spectra, there was a hardware requirement that the anode signals be long (8 μs out of a drift time of 12 μs for p-10 and 8 μs out of a drift time of 40 μs for xenon). This hardware cut rejected low energy events that resulted from backscattering of electrons on the cathode and from the 500 keV peak.

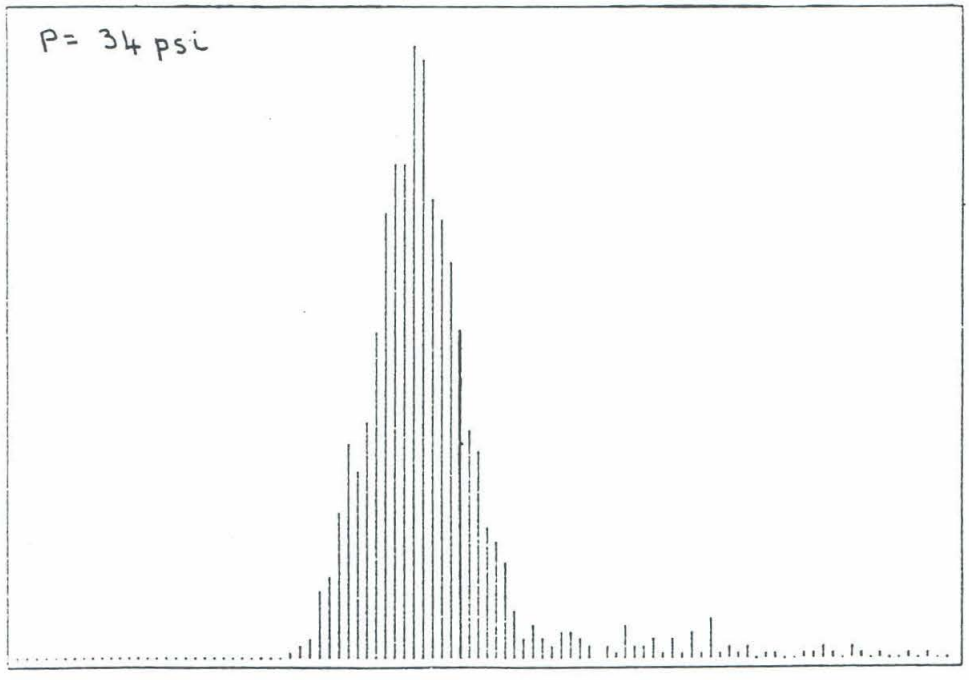

Figure (7.4) ^{113}Sn spectrum as measured using Mark 1, with p-10 as the fill gas.

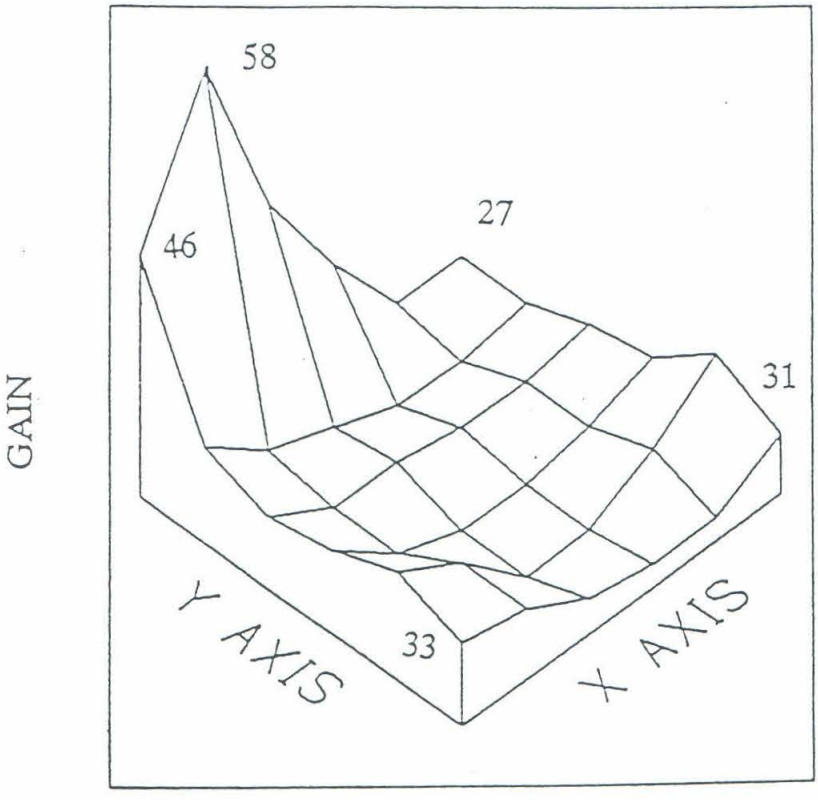

Figure (7.5) The gain variation in the X-Y readout plane.

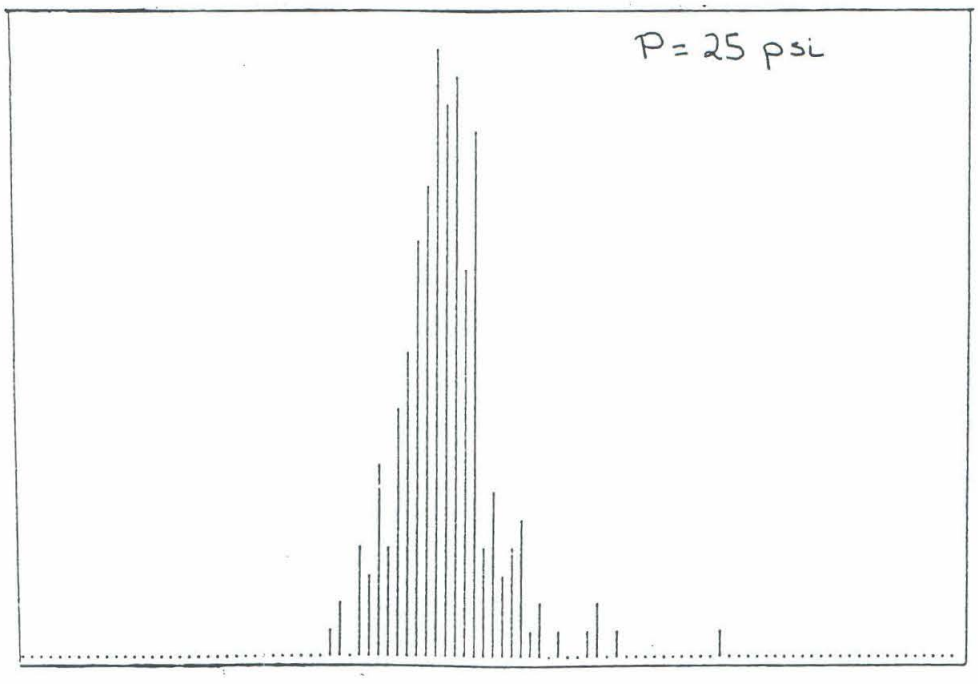

Figure (7.6a) The 1 MeV peak of ^{207}Bi as measured using Mark 1, with xenon as the fill gas.

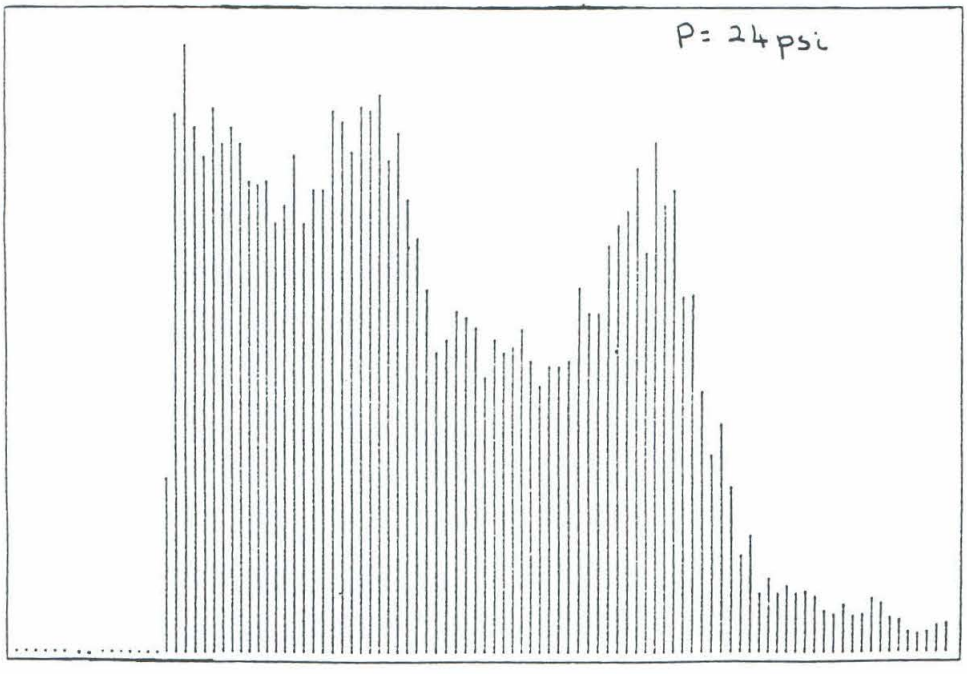

Figure (7.6b) The ^{207}Bi spectrum as measured using Mark 3, with xenon as the fill gas.

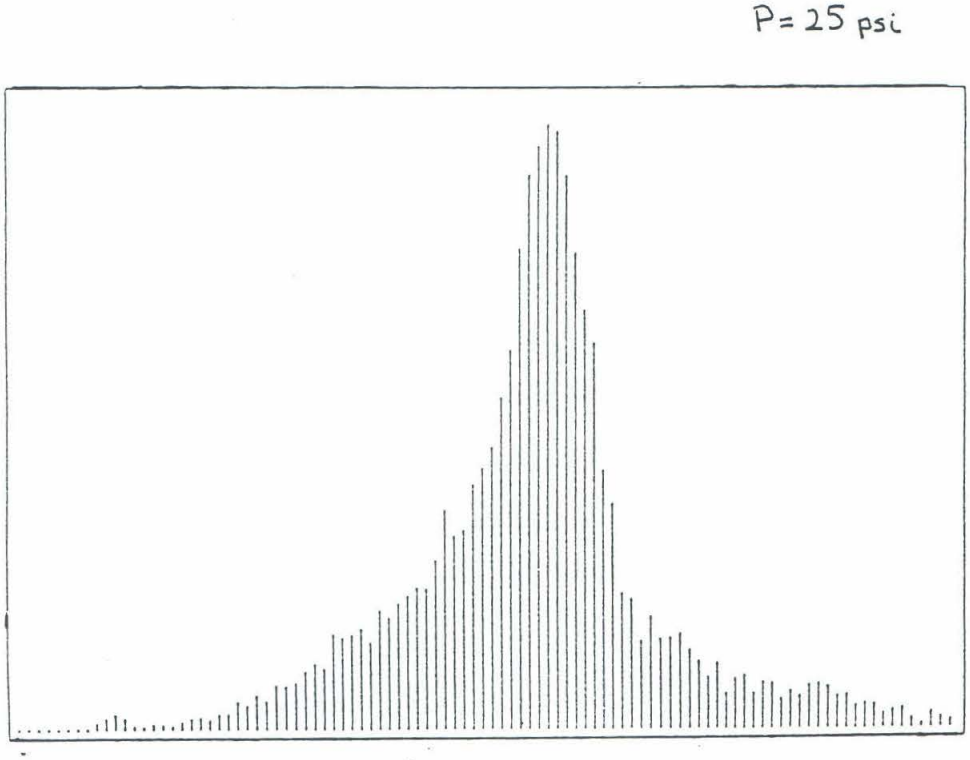

Figure (7.6c) The 1 MeV peak of ^{207}Bi as measured using Mark 3 and xenon gas.

In xenon it was observed that the slower drift speed made the spectra more susceptible to contamination, micro-discharges and random electronic noise. On the time scale of 5 hours, there was an observable shift of the entire spectrum to the low energy side. Also, the anode signals became discontinuous, and thus the hardware length cut decreased in efficiency.

Using Mark 1 the optimal range of working voltage that would give a high (compared to background counts) count rate from the electron source and which would give a reasonable energy spectrum was as low as 30 V. With Mark 2, the spectral shape remained constant over a range of 100 V.

During construction of the anode system, much useful information was acquired. It was observed that once properly tensioned, the anode wires could be stretched (unsupported) over a length of 60 cm, and a voltage of at least 3 kV could be applied to the wires before they oscillated. Various suitable materials for the anode wires were tested. Based on these tests, gold plated tungsten was chosen as the anode wire material for the final low background anode wire system. Gold-plated tungsten has a high tensile strength and can easily be soldered using low temperature solders. At present the search is on for a low background material that can be used for the anode wire support frame. At the moment, the Shell Epon resin used to attach the delrin honeycomb to the Rexolite board (Chapter 5) appears to be a likely candidate for this job.

7.3 Track Reconstruction

In the earlier stages of the experiment, p-10 (90% Ar-10% CH_4) was used for the TPC fill gas. The proportional properties of p-10 were well known. Thus, it was useful to fill the TPC with p-10 to assist in debugging electronic and hardware problems. Initially, adjacent x and adjacent y channels were connected, giving a spatial resolution of 7 mm. In this setup, the xy readout pad

was made from G-10; later, it was replaced by the Rexolite board, which gave the full spatial resolution of 3.5 mm. Also, an aluminum cover was used for the TPC in order to facilitate removal of the cover. The final copper cover weighed about 1/4 ton, making it difficult to remove.

For the first year of operation, the Mark 1 system was used. Figure (7.7) shows some tracks produced in the TPC. The tracks produced by alpha particles, muon particles, cosmic ray showers, and electrons all show very distinctive features. The charge blobs at the end of the electron tracks were visible, and it was possible to locate the beginning and ends of the track.

Figure (7.8) shows some tracks obtained with the full resolution system, both with Mark 1 and Mark 2. It can be seen that the tracks are narrower.

One very interesting measurement is shown in Figure (7.9) Here a statistics spectrum is shown in which all the channels were monitored for hits. This diagnostic facility was developed in order to check for dead electronic channels. In the YZ projection, there are seven discontinuities, which correspond to the seven nylon wires used to support the anode wires. Thus, it can be seen that the nylon wires give rise to a region that is insensitive to multiplication. The width of this region is approximately 1.4 cm.

7.4 dE/dx measurement

From the electron track in Figure (7.8c), it can be seen that the electron tracks show the features predicted by the Monte Carlo. The tracks had relatively straight beginnings and staggered ends. The presence of the increased charge deposition at the end of the trajectory was also clearly visible. From these findings, it was concluded that the 2-bit digitization scheme was adequate for distinguishing between the minimum ionizing region of the track and the blobs produced at the ends of the track and those places where delta electrons were generated. Delta electrons showed up prominently, especially in muon

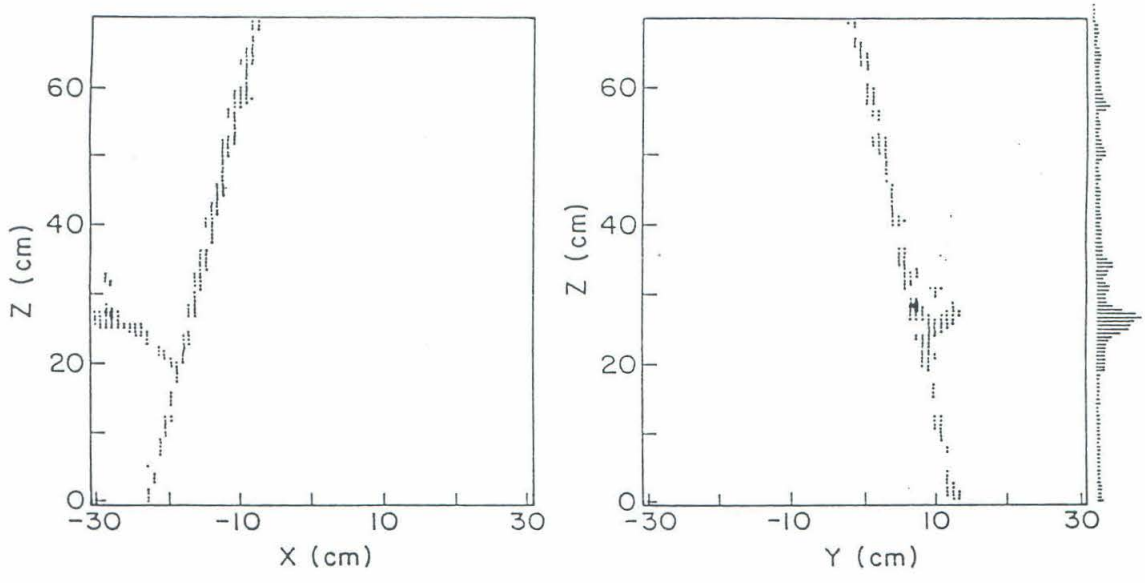

Figure (7.7a) The xz and yz projection of a cosmic ray muon ejecting a delta electron. The energy signal of the muon is shown as a function of the drift time on the right-hand side. The fill gas was p-10.

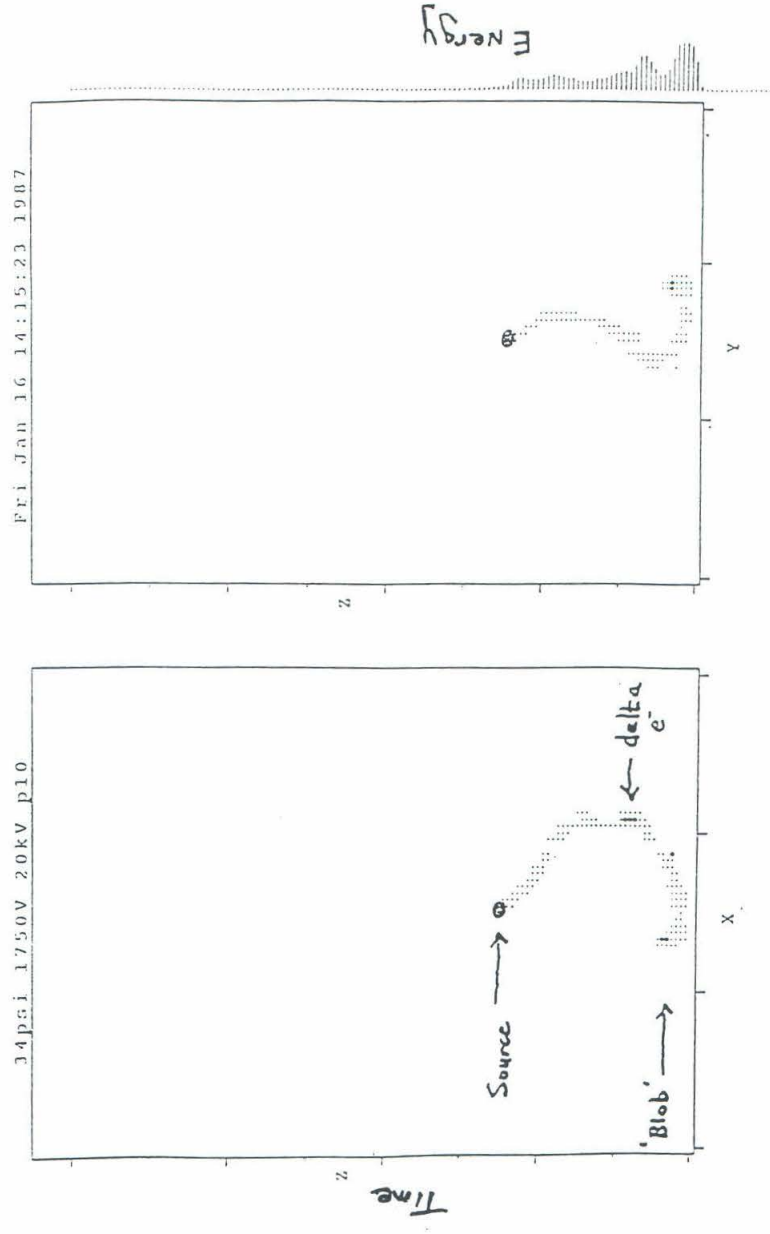

Figure (7.7b) The xz and yz projection of an electron emitting a delta electron. The fill gas was p-10.

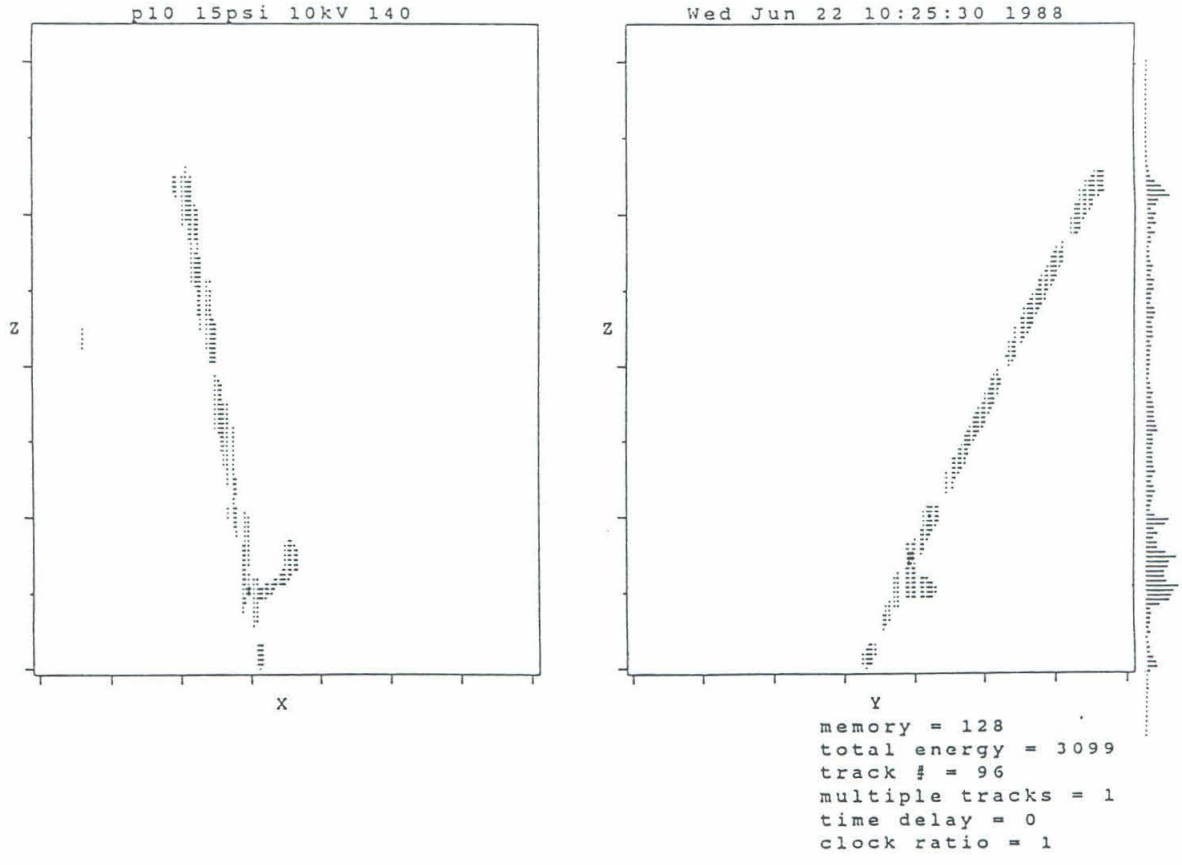

Figure (7.8a) Projections of a muon ejecting a deta electron.

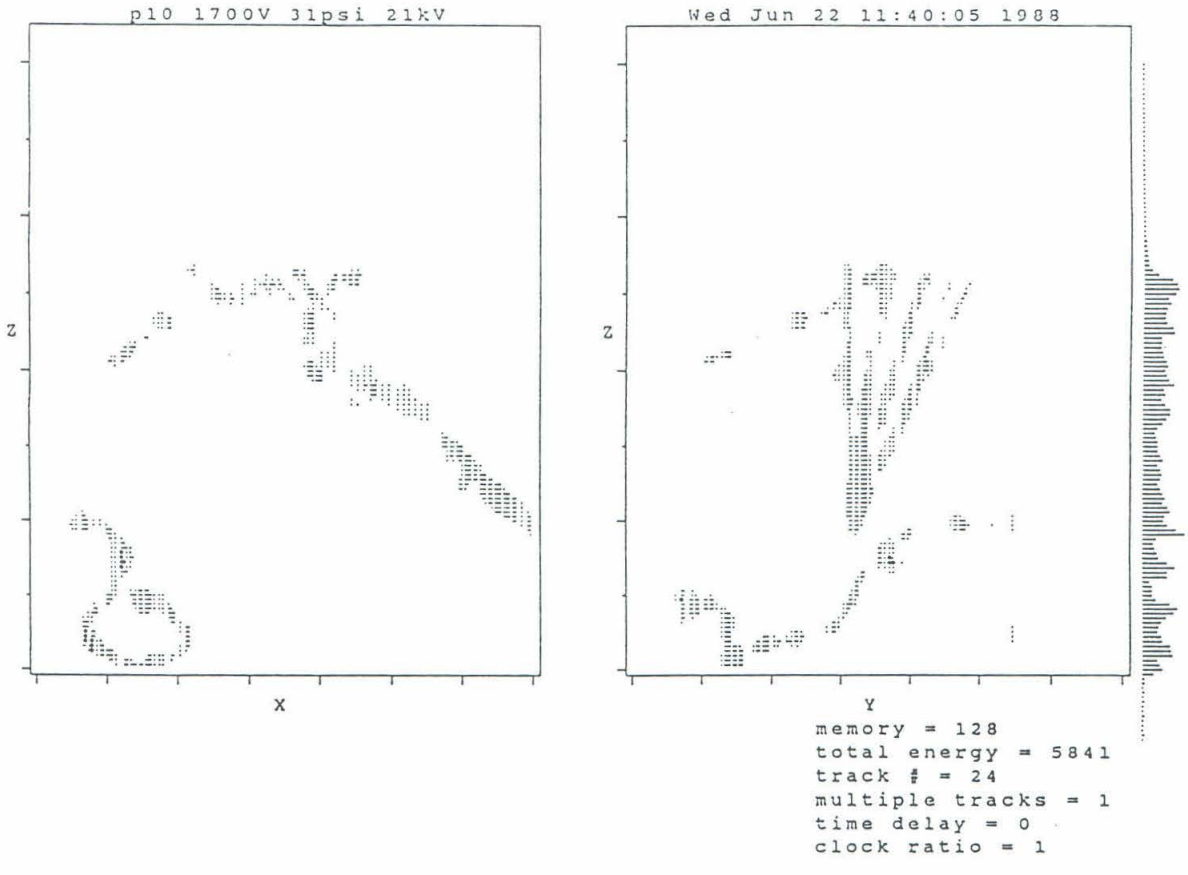

Figure (7.8b) Projections of a cosmic ray muon shower and an electron track.

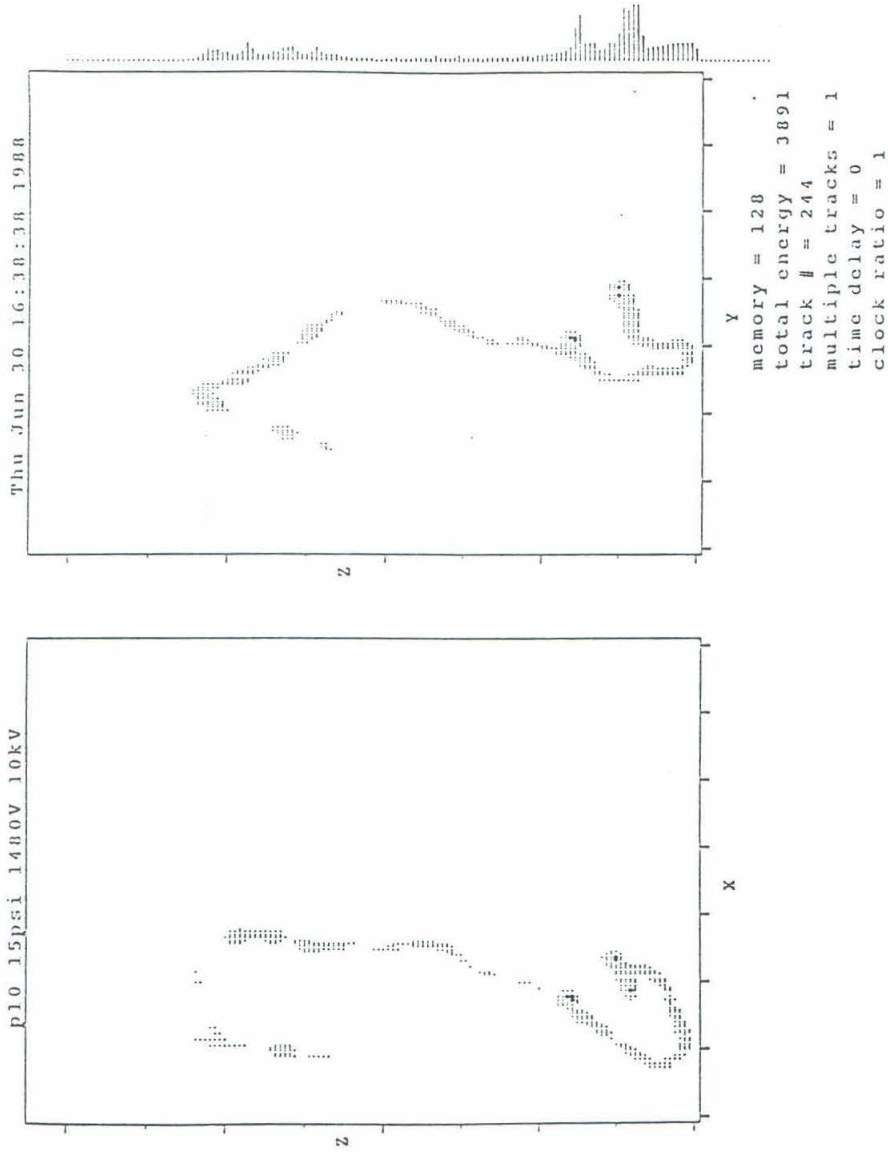

Figure (7.8c) Projections of an electron track ejecting a delta electron.

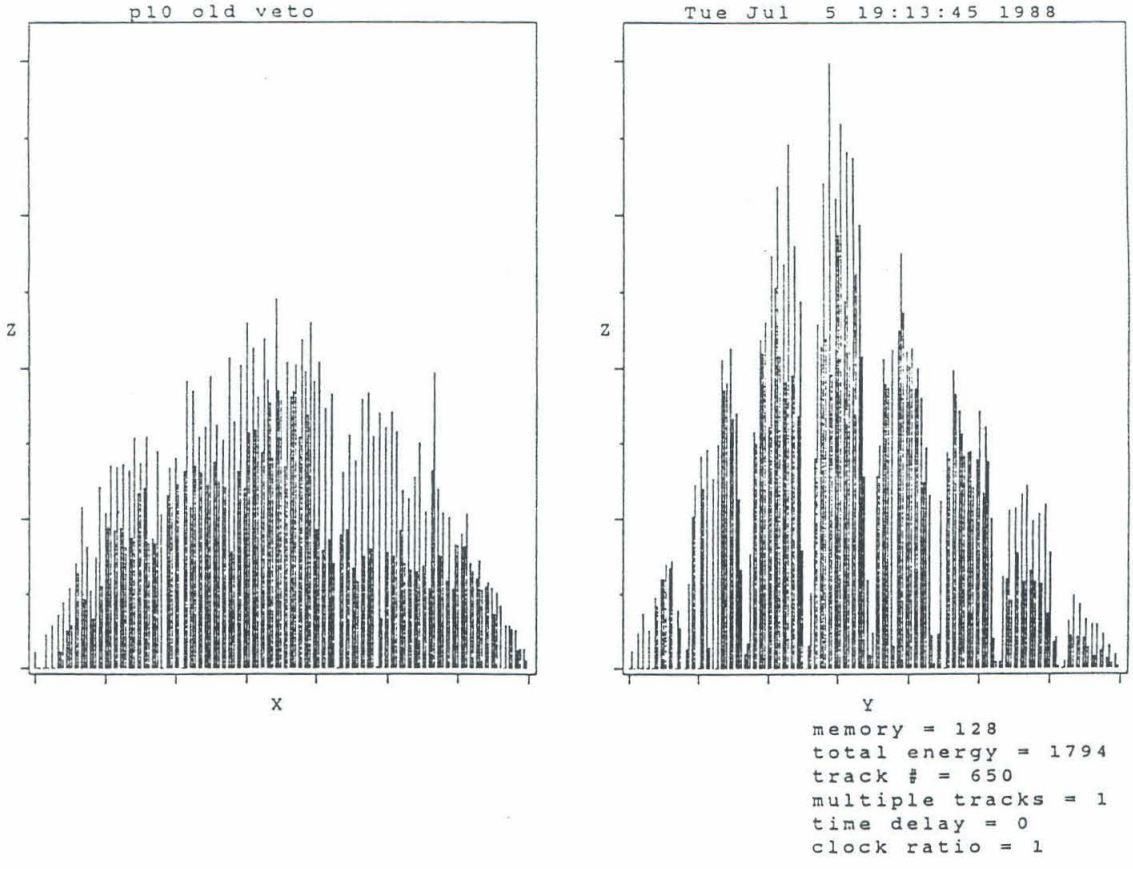

Figure (7.9) Statistics histogram of firing channels.

tracks.

7.5 Gas Purification

It was possible to drift electrons the full length of the TPC when it was filled with Xe - 5%CH_4 at 5 atm. However, the degradation of the track quality proceeded rapidly. During testing of the TPC at Caltech, six purification schemes were investigated, as follows:

(*1*) *Gas circulation through MnO and molecular sieve.* A schematic of the system is shown in Figure (7.10). The gas was circulated using a metal bellows pump (Model MB-302, Metal Bellows Corp.). The total volume of gas in the TPC could be circulated through the purifier once every fifteen minutes. The purifier consisted of a stainless steel column (1.5 m in height and 15 cm in diameter), which contained MnO and molecular sieve (4A). The total volume of gas could be circulated through the purifier once every fifteen minutes. The MnO removed O_2 from the circulating gas, while the molecular sieve trapped water molecules. When the system became overloaded, it could be regenerated by heating the MnO and sieve and by flushing it with H_2 gas. The setup was a very efficient purification scheme. However, it was not compatible with the low background requirements of the experiment. Commercial molecular sieve contains a significant amount of ^{238}U and ^{232}Th. These two isotopes both outgas radioactive ^{222}Rn and ^{220}Rn and thus would generate background problems in the TPC.

(*2*) *Gas circulation through a commercial hydrox.* The pump as described above was used to circulate the gas through a Hydrox purifier (Matheson Model 8301). Although this system performed well, the pump had a maximum operating pressure of 2.5 atm and caused the system to vibrate.

(*3*) *Gas circulation by a magnetically coupled pump through a hydrox.* In order

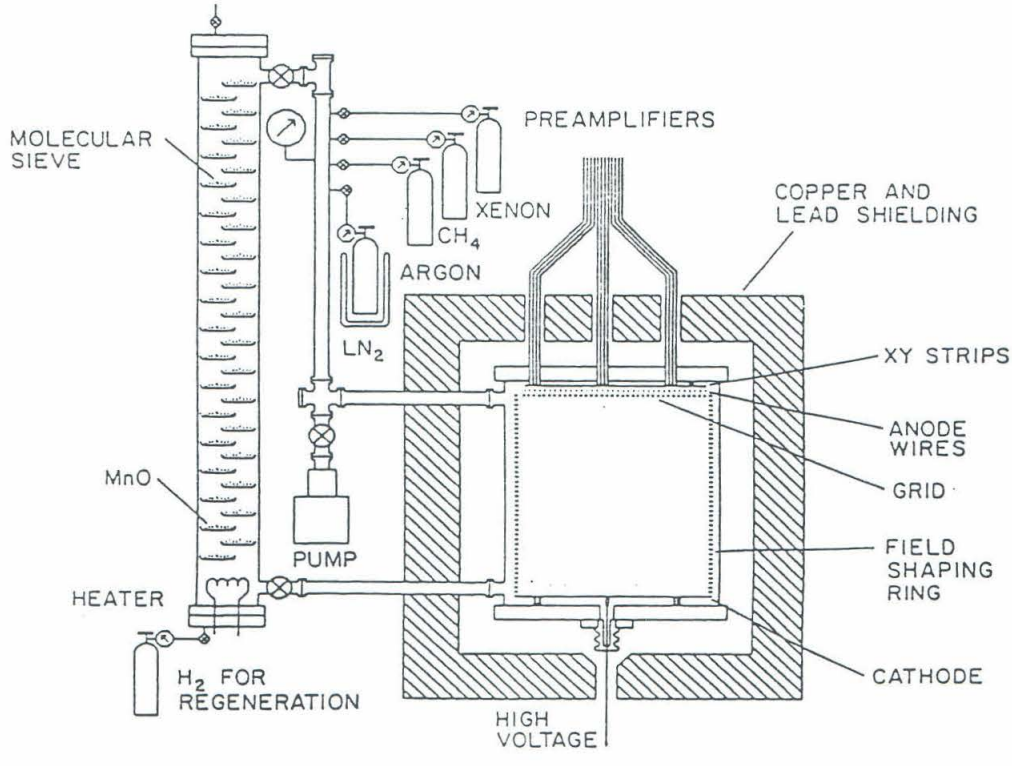

Figure (7.10) Schematic of purification scheme (1).

to overcome the problem discussed in the system above, a magnetically coupled pump (Brey GK 07-M) was introduced into the system. Most pumps are sealed, using some type of shaft seal. These shaft seals are dynamic seals and allow leakage and contamination to occur. Magnetically coupled pumps utilize a static seal, which greatly reduces maintenance and virtually eliminates the possibility of contamination or leakage. After a few months of operation, it was found that the graphite rotating vanes had worn away, and the resulting graphite dust had found its way into the TPC chamber. Various materials to replace the graphite were tested, but none proved satisfactory.

(*4*) *Gas circulation by convection through turnings made from an alloy of zirconium, titanium, and nickel.* A schematic of the system is shown in Figure (7.11). The system was tested using 30 psi of Xe - 5%CH_4 and with the ^{207}Bi source on the cathode. After regenerating the turnings, the heating tape was turned on and the gas was circulated. Then the turnings were heated. Initially the gas was dirty and the 1 MeV peak was absent in the energy spectrum. After about an hour the 1 MeV peak began appearing in the spectrum, and after twenty four hours the peak had reached the maximum position (same as for clean gas). With this purification scheme the gas was kept clean for three days, after which the heating tape was shut off. The 1 MeV peak shifted to the low energy side of the energy spectrum, but upon turning on the purifier, the clean spectrum was recovered.

However, some of the turnings were carried by the gas into the main chamber where they caused problems such as high voltage breakdown of the cathode to the bottom cover of the TPC. Thus, a new gettering compound was investigated.

5) *Gas circulation by convection through titanium vanes.* The same basic scheme as described in scheme (4) was used except that the Zr-Ti-V turnings

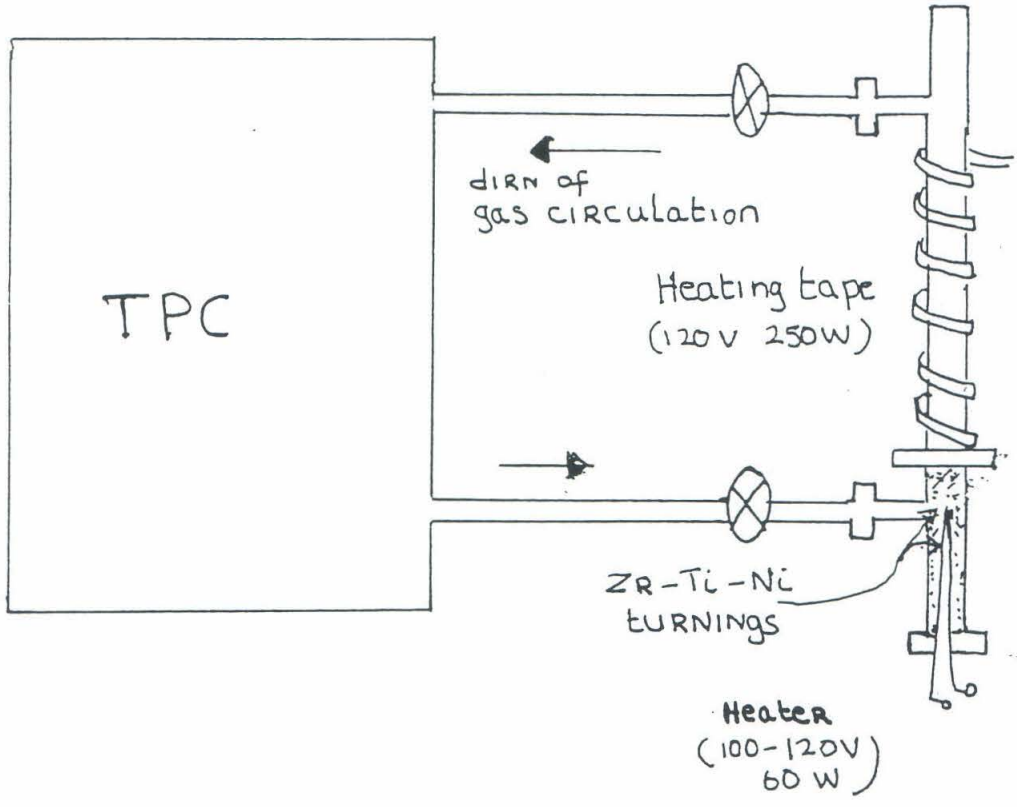

Figure (7.11) Schematic of purification scheme using convection through Zr-Ti-Ni turnings.

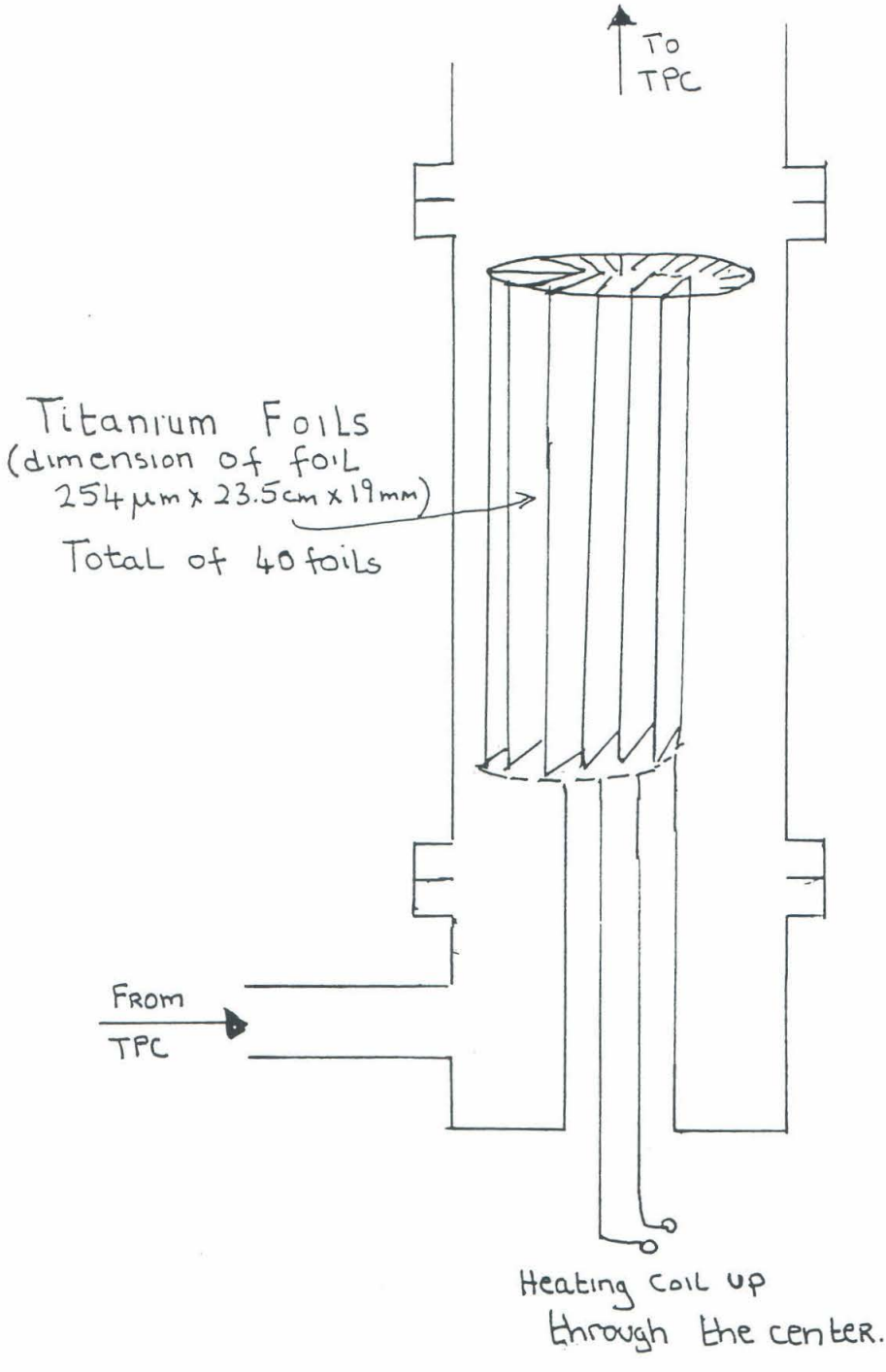

Figure (7.12) Schematic of the Ti vanes. This section replaced the section containing the Zr-Ti-Ni turnings in Figure (7.11).

were replaced by titanium vanes, as indicated in Figure (7.12). After initial testing, it was found that this system increased the pulse height but could not solve the problem of track deterioration (i.e., could not get long muon tracks). Further research determined that titanium needs to be at 800 °C before it can purify, and it removes only oxygen, leaving the water vapor in the system.

6) Gas circulation by convection through SAES St707 getter material. Upon contacting SAES getter company, it was found that the company manufactured a getter material (St707) which, when operated at temperatures below 250 °C, will purify xenon without removing CH_4. During preliminary tests in the summer of 1988 at Caltech, it was determined that this getter material was a very efficient purifier. After the getter is activated, gaseous impurities such as H_2, O_2, H_2O, CO, CO_2, and N_2, which strike the getter's surface, are captured and chemisorbed. Only noble gas atoms are not affected by this process. The purification properties of the getter were tested at temperatures ranging from room temperature to about 400 °C. O_2 and H_2O were readily absorbed, but at the temperature range investigated, no methane was removed. The getter was purchased in the form of a St707 powder layer deposited and fixed on both sides of a thin, continuous constantan (55% Cu - 45% Ni) strip. At Neuchatel, the getter strip was installed in the titanium vane holders as described in (5) above. The gas was circulated by convection through the getter. It was found that this system was able to maintain the gas purity for 9 days, when the TPC contained xenon gas at 1.5 atm.

7.6 Drift velocity measurements

The drift velocity was measured using the drift time of vertical muons as they passed through the TPC. A scintillator panel (Chapter 5, Sec 5.14) and plastic scintillator paddles, which rested on top and underneath the TPC provided the muon trigger. The drift velocity as a function of drift field was

measured for Xe - 5%CH_4 at 1 atm and for p-10 at 1 atm. The drift velocity is dependent on the ratio of Xe and CH_4 [48]. Thus, by measuring the drift velocity, the amount of CH_4 present in the xenon can be monitored.

7.7 Track Reconstruction and Background Rejection

In the ideal case of no diffusion and no smearing of trajectories during charge multiplication, Monte Carlo studies indicated that at 5 atm of xenon, single electron tracks at 2.5 MeV could be rejected with a 95% efficiency by summing the total charge along a track and analyzing the charge accumulation in a given region surrounding both ends of the trajectories. If the second derivatives are measured at the ends of the track, then this efficiency can be further increased. The work performed to date used the two 2D projections of the track (xz and yz, the xy projection is not measured directly). The goal is to fold the two 2D projections into one 3D track. To do this may require intensive computer power. Several difficulties exist: Tracks can be broken and noise may be present. Sharp bends, smearing of the tracks and energetic delta electrons all cause confusion. The tracks have no preferred origin, direction, or orientation. Another problem is that of combinatorial ambiguities; given a plane at which the track crosses more than once, it will be impossible to select which of the possible combinations of x,y correspond to the real track. A detailed discussion of the track reconstruction algorithms is presented in [59].

7.8 Future Plans and Time Scale

Currently, the TPC is at the University of Neuchatel. The gas purification system and gas recovery system are being fine tuned. The low background anode system (which will have a controlled geometry) is under development; the lead shielding that will surround the TPC in the tunnel is under

construction, and the data analysis programs are being upgraded. The TPC is due to be installed in the tunnel by February 1989, at which time preliminary background studies will commence. In April 1989, the final anode system is to be installed and by June 1989, data taking should start with the TPC filled with xenon depleted in ^{136}Xe and then with xenon enriched in ^{136}Xe (60%).

REFERENCES

[1] W. Pauli, *Letter to the Physical Society of Tubingen, unpublished; reproduced in* L.M. Brown, *Physics Today*, **31**, No. 9, 23 (1978)

[2] C.L. Cowan et al., *Science*, **124**, 103 (1956).

[3] G. Danby et al., *Phys. Rev. Lett.*, **9**, 36 (1962).

[4] M.L. Perl et al., *Phys. Rev. Lett.*, **35**, 1489 (1975).

[5] Z. Maki et al., *Prog. Theor. Phys.*, **28**, 870 (1962).

[6] B. Pontecorvo, *Zh. Eksp. Theor. Fiz.*, **53**, 1717 (1967).

[7] T.D. Lee and C.N. Yang, *Phys. Rev.*, **104**, 254 (1956).

[8] S.L. Glashow, *Nucl. Phys.*, **22**, 579 (1961).

[9] A. Salam and J.C. Ward, *Phys. Rev. Lett.*, **13**, 168 (1964).

[10] S. Weinberg, *Phys. Rev. Lett.*, **19**, 1264 (1967).

[11] B. Kayser, *Comments on Nuclear and Particle Physics*, **14**, 69 (1985).

[12] R. Davis, *Phys. Rev.*, **97**, 766, (1955); *Bull. Am. Phys. Soc., Series 2*, **1**, 219 (1956).

[13] V. Lubimov et al., *Phys. Lett.*, **B94**, 266 (1980).

[14] V. Lubimov, **Massive Neutrinos in Astrophysics and Particle Physics, Proceedings of the 7^{th} Moriond Workshop**, eds. O. Fackler and J. Tran Thanh Van, Editions Frontieres: Paris (1987).

[15] F. Boehm and P. Vogel, **Physics of Massive Neutrinos**, Cambridge University Press, Cambridge (1987).

[16] E. Segre, **Nuclei and Particles**, W. A. Benjamin, Inc., New York (1964).

[17] R. Davis et al., in **Science Underground, AIP Conf. Proc., 96**, eds. M.M. Nieto, Am. Institute of Physics: New York (1983).

[18] W.C. Haxton and G.J. Stephenson, *Prog. in Part. and Nucl. Phys.*, **12**, 409 (1984).

[19] M. Doi et al., *Prog. of Theor. Phys. Suppl.*, **83** (1985).

[20] H. Primakoff and S.P. Rosen, *Rep. Prog. Phys.*, **22**, 121 (1959).

[21] J. Engel et al., *Phys. Rev C*, **37**, 731 (1988).

[22] H.V. Klapdor and K. Grotz, *Nucl. Phys.*, **A460**, 395 (1986).

[23] H. M. Georgi et al., *Nucl. Phys.*, **B193**, 297 (1981).

[24] W.C. Haxton et al., *Phys. Rev.*, **D26**, 1805 (1982).

[25] T. Kirsten et al., *Phys. Rev. Lett.*, **50**, 474 (1983); and *Z. Physik*, **C16**, 189 (1983).

[26] S.R. Elliott et al., *Phys. Rev. Lett.*, **59**, 2020 (1987).

[27] C.A. Levine et al., *Phys. Rev.*, **77**. 296 (1950).

[28] W.C. Haxton et al., *Phys. Rev.*, **C28**, 467 (1983).

[29] L.W. Mitchell and N. Winograd, *Bull. Am. Phys. Soc.*, **31**, 1219 (1986).

[30] P.Fisher, in **Massive Neutrinos in Astrophysics and Particle Physics, Proceedings of the 6^{th} Moriond Workshop**, eds. O. Fackler and J. Tran Thanh Van, Editions Frontieres: Paris (1986).

[31] D.O. Caldwell in **Neutrino '86, Proc. 12^{th} Int. Conf. Neutrino Physics and Astrophysics,,** Sendai, eds. T. Kitagaki and H. Yuta, World Scientific: Singapore (1986).

[32] F.T. Avignone et al., *Phys. Rev.*, **C34**, 666 (1986).

[33] E. Bellotti et al., In **Massive Neutrinos in Astrophysics and Particle Physics, Proceedings of the 6^{th} Moriond Workshop**, eds. O. Fackler and J. Tran Thanh Van, Editions Frontieres: Paris (1986).

[34] Ejiri et al., in **Nuclear Beta Decays and Neutrino, Proc. Int. Symposium on Neutrino Mass**, Osaka, eds. T. Kotani, H. Ejiri and E. Takasugi, World Scientific: Singapore (1986).

[35] J.J. Simpson et al., *Phys. Rev. Lett.*, **53**, 141 (1984).

[36] A.S. Barabash, *NIM*, **B17**, 450 (1986).

[37] D.A. Imel and J. Thomas, to be published in *NIM*, Feb, 1989, Caltech preprint Calt 63-533.

[38] D. Yu Bardin et al., *Sov. Phys. JETP Lett.*, **13**, 273 (1971).

[39] O. Cremonesi, **Proceedings of the EPS High Energy Physics Conference, Uppsala, Sweden, 24 June - 1 July 1987**, in press.

[40] M.Z. Iqbal et al., *NIM A259*, 459 (1987).

[41] F.T. Avignone et al., Talk presented to the American Physical Society, Salt Lake City, Jan. 14-17, 1987; Univ. of South Carolina preprint, Jan. 1987.

[42] P. Fisher, Ph. D. Thesis, Caltech, 1988.

[43] D.R. Nygren, *Proposal to Investigate the Feasibility of a Novel Concept in Particle Detection*, internal report, Lawerence Berkeley Laboratory, Berkeley, California (February 1974).

[44] L.S. Barabash et al., in **Nuclear Beta Decays and Neutrino, Proc. Int. Symposium on Neutrino Mass**, Osaka, eds. T. Kotani, H. Ejiri and E. Takasugi, World Scientific: Singapore (1986).

[45] A.J.P.L. Policarpo, *Phys. Scripta*, **23**, 539 (1981).

[46] M. Salete and S.C.P. Leite, *Portugal Phys.*, fB11, 53 (1980).

[47] M. Suzuki et al., *NIM*, **192**, 565 (1982).

[48] M. Mutterer et al., **Detectors in Heavy Ion Reaction**, Lecture Notes in Physics 178, Proc., Berlin (1982).

[49] L.G. Christophorou et al., *NIM*, **171**, 491 (1980).

[50] A. Peisert and F. Sauli, **CERN** 84-08 (1984).

[51] S. Goudsmit and J.L. Saunderson, *Phys. Rev.*, **57**, 24; **58**, 36 (1940).

[52] G. Moliere, *Z. Naturforch*,3a, 78 (1948).

[53] H.A. Bethe, *Phys. Rev.*, **89**, 1256 (1953).

[54] H.A. Bethe, **Handbuch für Physik**, Vol. 24, Julius Springer: Berlin (1933), p.273.

[55] C. Moller, *Ann. Physik*, **14**, 531 (1932).

[56] F. Rohrlich and B.C. Carlson, *Phys. Rev.*, **93**, 38 (1954).

[57] R.M. Sternheimer, *Phys. Rev.*, **145**, 247 (1966).

[58] L. Pages et al., *Atomic Data Tables*, **4**, 1 (1972).

[59] H. T-k Wong, Ph. D. Thesis, Caltech 1989 (in preparation).

[60] A.O. Hanson et al., *Phys. Rev.*, **84**, 634 (1951).

[61] R.L. Ford and W.R. Nelson, **SLAC-210 Uc-32**, June 1978.

[62] L.A. Kulchitsky and G.D. Latyshev, *Phys. Rev.*, **61**, 254 (1941).

[63] K. Siegbahn, **Alpha-, Beta-, Gamma-, Spectroscopy**, Vol. 1, North-Holland (1955).

[64] D. M. Ritson, **Techniques of High-Energy Physics**, Interscience Publ.: New York (1961).

[65] G.F. Knoll, **Radiation Detection and Measurement**, John Wiley and Sons: New York (1979).

[66] J. Byrne, *NIM*, **74**, 291 (1969).

[67] W. Diethorn, **A Methane Proportional Counter System for Natural Radiocarbon Measurements**, US. AEC Report **NYO-6628** (1956).

[68] F. Sauli, *Principles of Operation of Multiwire Proportional and Drift Chambers*, CERN 77-09 (1977).

[69] E. Storm and H. Israel, *Nuclear Data Tables*, **A7**, 566 (1970).

[70] O. Helene, *NIM*, **212**, 319 (1983).

[71] W. T. Eadie et al., **Statistical Methods in Experimental Physics**, North-Holland: Amsterdam (1971).

[72] H. B. Prosper, *NIM*, **A241**, 236 (1985)

[73] H. B. Prosper, *Phys. Rev.*, **D37**, 1153 (1988)

[74] C.K. Hargrove et al., *NIM*, **219**, 461 (1984).

[75] J. Thomas et al., *IEEE Trans. Nucl. Sci., 5th Conf. on Real-Time Computer Application in Nuclear Particle and Plasma Physics* (1987).